



HAL
open science

Stress-resultant models for optimal design of reinforced-concrete frames

Ba Hung Pham

► **To cite this version:**

Ba Hung Pham. Stress-resultant models for optimal design of reinforced-concrete frames. Engineering Sciences [physics]. École normale supérieure de Cachan - ENS Cachan, 2009. English. NNT : 2009DENS0070 . tel-00538958

HAL Id: tel-00538958

<https://theses.hal.science/tel-00538958>

Submitted on 23 Nov 2010

HAL is a multi-disciplinary open access archive for the deposit and dissemination of scientific research documents, whether they are published or not. The documents may come from teaching and research institutions in France or abroad, or from public or private research centers.

L'archive ouverte pluridisciplinaire **HAL**, est destinée au dépôt et à la diffusion de documents scientifiques de niveau recherche, publiés ou non, émanant des établissements d'enseignement et de recherche français ou étrangers, des laboratoires publics ou privés.



ENSC-2009/XXX

**DOCTORAL THESIS
L'ÉCOLE NORMALE SUPÉRIEURE DE CACHAN**

Presented by

Ba Hung PHAM

for obtaining the grade of

DOCTOR OF L'ÉCOLE NORMALE SUPÉRIEURE DE CACHAN

Domain

MECHANICS - MECHANICAL ENGINEERING - CIVIL ENGINEERING

Subject of thesis

**Stress-resultant models for optimal design of
reinforced-concrete frames**

Defended at Cachan, December 15, 2009, in front of the jury :

Quoc Son NGUYEN	Professor, École Polytechnique	President
Pierre LEGER	Professor, École Polytechnique de Montréal	Opponent
Boštjan BRANK	Professor, University of Ljubljana	Opponent
Adnan IBRAHIMBEGOVIC	Professor, ENS de Cachan	Supervisor
Luc DAVENNE	HDR, ENS de Cachan	Examiner
Delphine BRANCHERIE	MDC, UT de Compiègne	Examiner

LMT-Cachan

ENS Cachan / CNRS / UPMC / PRES UniverSud Paris
61 avenue du Président Wilson, F-94235 Cachan cedex, France

This thesis could be finished by so many helps and supports from my family, my professors and my friends...

- For all members in my family, they are always in my heart .
- For my professor, **Adnan Ibrahimbegovic**, I would like to say "thank you very much" for all everything and thank for always having believe in me.
- For **Luc Davenne** and **Delphine Brancherie**, I would like to say that you are my best teachers!
- For my friends in France, I am very happy to have them always beside to support me every time and every where ... and they are always in my mind!

Contents

Contents	i
List of Figures	iii
List of Tables	vii
Introduction	1
1 Stress resultant and multi-fiber beam model for bending failure	5
1 Introduction	6
2 Embedded rotation discontinuity for Timoshenko beam	7
3 Multi-fiber beam model with embedded strain discontinuity in fibers . . .	14
3.1 Multi-fibers beam model	14
3.2 Embedding strain discontinuity in fiber	15
3.3 Assembly of all fibers in a beam element	16
3.4 Constitutive laws of the concrete and the steel	18
4 Numerical examples	20
4.1 Reinforced concrete simple beam	21
4.2 Two-storey frame ultimate load computation	23
5 Conclusions	27
2 Stress resultant and multi-fiber beam model for combined axial force and moment	29
1 Introduction	31
2 Prediction for the relations of ultimate and yield moments with axial force	32
2.1 Material properties and basic assumptions	33
2.2 Formulas for doubly reinforced-concrete rectangular section . . .	34
2.3 Prediction for ultimate moment and axial force relation	36
3 Parameter identifications and macro model for stress-resultant failure criteria in frame	38
3.1 Stress-resultant macro model for reinforced concrete frames and chosen material behavior of concrete and reinforcement	38
3.2 Parameter identification for doubly reinforced concrete rectangular section	41

3.3	Function identification for moment-axial force relation	48
3.4	Function identification for curvature-axial force relations	51
3.5	Moment and curvature yield functions for stress-resultant macro model at the time t	55
4	Numerical applications	56
4.1	Single-element console computation	57
4.2	Two-storey reinforced concrete frame computation	59
5	Conclusion	66
3	Stress resultant and multi-fiber beam model with shear failure and crack spacing	69
1	Introduction	71
2	Reinforced concrete model and its finite element implementation	72
2.1	Concrete, bond-slip and steel models	72
2.2	Numerical formulation of the reinforced concrete element	76
2.3	Numerical examples	78
3	Stress-resultant macro model: embedded displacement discontinuities	81
3.1	Theoretical formulation and finite element representation	83
3.2	Stress-resultant constitutive laws	88
4	Numerical examples	91
5	Conclusions	93
	Conclusion	95
	Bibliography	97

List of Figures

1	Standard design procedure and performance based design procedure	2
1.1	Displacement discontinuities in the Euler-Bernoulli beams	6
1.2	Rotation and curvature discontinuity description in the beam element	7
1.3	Moment-rotation behavior at the discontinuity point of beam element	8
1.4	Timoshenko beam-column element with different kind of external loads	8
1.5	2D bar element and shapes of the interpolation functions	9
1.6	Moment-Curvature relation for stress resultant macro model	13
1.7	Considered beam and fibers in the element	15
1.8	Behaviors of concrete and steel	19
1.9	Reinforced concrete beam in computation	21
1.10	Beam diagram in computation	21
1.11	Relation of reaction and vertical displacement	22
1.12	RC frame diagram in computation and experiment	24
1.13	Elements to compute beam and column	25
1.14	Relation of moment-curvature for representative beam and column .	25
1.15	Rotational displacement of frame	26
1.16	Relation of lateral load versus deflection at top storey of frame	27
2.1	Stress-strain curve of steel for design	33
2.2	Stress-strain curve of concrete in compression of experiment	34
2.3	Ultimate strains in members under compression	35
2.4	Parabolic-rectangular curve in compressive zone of bending beam . .	35
2.5	Prediction for ultimate moment-axial force relation	37
2.6	Imposed axial load and rotation in multi-fiber and stress-resultant beam-column element	38
2.7	Stress-resultant macro model for frames	39
2.8	Material behaviors of concrete and reinforcement	40
2.9	Multi-fiber beam-column diagram for parameter identification	42
2.10	Geometry of reinforced concrete built-in beam-column for parameter identification	43
2.11	Axial force identification for rectangular cross-section	43
2.12	Moment-curvature relations obtained by multi-fiber beam-column model based computations	44

2.13	Stress-time fiber curve and moment-time curve	45
2.14	Moment-curvature diagrams in the refined curves	46
2.15	Cracking, yielding and ultimate moments with respect to N/N_y ratio .	47
2.16	Prominent curvature values ($\kappa_c, \kappa_y, \kappa_u, \kappa_p$) with respect to $n= N/N_y$ ratio	48
2.17	Best-fit function for cracking moment M_c variation with respect to $n= N/N_y$	49
2.18	Best-fit function for yielding moment M_y variation with respect to $n= N/N_y$	50
2.19	Best-fit function for ultimate-moment M_u variation with respect to $n= N/N_y$	51
2.20	Function of curvature κ_c with $n= N/N_y$	52
2.21	Best-fit function for curvature at yield moment variation with respect to N/N_y	53
2.22	Best-fit function for curvature at ultimate moment variation with respect to N/N_y	54
2.23	Best-fit function for curvature at rupture point κ_p variation with respect to $n=N/N_y$	55
2.24	Axial loading program and its time evolution	57
2.25	Multi-fiber computation for reinforced concrete single-element console .	58
2.26	Stress-resultant beam macro computation for reinforced concrete single-element console	58
2.27	Change of cracking moment M_c	59
2.28	Change of yield moment M_y	60
2.29	Change of ultimate moment M_u	60
2.30	Change of crack-curvature κ_c	61
2.31	Change of yield-curvature κ_y	61
2.32	Change of ultimate-curvature κ_u	62
2.33	Change of curvature κ_p	62
2.34	Change of hardening tangent K_1	63
2.35	Change of hardening tangent K_2	63
2.36	Change of softening tangent K_3	64
2.37	Detail of two-storey reinforced concrete frame	65
2.38	Rotation displacement of frame in computation	65
2.39	Transversal load and deflection in frame	66
3.1	Kinematics of the macro element and enriched finite element	77
3.2	Four point bending test on RC specimen: geometry, loading and finite element mesh	79
3.3	Bond-slip along the bar and crack pattern for the first macro-cracks .	79
3.4	Cracks pattern at an advance loading stage	80
3.5	Displacement field along axis Y	80
3.6	Global response for the heavy reinforcement	80

3.7	Cracks opening in the RC specimen	81
3.8	Cracks pattern and bond slip sliding	82
3.9	Global response for weak reinforcement	82
3.10	General beam diagram for stress-resultant model	83
3.11	Beam element and shapes of interpolation function	84
3.12	Description of transverse displacement and rotation discontinuities in beam element	85
3.13	Moment-Curvature relation for stress resultant macro model	90
3.14	Geometry and details of beam in the four-point bending test	91
3.15	Computational diagram and post transverse displacement of tested beam	92
3.16	Global behavior of support reaction and deflection of tested beam	93

List of Tables

3.1	Main ingredients of the construction of the two damage models	73
-----	---	----

Introduction

Reinforced concrete is perhaps the most widely used material in construction, for all components from the foundations until the roof in general civil structures, such as the buildings and bridges, or in special constructions as the dams, the tunnels, the roads and the runways for takeoff and landing in the airport. The recent development in the field of finite element computation resulting with very fast codes, with the support of strong computer, allows that the computation for the complex structure be considered with the aim to optimize design for both the local, element level (such as for the slab, the beam or the column) and the global, structural level (frame, walls, shell ...).

The standard design procedure of reinforced concrete frame structures starts with linear analysis to obtain the corresponding diagrams of stress resultants (bending moment, shear and axial force), followed by the ultimate analysis of each cross section. The main disadvantage of such a design procedure concerns the (highly) statically indeterminate frames, where the failure of each beam or column would not imply the complete failure of the structure, but would lead to a significant stress resultant redistribution with respect to the result obtained by linear analysis (see Figure 1).

For that reason, we propose the performance based design procedure where the behavior until complete failure of beam-column and frames imposes to consider so-called plastic hinges corresponding to the zones where plasticity and/ or damage localizes. Engineering structures are usually statically indeterminate, so that the total failure of one member would affect the global response of the structure but it would not lead to a complete loss of the structural integrity. Moreover, being capable of describing the softening response of the members of one particular structure can provide an estimate of the residual life of a partially damaged structure. Such a procedure can also help to provide a more detailed crack description, which is needed to make decisions about the maintenance and repairs.

Objectives:

The aim of this work is to provide an efficient tool for the optimal design of reinforced concrete frames under the extreme loading. A multi-scale approach has been adopted. Three levels of refinement are considered:

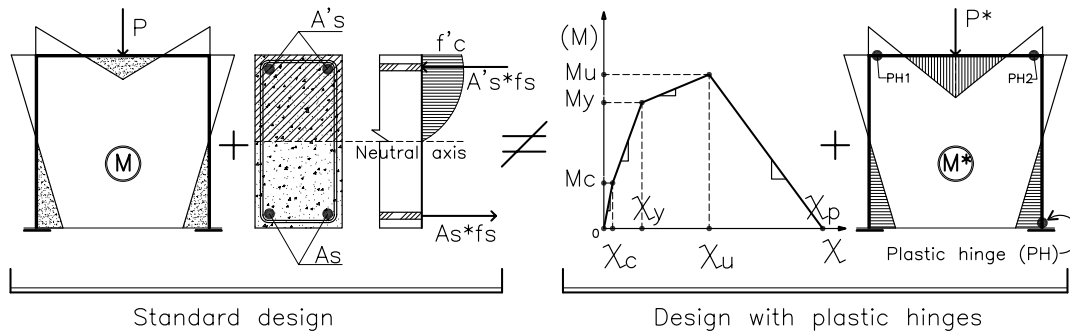


Figure 1: Standard design procedure and performance based design procedure

- at the global level, a force resultant model has been implemented in a Timoshenko beam element with strong rotation discontinuity,
- at the semi-global level, a uniaxial model has been implemented in a multi-fiber beam element with strong discontinuities in the fibers,
- at the local level, a 2D solid modeling of the reinforced concrete is used, based on previous works [1] [53], including cracking of concrete and bond slip behavior between steel and concrete.

Proposed approach:

The non linear response of the whole structure is computed in two steps:

- in the beginning, the moment-curvature behavior of a section of each beam or column of the frame is computed with the multifiber element (embedded on one end and with an imposed rotation on the other end), and then the parameters of the global Timoshenko beam element are identified. Since there is only one element used for these computations, they are very fast to carry out.
- after that, the response of the frame structure can be computed fast by using the three degree of freedom Timoshenko beam elements with a global model. Since these elements are able to represent the softening of the cross sections and the rotation discontinuities due to the cracks, it is possible to compute the force redistributions in a statically indeterminate structure until global failure.

This basic idea needs at least two main improvements:

- the influence of the axial force on the bending curvature response must be taken into account, especially in the columns. It has been done while introducing a parameter depending on the rate of axial force in the global model.
- when dealing with softening, the size of the elements is of almost importance. Since the global Timoshenko beam elements model both the spread plasticity/damage along the element and the discontinuity due to the cracking concentrated at the middle of the element, the length of an element is guided by the crack spacing in the structure. This crack spacing is very much related to the bond-slip behavior. The local 2D model is used to determine this spacing and identify the length of the softening elements. Moreover, the 2D model is also used to identify the descending branch of the global model with proper value of fracture energy considerations.

Thesis outline:

The first chapter of this document presents first the implementation of the strong rotation discontinuity in a Timoshenko beam element to model reinforced concrete frames. Then it presents the implementation of strong discontinuities in fibers to model the concrete cracking in the multifiber beam elements, and to have a reliable and efficient tool for the identification of the parameters of the global model. Some examples are presented where the parameters of the global model were identified with constant axial forces. They are compared to fit the experimental results.

The second chapter focusses on the influence or the variation of axial forces. After an explanation of the standard code and usual methods, the modification of the yield functions to introduce the axial force are presented. The parameters of the global model are now functions of the axial force. The improvement of the response of some structures is shown and compared to test results.

The third chapter first recalls some earlier results on the 2D modelling of reinforced concrete structures including cracking of concrete and bond slip between steel and concrete modeling. It then presents an example how to take into account the crack spacing for determining the size of the global elements and how to identify the parameters of the global model taking into account the influence of the bond slip.

Chapter 1

Stress resultant and multi-fiber beam model for bending failure

In this chapter, we present a new finite element for Timoshenko beam model for ultimate load computation of reinforced concrete frames. The proposed model combines the descriptions of the diffuse plastic failure in the beam-column followed by the creation of plastic hinges due to the failure or collapse of the concrete and or the re-bars. A modified multi-scale analysis is performed in order to identify the parameters for stress-resultant-based macro model, which is used to describe the behavior of the Timoshenko beam element. The micro-scale is described by using the multi-fiber elements with embedded strain discontinuities in mode I, which would typically be triggered by bending failure mode.

Contents

1	Introduction	6
2	Embedded rotation discontinuity for Timoshenko beam	7
3	Multi-fiber beam model with embedded strain discontinuity in fibers .	14
3.1	Multi-fibers beam model	14
3.2	Embedding strain discontinuity in fiber	15
3.3	Assembly of all fibers in a beam element	16
3.4	Constitutive laws of the concrete and the steel	18
4	Numerical examples	20
4.1	Reinforced concrete simple beam	21
4.2	Two-storey frame ultimate load computation	23
5	Conclusions	27

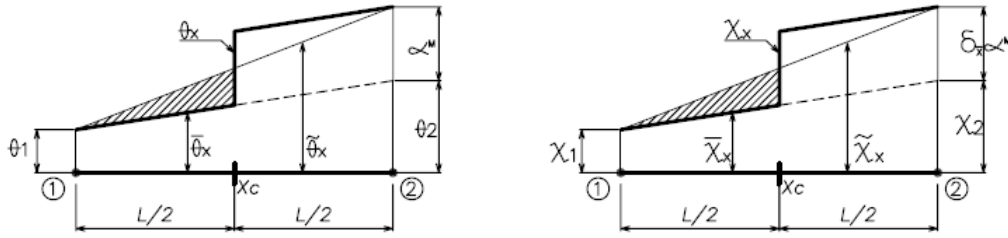


Figure 1.2: Rotation and curvature discontinuity description in the beam element

In order to describe the softening behavior of the hinge, a relation of bending moment/rotation is introduced at the discontinuity. Moreover, in order to identify the precise form and corresponding parameters of this relation in the case reinforced concrete members, we propose a multi-scale type analysis. The fine behavior of the member is computed using a multi-fiber element analysis, where each concrete fiber is considered as a bar element enriched with strain discontinuity and the compression phase different from the tension phase. The behavior of re-bars fibers is also considered as the bar elements with embedded strain discontinuity in two phase of compression and tension. From this micro-scale analysis, we can identify the parameters of the bending moment/rotation relationship introduced on the hinge at the macro level. We also present the combination of all fibers in one element, this procedure is presented in details in Section 3.

In Section 4, a method for obtaining the parameters as the tangent modulus and limit values of bending moment M_c M_y M_u and corresponding curvature κ_c κ_y κ_u is presented. It also includes the numerical application for two specific examples, a three point bending beam and a two-storey reinforced concrete frame. Finally, in the last section, some chapter conclusions are given.

2 Embedded rotation discontinuity for Timoshenko beam

We present in this section the main ingredients allowing to embed a rotation discontinuity in Timoshenko beam-column elements. Particular attention is paid to the kinematic enrichment and the modification of the weak equilibrium equation. We also give some details on the finite element implementation of such a method. At the end of this section, some threshold functions used in computation of the stress-resultant beam macro model are presented.

Theoretical formulation and numerical implementation

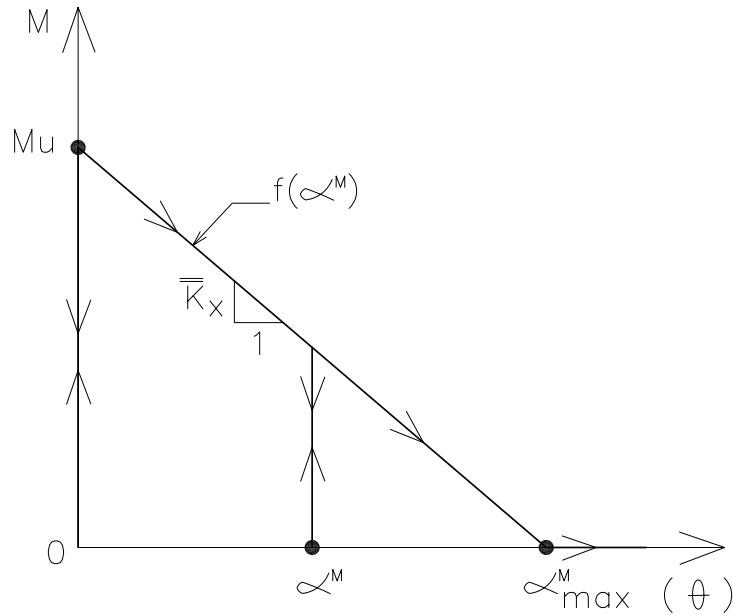


Figure 1.3: Moment-rotation behavior at the discontinuity point of beam element

We introduce a Timoshenko beam-column with different kind of external loads and imposed displacements: $f(x)$, $q(x)$, $m(x)$ are considered as the distributed loads along the beam-column element and F , T , C are considered as the concentrated loads, axial force, transversal force and moment. In Figure 3.10, u v will denote the axial and transversal displacements of the mean line of the beam-column element and θ the rotation of its cross section. Point Γ_d and point Γ_t are considered as the imposed displacement points and concentrated loads as the boundary conditions. With this notation in hand, the strong form of equilibrium equations and kinematic formulations for the case 2D of Timoshenko beam-column can be written as follows:

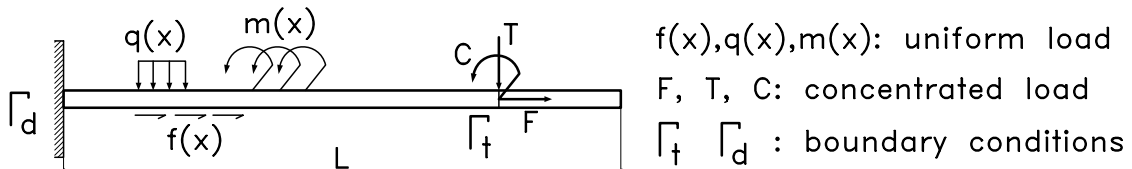


Figure 1.4: Timoshenko beam-column element with different kind of external loads

Equilibrium equations in stress resultants:

$$\frac{dM}{dx} + T(x) + m(x) = 0; \quad \frac{dN}{dx} + f(x) = 0; \quad \frac{dT}{dx} + q(x) = 0; \quad (1.1)$$

Kinematics of Timoshenko beam

$$\varepsilon_x = \frac{dU_x}{dx}; \gamma_x = \frac{dV_x}{dx} - \theta_x; \kappa_x = \frac{d\theta_x}{dx}; \quad (1.2)$$

The constitutive equations for stress resultant, axial load, shear load and bending moment

$$\begin{aligned} N &= EA\varepsilon \\ V &= kGA\gamma \\ M &= EI\kappa \end{aligned} \quad (1.3)$$

Considering further for this problem the finite element aspects, the 2D beam-column element with two nodes is chosen, with the length l^e . The point x_c is placed in the middle of element to describe kinematic enhancement (see Fig. 1.5 below). The classical displacement field based on the linear interpolation functions can be described

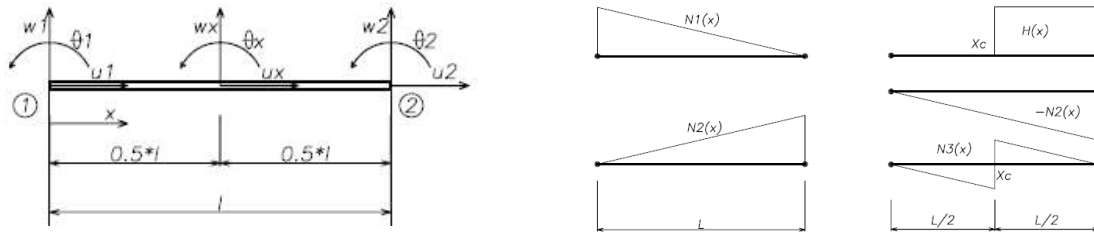


Figure 1.5: 2D bar element and shapes of the interpolation functions

$$\begin{aligned} U(x) &= N_1(x)U_1 + N_2(x)U_2 = N(x)u \\ V(x) &= N_1(x)V_1 + N_2(x)V_2 = N(x)v \\ \theta(x) &= N_1(x)\theta_1 + N_2(x)\theta_2 = N(x)\theta; \end{aligned} \quad (1.4)$$

where $N_1(x) = 1 - \frac{x}{l^e}$; $N_2(x) = \frac{x}{l^e}$

With the purpose of embedding the rotation discontinuity in the rotational function, the incompatible mode method [6] is used to enrich the classical rotational displacement interpolation. Rotational function in (1.4) can thus be re-written as

$$\begin{aligned} \theta(x) &= N_1(x)\theta_1 + N_2(x)\theta_2 + N_3(x)\alpha \text{ or} \\ \theta(x) &= N_1(x)\theta_1 + N_2(x)\theta_2 + (H_\Gamma - N_2(x))\alpha \end{aligned} \quad (1.5)$$

In the last expression we used the Heaviside function H_Γ , described as $H_\Gamma = \begin{cases} 0 & \text{if } x < 0 \\ 1 & \text{if } x \geq 0 \end{cases}$

With a new interpolation function for the rotation in hand, the regular part and the singular part are separated. The curvature κ of the element can be also decomposed into a regular part and a singular part and written as

$$\kappa(x) = \bar{\kappa}(x) + \alpha \delta_{\bar{x}}(x) \quad (1.6)$$

In the spirit of incompatible mode method, (see [1] and [6]), the added part $N_3(x)\alpha$ is used only for the construction of enrichment in the curvature interpolation. Hence, the new form of element deformations can be now written as

$$\begin{aligned} \varepsilon(x) &= Bu \\ \gamma(x) &= Bv - N\theta \\ \kappa(x) &= B\theta + G_r\alpha \end{aligned} \quad (1.7)$$

where B is $\{-\frac{1}{l^e}; \frac{1}{l^e}\}$ and G_r is $\frac{d}{dx}N_3(x)$. The term $N_3(x)$ in (1.5) is described for the discontinuity part, which implies that G_r in (1.7) can also be decomposed into a regular part \bar{G}_r and a singular part $\bar{\bar{G}}_r$

$$G_r = \bar{G}_r + \bar{\bar{G}}_r \quad (1.8)$$

with $\bar{G}_r = -\frac{1}{l^e}$ and $\bar{\bar{G}}_r = \delta_{\bar{x}}(x)$. We denote $\{\varepsilon\}^T = [\varepsilon \ \gamma \ \kappa]$ as the beam-column deformation, with the general deformation form that can be expressed as $\varepsilon = BD + G_r\alpha$ with

$$B = (B_1, B_2); \text{ with } B_i = \begin{bmatrix} \frac{dN_i}{dx} & 0 & 0 \\ 0 & \frac{dN_i}{dx} & -N_i \\ 0 & 0 & \frac{dN_i}{dx} \end{bmatrix}; \quad (1.9)$$

The enhanced interpolation G_r of bending strain can be expressed as the matrix form correlated to the components of deformations:

$$G_r = \begin{bmatrix} 0 \\ 0 \\ -\frac{1}{l^e} \end{bmatrix} + \begin{bmatrix} 0 \\ 0 \\ 1 \end{bmatrix} \delta_{Xc}$$

We also denote with $\{d\}^T = [U_1 \ V_1 \ \theta_1; U_2 \ V_2 \ \theta_2]$ the displacement vector of the beam-column element and with d^* its variation.

From those interpolations, the virtual displacement field of the beam-column element is written as $\{d^*\}^T = [u^* \ v^* \ \theta^*]$, and assumed to be kinematically admissible *i.e* equal to 0 at the point Γ_d . The virtual deformation field is denoted as $\eta^* = Bd^* + G_v\beta^*$, where G_v is deduced from G_r by imposing the patch test $\int_0^{l^e} G_v dx = 0$. Following the idea presented in [6], we propose to choose $G_v = G_r - \frac{1}{l^e} \int_0^{l^e} G_r dx$. Note that G_v can be also decomposed into regular and singular parts, $G_v = \bar{G}_v + \bar{\bar{G}}_v \delta_{Xc}$, where $\bar{G}_v^T = [0 \ 0 \ -\frac{1}{l^e}]$ and $\bar{\bar{G}}_v^T = [0 \ 0 \ 1]$.

Appealing to the incompatible modes method introduced in [1] and [6], the weak form of the equilibration equation can be written for two levels, global concerning all the nodes $\forall d^*$ of the chosen mesh and local concerning all the elements $\forall \beta^*$

$$\int_0^{l^e} d^{*T} B^T \begin{bmatrix} N \\ T \\ M \end{bmatrix} dx - \int_0^{l^e} d^{*T} N^T \begin{bmatrix} f(x) \\ q(x) \\ m(x) \end{bmatrix} dx - \int_{\Gamma} d^{*T} N^T \begin{bmatrix} F \\ Q \\ C \end{bmatrix} d\Gamma = 0; \quad \forall e \quad (1.10)$$

$$\int_0^{l^e} \beta^* \bar{G}_v^T \begin{bmatrix} N \\ T \\ M \end{bmatrix} dx - \int_0^{l^e} \beta^* \bar{G}_v^T \begin{bmatrix} N \\ T \\ M \end{bmatrix} \delta_{x_c} dx = 0; \quad \forall e$$

The second of equations in (1.10)- the local equation- is written only in each element where plastic hinge occurs. The main contribution of this equation is control the amount of the rotation jump α , decoupled from element to another. This local equation can be interpreted as a weak form of the bending moment continuity condition across the discontinuity.

Finally, we can obtain the following system with reducing the components of N and T in the second of equations (1.10)

$$A_{e=1}^{nel} [f^{int(e)} - f^{ext(e)}] = 0; \quad (1.11)$$

$$h^e = 0; \quad \forall e \in [1, nel]$$

Where A is the finite element assembly procedure and

$$f^{int(e)} = \int_0^{l^e} B^T \begin{bmatrix} N \\ T \\ M \end{bmatrix} dx;$$

$$f^{ext(e)} = \int_0^{l^e} N^T \begin{bmatrix} f(x) \\ q(x) \\ m(x) \end{bmatrix} dx + \int_{\Gamma} N^T \begin{bmatrix} F \\ Q \\ C \end{bmatrix} d\Gamma; \quad (1.12)$$

$$h^e = \int_0^{l^e} \bar{G}_v^T M dx + M_{(x=x_c)}$$

We can consider the case where the material outside the discontinuity is non-linear, with a constitutive equation of the form

$$\dot{\sigma} = D^{in} \dot{\bar{\epsilon}} = D^{in} (B \dot{d} + \bar{G}_r \dot{\alpha}); \quad \text{with } \{\sigma\}^T = [N, T, M] \quad (1.13)$$

and the moment-rotation jump relation can be written as

$$\dot{M}_{x_c} = K_{x_c} \dot{\alpha} \quad (1.14)$$

For such a case the equations (1.11) can be written in the incremental form

$$\begin{aligned} A_{e=1}^{nel} \left[K^e \Delta d + F_r \Delta \alpha - f^{ext(e)} \right] &= 0; \text{ and} \\ F_v^T \Delta d + H \Delta \alpha + K_{x_c} \Delta \alpha &= 0 \quad \forall e \in [1, nel] \end{aligned} \quad (1.15)$$

where

$$\begin{aligned} K^e &= \int_0^{l^e} B^T D^{in} B dx; \quad F_r = \int_0^{l^e} B^T D^{in} \bar{G}_r dx \\ F_v &= \int_0^{l^e} B^T D^{in} \bar{G}_v dx; \quad H = \int_0^{l^e} \bar{G}_v^T D^{in} \bar{G}_r dx \end{aligned}$$

This set of equations is solved by using the operator split method, (see [1]). Namely, we first solve local equation in each localized element for a fixed value of total displacement d , so that we can determine the value of the rotation jump α . Then by static condensation at the element level, the first equation in (1.15) turns into

$$A_{e=1}^{nel} \left[\hat{K}^e \Delta d - f^{ext(e)} \right] = 0; \text{ with } \hat{K}^e = K^e - F_r (H + K_{x_c})^{-1} F_v^T \quad (1.16)$$

The solution to (1.16) will give the corresponding displacement increment and a new value of the displacement d .

We assume in the following that the axial and transverse responses of the beam material remains elastic. As regards the bending moment and as suggested previously, we use two different stress-resultant models (see Figure 3.13):- a stress-resultant elasto-plastic model with two linear hardening phases to deal with the bulk behavior; - and a rigid-plastic model with linear softening to deal with the formation and development of plastic hinges.

Four yield functions are thus introduced to process the beam material behavior :

$$\begin{aligned} \Phi^M(M, \zeta_i^M) &:= |M| - (M_i + K_i I \cdot \zeta_i^M) \leq 0 \\ \text{if } i = 1 &: \text{hardening phase 1} \Rightarrow M_i = M_c; K_i = K_1 \text{ and } \zeta_i^M = \zeta_1^M \\ \text{if } i = 2 &: \text{hardening phase 2} \Rightarrow M_i = M_y; K_i = K_2 \text{ and } \zeta_i^M = \zeta_2^M \\ \text{if } i = 3 &: \text{softening phase} \Rightarrow M_i = M_u; K_i = K_3 \text{ and } \zeta_i^M = \zeta_3^M \\ \text{if } i = 4 &: \text{complete rupture} \Rightarrow M_i = 0; K_i = 0 \text{ and } \zeta_i^M = \zeta_4^M \end{aligned}$$

where M_c, M_y, M_u denote the cracking moment, yield moment and ultimate moment. I

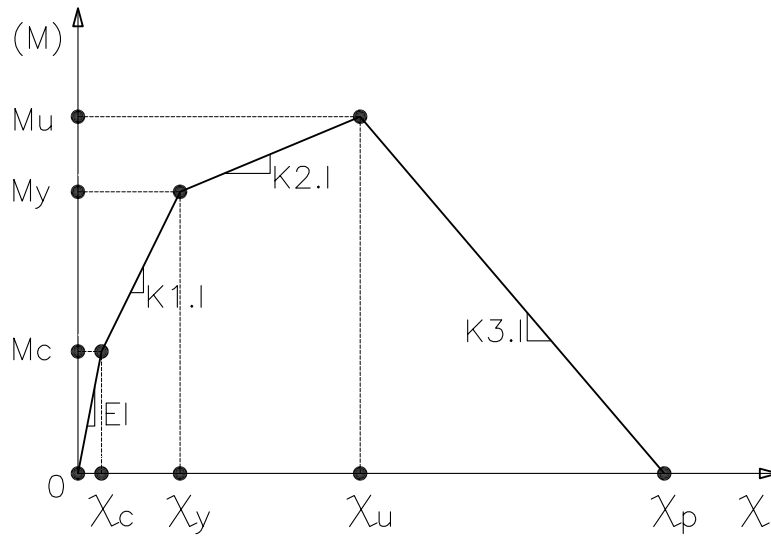


Figure 1.6: Moment-Curvature relation for stress resultant macro model

denotes the cross-section inertia and K_i denote the different hardening/softening moduli. We can note that K_{x_c} introduced previously is equal to K_3I . In the next section, a method for obtaining the values D^{in} , K_i and K_{x_c} will be described in more detail and the multi-fiber beam model will also be introduced.

3 Multi-fiber beam model with embedded strain discontinuity in fibers

In this section we present shortly about the multi fibers beam model, which provides the basis for identifying the parameters of stress resultant model. This multi-fiber model is helpful to analyse and handle a beam-column with multi materials embedded in one cross-section in general or for reinforced concrete in particular. In this method, we also present the steps for embedding strain discontinuity in each fibers, including concrete fibers and steel reinforced fibers. The constitutive laws of concrete and steel are introduced as the corresponding Elasto-Plastic material models with softening.

3.1 Multi-fibers beam model

The beam in Fig. 1.7 is introduced as the fine micro scale beam model used to explore the details of inelastic constitutive behavior of material such as the reinforced concrete. The analysis of this kind is quite equivalent to nonlinear homogenization, which will provide the best possible definition of ('macro') stress resultant beam model. The analysis is carried out on the built-in beam with the length L , divided in a number of elements with length l^e . The beam rectangular cross-section with the width b and the depth h is divided into a number of concrete fibers and reinforced fibers. The coordinate y_i denotes the distance from the neutral line to the centre of a given fiber. This beam is further submitted to a loading program with a constant value of axial force N and an increasing value of moment M applied at free end.

For each fiber we can obtain its axial and shear strains depending upon the element displacements, which include the axial displacement U_x and the rotation displacement θ_x corresponding to the couple N and M

$$\epsilon_x^i = \frac{dU_x}{dx} - y_i \frac{d\theta_x}{dx}; \quad 2\epsilon_{xy}^i = \frac{dV_x}{dx} - \theta_x \quad (1.17)$$

In accordance to the material behavior, the stresses in each fibers can be written as

$$\sigma_x^i = D^{in} \epsilon_x^i; \quad \sigma_{xy}^i = 2G^{in} \epsilon_{xy}^i \quad (1.18)$$

The corresponding values of stress resultants in each cross section can be computed by summing up all stresses in fibers; we thus obtain the axial force N , the shear force V and the bending moment M defined as

$$N = \int_S \sigma_x dS; \quad V = \int_S \sigma_{xy} dS; \quad M = - \int_S y^2 \sigma_x dS; \quad (1.19)$$

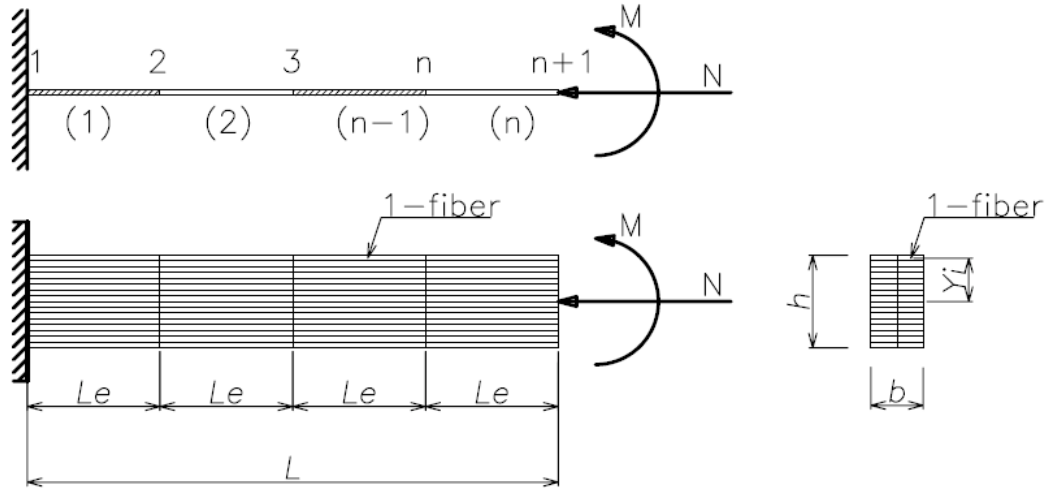


Figure 1.7: Considered beam and fibers in the element

3.2 Embedding strain discontinuity in fiber

Each fiber of this beam element can be considered as a truss-bar element, for which the stress-strain behavior is selected as either concrete or steel material. For any fiber placed at any point in the cross section, we will consider that the strain discontinuity can be embedded (see [1] and [2]). The fiber axial strain can be split into the regular part and singular part

$$\epsilon_x^i = \bar{\epsilon}_x^i + \alpha^i \delta_{x_c}^i \quad (1.20)$$

If the fiber response is non-linear, the fiber strain depends on element displacement and fiber strain discontinuity parameters α^i , this can be written as

$$\epsilon_{x,t}^i = \sum_{a=1}^2 B_a d_{a,t} + \tilde{G} \alpha^i \quad (1.21)$$

From each fiber strain, the stress can easily be computed by multiplying with tangent modulus of material

$$\sigma_{x,t}^i = \hat{C} \epsilon_{x,t}^i = \hat{C} \left[\sum_{a=1}^2 B_a d_{a,t}^i + \tilde{G} \alpha_t^i \right] \quad (1.22)$$

Thanks to the standard kinematic hypothesis for Timoshenko beam, the displacement $d_{a,t}^i$ in each fiber is computed from the nodal displacement of beam element as well as the fiber coordinate y^i , $d_x^i = \dot{U}_x - y^i \dot{\theta}_x$. The stress computed in each fiber is used to obtain the corresponding contribution to the stress resultant internal force. Moreover, this stress has to satisfy the local equivalent equation, which is solved in each localized fiber with a fixed value of displacement $d_{x,t}^i$, where α_t^i is the axial displacement jump of fiber level, whereas $t(\alpha^{fib})$ is considered as the corresponding stress value at the discontinuity point X_c . The latter can be expressed as a function $\bar{t} = \bar{K}_{X_c} \alpha$, where tangent modulus \bar{K}_{X_c} is dependent on the type of fiber material. The threshold function $\Phi(t, \bar{q}) := |\bar{t}| - (\sigma_y - \bar{q}) \leq 0$ is used to manage the stress \bar{t} , with only zero value indicating further changes

$$\begin{aligned} f^{fib,int} &= \int_0^{l^{fib}} B^T \sigma(d, \alpha^{fib}) dx \\ h^{e,fib} &= \int_0^{l^{fib}} \tilde{G}^T \sigma(d, \alpha^{fib}) dx + t(\alpha^{fib}) = 0 \\ &\text{with } \forall e \in [1, n_{elmt}] \text{ and } \forall fib \in [1, m_{fiber}] \end{aligned} \quad (1.23)$$

3.3 Assembly of all fibers in a beam element

Assembly of all fibers in a beam element is process by which the program computes the internal forces N , V , and M , and then proceeds to the residual computation, which is repeated for each iteration. In the computation process, the internal energy and the total dissipation are always assured with the equivalence between element level and multi fibers level. The description of equivalence for the internal energy can be described as

$$\Psi_{elmt} = \sum_{i=1}^{n_{fib}} \Psi_i^{fib} \quad (1.24)$$

and the equivalence of dissipation can be expressed as, where the subscripts $elmt$ and fib indicates, respectively, a particular element and a particular fiber

$$D_{elmt} = \sum_{i=1}^{n_{fib}} D_i^{fib} \quad (1.25)$$

On other hand, the contribution in the internal energy or the dissipation at global level should be matched by the energy of the external forces, such as axial force, shear force, and bending moment, denoted with subscripts N , V , and M , respectively.

$$\begin{aligned} \Psi_{elmt} &= \Psi_{elmt}^N + \Psi_{elmt}^V + \Psi_{elmt}^M \\ D_{elmt} &= D_{elmt}^N + D_{elmt}^V + D_{elmt}^M \end{aligned}$$

In the presence of the dissipation at the fiber level, both internal energy and dissipation can be split into a regular part and a singular part, (see [2]).

$$\begin{aligned}\Psi_i^{fib}(\boldsymbol{\varepsilon}, \bar{\zeta}, \bar{\bar{\zeta}}) &= \bar{\Psi}_i^{fib}(\boldsymbol{\varepsilon}, \bar{\zeta}) + \bar{\bar{\Psi}}_i^{fib}(\bar{\bar{\zeta}})\delta_{xc} \\ D_i^{fib} &= \int_0^{l^e} [\sigma^{fib}\dot{\boldsymbol{\varepsilon}}^p + \bar{q}^{fib}\dot{\bar{\zeta}}] dx + \left[\bar{\bar{q}}^{fib}\dot{\bar{\zeta}} \right]_{|_{xc}}\end{aligned}$$

The first part affects all the points along the fiber and the second part affects only the discontinuity point Xc , placed in the middle of fiber. With two independent parts in fiber level, the internal energy and dissipation of the element level can be also written with a split between the regular and the singular part:

$$\begin{aligned}\Psi_{elmt} &= \bar{\Psi}_{elmt} + \bar{\bar{\Psi}}_{elmt} \\ D_{elmt} &= \bar{D}_{elmt} + \bar{\bar{D}}_{elmt}\end{aligned}\tag{1.26}$$

The regular parts of internal energy and dissipation at element level can be written as

$$\bar{\Psi}_{elmt} = \sum_{i=1}^{n_{fib}} \bar{\Psi}_i^{fib}(\boldsymbol{\varepsilon}, \bar{\zeta}); \quad \bar{D}_{elmt} = \sum_{i=1}^{n_{fib}} \int_0^{l^e} [\sigma^{fib}\dot{\boldsymbol{\varepsilon}}^p + \bar{q}^{fib}\dot{\bar{\zeta}}] dx$$

and the singular part of internal energy and dissipation at element level can be written from the sum of singular parts at fiber level as

$$\bar{\bar{\Psi}}_{elmt} = \sum_{i=1}^{n_{fib}} \bar{\bar{\Psi}}_i^{fib}(\bar{\bar{\zeta}})\delta_{xc}; \quad \bar{\bar{D}}_{elmt} = \sum_{i=1}^{n_{fib}} \left[\bar{\bar{q}}^{fib}\dot{\bar{\zeta}} \right]_{|_{xc}}$$

We can thus conclude that if the local failure appears in any element fiber, concrete or reinforcement, this local failure phenomena will accounted for at the element level.

The element stiffness matrix form can be presented as

$$[K_{elmt}] = \int_0^{l^e} [B]^T [K_s] [B] dx\tag{1.27}$$

Where axial and bending terms are coupled, whereas the shear term remains uncoupled. The section stiffness K_s can be written as in the matrix form with components corresponding to three displacement vectors U , V , and θ

$$[K_s] = \begin{bmatrix} K_{s11} & 0 & K_{s13} \\ 0 & K_{s22} & 0 \\ K_{s31} & 0 & K_{s33} \end{bmatrix} \quad \begin{aligned} K_{s11} &= \int_S E dS & K_{s22} &= k \int_S G dS \\ K_{s33} &= \int_S y^2 E dS & K_{s13} &= K_{s31} = - \int_S y E dS \end{aligned}$$

That process can start from the first step of forming the section stiffness followed by the second step to compute the integrals along the element length to finally obtain the stiffness matrix K_{elmt} . We use such method to compute two components of element stiffness matrix K_{elmt}^{11} and K_{elmt}^{22} , but the component K_{elmt}^{33} corresponds to the rotational displacement and can be computed in somewhat modified way as

$$\begin{aligned} K_{elmt}^{33} &= \int_S \left[K_{fib} - F_{fib,V}^T H_{fib}^{-1} F_{fib,R} \right] dS \\ &= \int_S [K_{fib}] dS - \int_S \left[F_{fib,V}^T H_{fib}^{-1} F_{fib,R} \right] dS \end{aligned} \quad (1.28)$$

In the second form of the beam tangent stiffness in (1.28), the first term can be obtained from the classical method and the second term corresponds to the effect of rotational discontinuity. All contribution of the particular fiber to the element stiffness matrix K_{elmt}^{33} can be computed as:

$$\begin{aligned} K_{fib} &= \int_0^{l^e} B_a^T (\hat{C}_{fib} A_{fib}) y_{fib}^2 B_a dx; \quad F_{fib,V} = \int_0^{l^e} B_a^T (\hat{C}_{fib} A_{fib}) y_{fib}^2 \bar{G} dx \\ F_{fib,R} &= \int_0^{l^e} \bar{G}^T (\hat{C}_{fib} A_{fib}) y_{fib}^2 B_a dx; \quad H_{fib} = \int_0^{l^e} \bar{G}^T (\hat{C}_{fib} A_{fib}) y_{fib}^2 \bar{G} dx - (\bar{\bar{K}}_{fib} A_{fib}) y_{fib}^2 \end{aligned}$$

Two components \bar{G} and B_a can be used as the same as those in (1.8) and (1.9). The parameters \hat{C}_{fib} and $\bar{\bar{K}}_{fib}$ can be obtained from the material properties. The cross area of fiber A_{fib} and the distance from the neutral line to the fiber centre y_{fib} pictured in the Fig.3.1

3.4 Constitutive laws of the concrete and the steel

In this part we present two constitutive models for concrete and steel materials referred to as Elasto-Plastic-Softening (EPSM). Either model is developed to include the strain discontinuity introduced in the previous section 3.2, ([2]). In the constitutive law of concrete, the compression phase and the tension phase are different. For the concrete material, the Young modulus is denoted as E_b , the ultimate stress and the plastic stress in the compression phase are denoted as f'_c and f_{yc} , the ultimate stress in the tension phase is denoted as f_t . All these values of stress are correlated with the different strains ϵ_u , ϵ_y and ϵ_t , which can be obtained from the simple tests of the concrete sample.

For clarity we picture the concrete model with the stress/strain relation described in Fig.3.4. We denote with K_1 the hardening tangent value of the compression phase, and with K_2 and K_3 we denote for the softening phases in compression and tension. In the

computation, they are used as the negative values (see [2]).

All values of the Young modulus, strength, tangent modulus for both hardening and softening phases are also compared to the other model. In the tension phase, no hardening part is considered. Therefore, the stress reaching the ultimate value f_t , will trigger the softening response with the tangent modulus $K_3 < 0$.

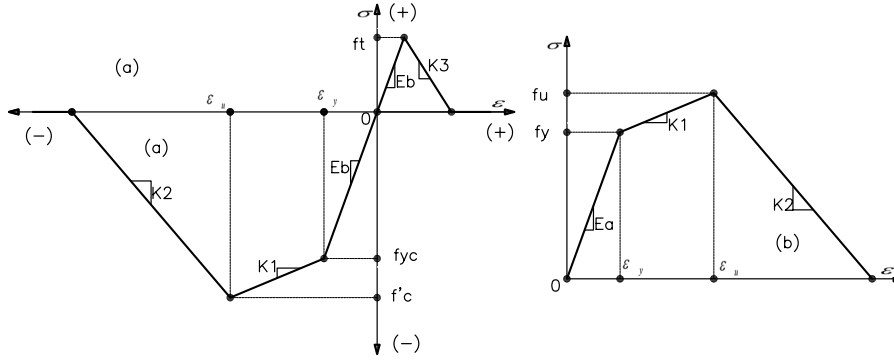


Figure 1.8: Behaviors of concrete and steel

In numerical computation, the plasticity model with combined hardening and softening [2] is applied for representation of the concrete constitutive laws. There are two different yield functions used in the compression phase hardening and softening along with the yield function governing the tensile failure. All these yield functions are defined below:

$$\begin{aligned}
 \Phi^c(\sigma, \bar{\zeta}_i) &:= |\sigma| - (\sigma_i^c + \bar{K}_i^c \bar{\zeta}_i) \leq 0 \\
 \text{if } i = 1 &:\text{hardening} \Rightarrow \sigma_i^c = \sigma_y^c; \bar{K}_i^c = \bar{K}_1^c \text{ and } \bar{\zeta}_i = \bar{\zeta}_1 \\
 \text{if } i = 2 &:\text{softening} \Rightarrow \sigma_i^c = \sigma_u^c; \bar{K}_i^c = \bar{K}_2^c \text{ and } \bar{\zeta}_i = \bar{\zeta}_2 \\
 \text{if } i = 3 &:\text{rupture} \Rightarrow \sigma_i^c = 0; \bar{K}_i^c = 0 \text{ and } \bar{\zeta}_i = \bar{\zeta}_3
 \end{aligned} \tag{1.29}$$

The compression and the tension phase of concrete response do not have the same number of yield functions, this is not the case for reinforcement constitutive model, where two yield functions are used for both compression and tension, with hardening and softening part.

$$\begin{aligned}
 \Phi^t(\sigma, \bar{\zeta}_i) &:= |\sigma| - (\sigma_i^t + \bar{K}_i^t \bar{\zeta}_i) \leq 0 \\
 \text{if } i = 1 &:\text{softening} \Rightarrow \sigma_i^t = \sigma_y^t; \bar{K}_i^t = \bar{K}_1^t \text{ and } \bar{\zeta}_i = \bar{\zeta}_1 \\
 \text{if } i = 2 &:\text{rupture} \Rightarrow \sigma_i^t = 0; \bar{K}_i^t = 0 \text{ and } \bar{\zeta}_i = \bar{\zeta}_2
 \end{aligned} \tag{1.30}$$

The main applications we are targeting by this model concern the ultimate load computation under a quasi-static monotonically increasing loading, so that the effect of damage induced change of elastic properties of the concrete is not considered fortunate {we refer to Ibrahimbegovic, Jehel and Davenne [2008] for the model that can combine plasticity with damage model and thus represent all mechanisms}. Under flexural loading, some fibers close to the mean line of the cross section may change the stress state from the compression with a activated compression damage limit to tension were new damage will get activated. In order to accommodate those mechanical phenomena, we can present the general equation of deformation including the particular strain discontinuity in each phase, which allows to combine damage in compression with damage in tension.

$$\epsilon_{x,t}^i = \sum_{a=1}^2 B_a d_{a,t} + \bar{G}(\alpha^{i,c} + \alpha^{i,t}) \quad (1.31)$$

In (1.31), the value $\alpha^{i,c}$ always remains negative, but the value $\alpha^{i,t}$ is positive independent time. When the tension state in the fiber is active, $\alpha^{i,t}$ changes, but the compression state or the value of $\alpha^{i,c}$ is kept constant. The reversal process is done when the compression state in the fiber is active with $\alpha^{i,c}$ changing and $\alpha^{i,t}$ kept constant.

The second material model is used for reinforcement steel. The constitutive laws of steel in this paper is different from that of concrete. Each of the compression and tension phases are described by the same threshold functions. The hardening/softening variables $\bar{\zeta}_i$, the trial stress σ and hardening/softening parameters are used with the same values for both phases leading to:

$$\begin{aligned} \Phi(\sigma, \bar{\zeta}_i) &:= |\sigma| - (\sigma_i + K_i \bar{\zeta}_i) \leq 0 \\ \text{with } i = 1 &: \text{hardening phase} \Rightarrow \sigma_i = \sigma_y \text{ and } K_i = K_1 \\ \text{with } i = 2 &: \text{softening phase} \Rightarrow \sigma_i = \sigma_u \text{ and } K_i = K_2 \\ \text{with } i = 3 &: \text{rupture phase} \Rightarrow \sigma_i = 0 \text{ and } K_i = 0 \end{aligned} \quad (1.32)$$

Typical values of material parameters for both concrete and steel fibers used in computations are defined in the next section, dealing with numerical examples.

4 Numerical examples

In this section, we describe the results obtained in two numerical examples: the first considering the three point bending test of a simple beam and the second dealing with the limit load analysis of two-storey frame. The geometric and material properties of both concrete and steel of the simple beam and frame are taken from [3] and [4].

4.1 Reinforced concrete simple beam

The beam used for test is of rectangular cross-section $b \times d = 20 \times 50\text{cm}$ and the length $L = 5\text{m}$. Two reinforcement longitudinal bars of diameter $\phi = 8\text{mm}$ are placed at the top side, and two with diameter $\phi = 32\text{mm}$ are placed at the bottom side of the cross section. The concrete material parameters used in this example are the same as those in [3], (see Fig.3.4). Young’s modulus $E_b = 37272\text{MPa}$, fracture process zone threshold $f'_y = 30.6\text{MPa}$, compressive strength $f'_c = 38.3\text{MPa}$, tensile strength $f_{ct} = 3.727\text{MPa}$, hardening modulus in compression $K_1 = 9090\text{MPa}$, softening modulus in compression $K_2 = -18165\text{MPa}$ and softening modulus in tension $K_3 = -30000\text{MPa}$.

The steel reinforcement material parameters chosen for this computation are: Young’s modulus $E_s = 200000\text{MPa}$, yield stress $f_{ys} = 400\text{MPa}$ and $t = E_t/E_s = 0.0164$. The stirrups with the diameter $\phi = 8\text{mm}$ and the distance $a = 100\text{mm}$ are placed along the beam. Detailed plan of the reinforcement is presented in Fig.1.9

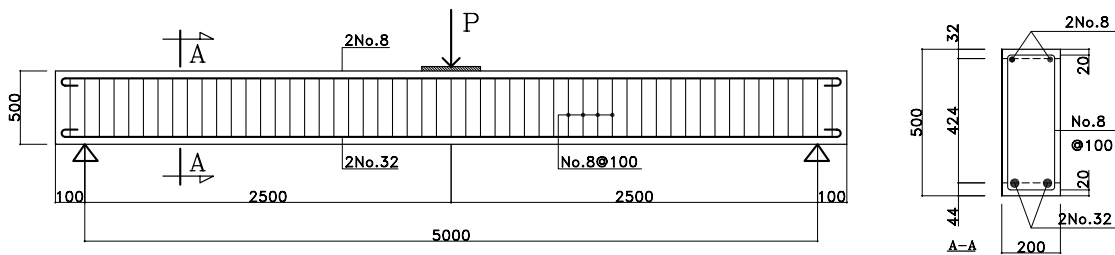


Figure 1.9: Reinforced concrete beam in computation

In the experiment, the beam is loaded by the vertical force P applied at the middle of the beam, with the load increasing from zero to the ultimate value. However, in actual computations, we would also like to represent the post-peak response of the beam under ultimate load. Therefore, we choose a model for half of the beam (see Fig.1.10) and carry out the analysis under displacement control.

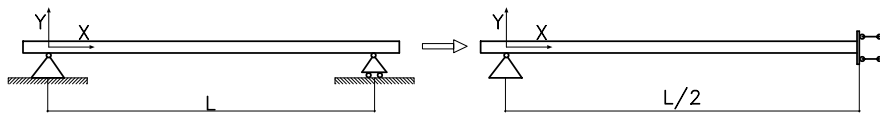


Figure 1.10: Beam diagram in computation

More precisely, we impose the increments of vertical displacement, along with the zero value of the rotation of the middle of the beam. With the length of the beam $L = 5\text{m}$

divided into 16 elements length is $L_e = 0.3125m$ for each element. The relation between vertical force and vertical displacement is established and compared for three computational models: 1- Multi-fibers, 2- Macro element, and 3- the result from Code-Aster.

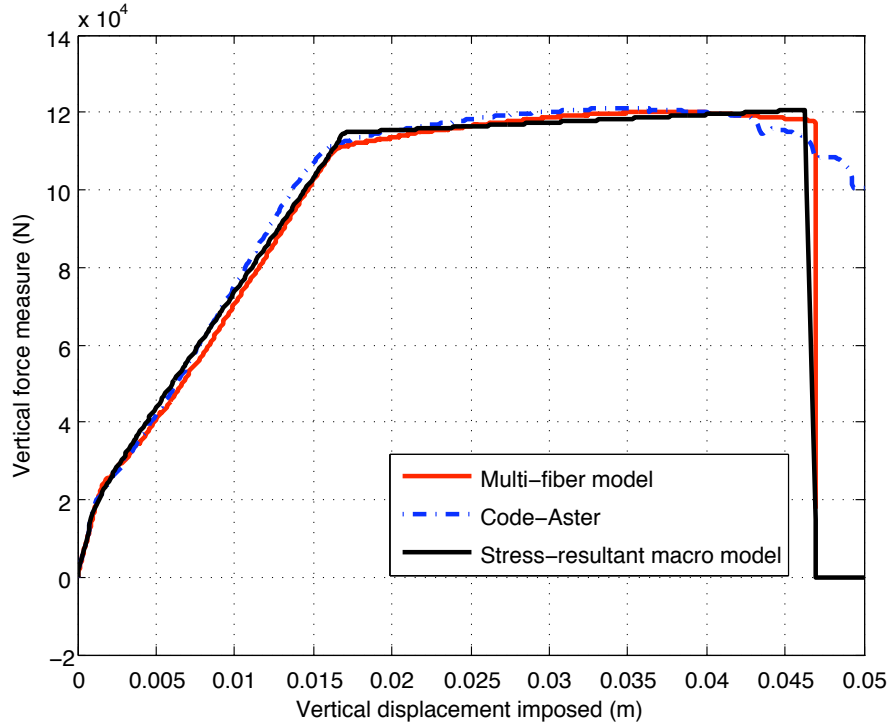


Figure 1.11: Relation of reaction and vertical displacement

In the first computation, the multi-fibers model divides the cross-section of the beam into 20 layers of concrete, and 4 discrete fibers of steel placed at the exact position of steel bar. The relation for force/displacement computed by the stress resultant model is presented as the thin solid line. The result of the Code-Aster computation with another fiber model [4] is also re-introduced as the dash-dot line.

In order to obtain the moment-curvature relationship that will be used for the stress resultant macro element computation, a representative beam element is chosen in terms of a console (see Fig.1.13), such an element has the length, the cross-section and material properties the same as all of the multi-fibers beam with the length $L_e = 0.3125m$, the cross-section $b \times d = 20 \times 50cm$, and 2 steel bars $\phi 8mm$ at the top, and 2 bars $\phi 32mm$ at the bottom side of the cross section. In this representative beam element, there is no effect of the axial force, so it is only the imposed rotation that is used to define the moment-curvature response. From the computed moment-curvature diagram for the representative beam element, we can easily define the corresponding moment threshold to be

employed for macro model computation. In this case it is easy to determinate the cracking moment value $M_c = 37.9KNm$ with the tangent value $K_1 = 29400MPa$, the yield moment value $M_y = 268KNm$ with the tangent value $K_2 = 172MPa$ and the ultimate moment value $M_u = 282KNm$ with the tangent value of softening phase $K_3 = -40800MPa$. Those values are further applied to the macro element, used for the computation of the vertical force-displacement diagram for the original reinforced-concrete beam. Those computations are carried out by computer code FEAP (see [14]) and the results are presented by thick solid line in Fig.1.11.

We note that the vertical force-displacement relationship for both multi-fiber or macro element can be solved up to the complete rupture point, while in the Code-Aster the computation can only reach the ultimate value. This is due to the enhanced kinematics and embedded discontinuity for representing the post-peak response by either multi-fiber or stress resultant macro beam element. Moreover, the macro element with embedded rotational discontinuity permits the problem to be solved with lower cost and quite comparable quality of the global result, which indicates its potentially great value for design procedure.

4.2 Two-storey frame ultimate load computation

In the second numerical example, we consider a reinforced-concrete frame with two floors and one span. The dimensions of the frame are detailed in the fig.1.12. The cross-section of both column and beam is $b \times d = 30 \times 40(cm)$, . In both beam and column, $4\phi 20mm$ of the longitudinal bar are placed at each side, and the stirrups $\phi 10mm$ at the distance $a = 125mm$ are used along to the length of span and the height of two-storey. This example is based on the experiment presented in [3]. Two fixed vertical forces $P = 700KN$ are applied at two nodes on the top of the frame representing the effect of the dead load. The lateral force is imposed on one side at the top node with the values increasing from zero to the time of the complete collapse of the frame.

The finite element model used in the numerical computations is as follows: each column with the height $h = 2m$ is divided into 8 elements with $L_e = 0.25m$ and each beam with the length $L = 3.5m$ is divided into 14 elements with $L_e = 0.25m$. The concrete has compressive strength $f'_c = 30MPa$, tensile strength $f_{ct} = 1.8MPa$, modulus of elasticity $E_b = 28,600MPa$. All the details on material parameters and geometry for the test can be found in [3].

For obtaining the transversal force-displacement diagram by the multi-fiber model computation, the cross-section is divided into 20 layers of concrete. In the cross-section are embedded 8 fibers of reinforcement steel, 4 on each side. The dimensions of cross section can be seen in Fig.1.12. The result of this computation is obtained by FEAP program, and the relation of lateral load versus deflection at the top storey of frame can be described by the hidden line in the Fig.1.16 and be compared to the dash-dot line of the

result of experiment.

In the computation using the stress resultant macro model, we also use two small secondary computations on the console very much the same as in the first example, except for the cross-section $b \times d = 30 \times 40(\text{cm})$ and the length of element $L_e = 0.25\text{m}$ for the frame case (see Fig.1.13). The first computation is carried out to find the relation of moment-curvature of the beam macro elements, when only moment with no axial force is applied, $M \neq 0$ and $N = 0$. The second computation is performed to obtain the relation of moment-curvature of the column macro element, where there are combined effects of moment and of axial force, $M \neq 0$ and $N \neq 0$. In this particular case, the column is first loaded by a constant axial force $N = 700\text{KN}$ followed by imposed moment. The results for moment-curvature relationship is given in Fig.1.14 for both cases.

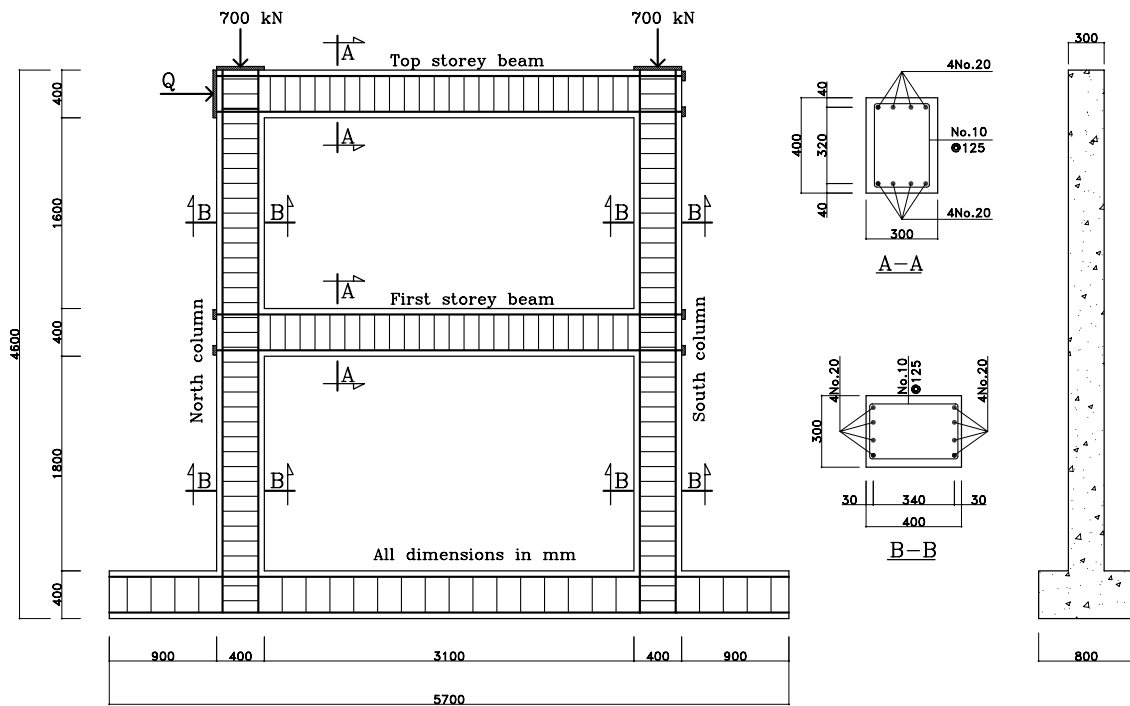


Figure 1.12: RC frame diagram in computation and experiment

The values of crack moment, yield moment and ultimate moment correspond to the values of flexions at the points of crack, yield and ultimate. We can apply all to the macro model to compute the macro frame. There are two kinds of section applied, one for the beam and one for the column. With the fixed value of the axial force $N = 700\text{KN}$ in the column computation, despite that both column and beam have the same section, we obtain all of the limit values of moment in the column much higher than those in the beam.

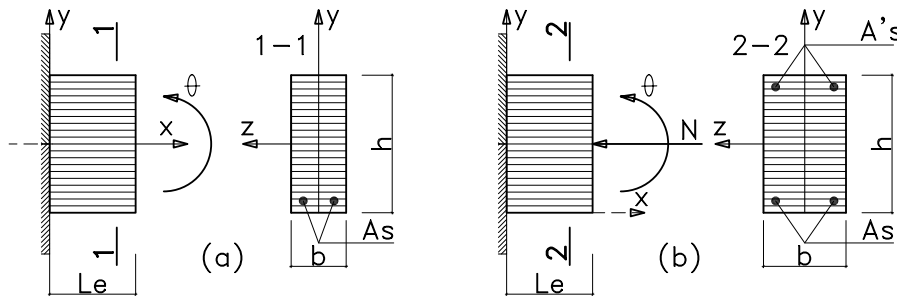


Figure 1.13: Elements to compute beam and column

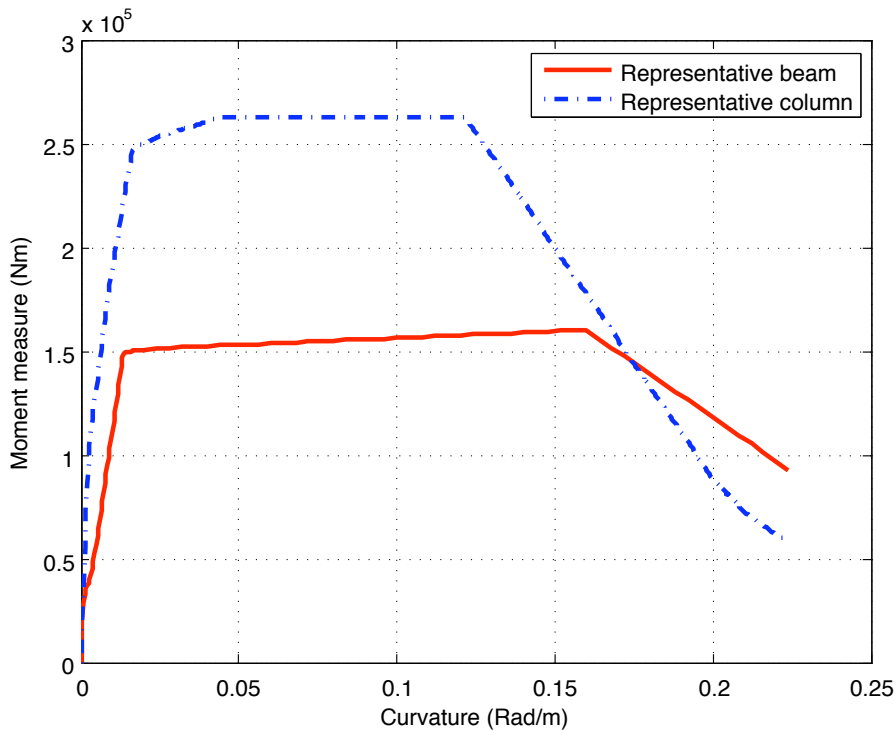


Figure 1.14: Relation of moment-curvature for representative beam and column

All the results for the frame computation for two cases obtained with multi-fiber and macro models, are computed by FEAP program (see [14]). In Fig.1.15, relation of transverse force and rotational displacement is presented. By the time steps, the plastic hinge group appears following in order in this case that the first plastic hinges appear in the elements number 1 and 17, where exist the axial force and the highest bending moment; the second plastic hinge group appears at two ends of the first beam of frame, elements number 33 and 46, where exist just only the bending moment; and the third group appears at two ends of the top beam of frame, the elements number 47 and 60.

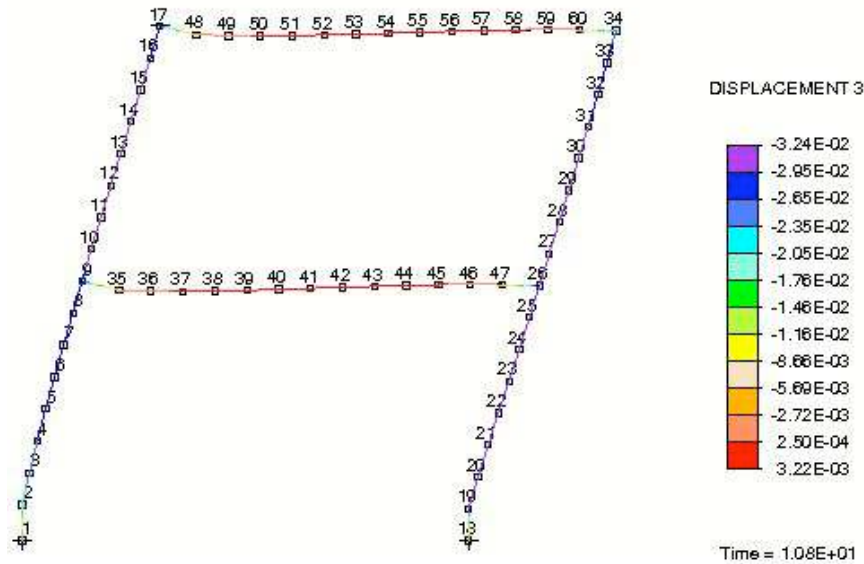


Figure 1.15: Rotational displacement of frame

The relation of lateral load-displacement of the macro computation is expressed also in Fig.1.16 with the continuous line to compare to the cases of experiment and multi-fibers. In fact, while the lateral load is increasing, the values of axial force in each columns are changed. The axial force of two columns on the left of frame will be decreased by the appearance of traction forces, while the axial force of two remaining columns on the right of frame will be increased by the appearance of compression forces. Further more, in the multi-fiber model computation, the change of axial force in the element is counted to affect to the change of bending moment, because of the change of stress in the fibers. The value of bending moment in this case is computed from the integral the stress in all fibers multiplied with the distance of fiber to neutral line. In the macro model, the axial force in the columns is also changed following the change of lateral load, but the relation of moment-curvature does not change, so there remain a difference in the comparison between multi-fiber model and macro model.

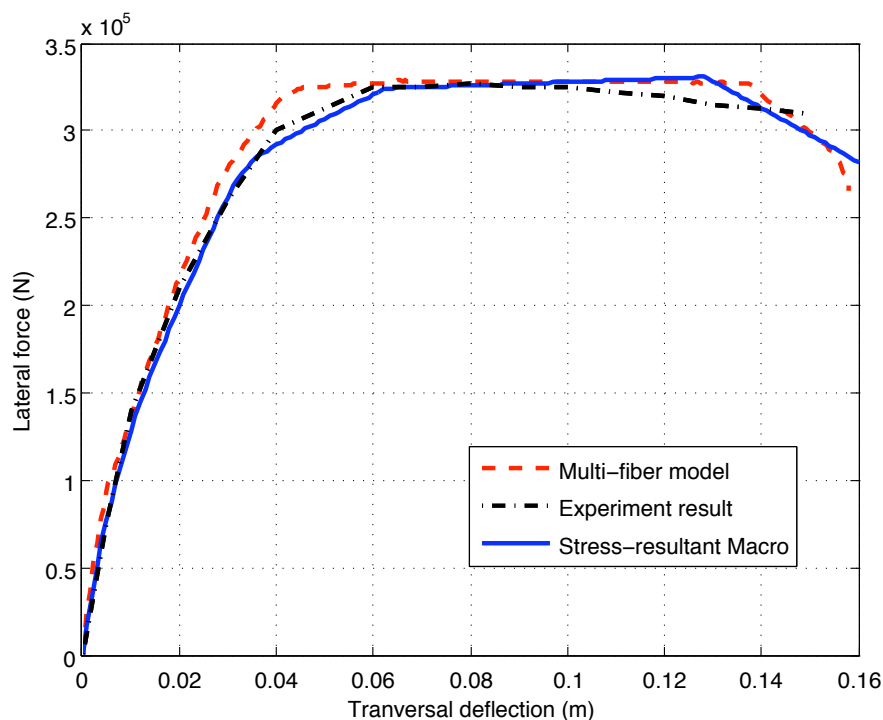


Figure 1.16: Relation of lateral load versus deflection at top storey of frame

5 Conclusions

In this work we have developed the stress-resultant (macro) beam element suitable for the ultimate limit state computation of reinforced-concrete frames. The parameters of such a model can be given very classical interpretation, such as the first cracking moment, the yield moment and the ultimate moment, which all affected both by concrete and reinforcement. The model assumes different hardening regimes until the ultimate moment is reached and a subsequent softening regime.

The latter leads to localization phenomena, or a plastic hinge creation that leads eventually to reducing the bending moment to zero once the corresponding fracture energy is applied. The plastic hinge requires a special finite element implementation where the standard Timoshenko beam element has to be enriched by the corresponding rotational discontinuity. This provides the most reliable representation of the failure mechanism independent on the chosen Timoshenko beam length.

We also present a multi-fiber (micro) beam model, where the beam cross-section can be split into a number of either concrete or steel reinforcement fibers. Each fiber is then assigned the corresponding constitutive model, which allows to obtain the adequate value of stress for the strain defined in accordance with the Timoshenko beam kinematics and

the position of a particular fiber with respect to the neutral axis of the Timoshenko beam. The concrete fibers are assigned different laws in tension and compression, characterized by the standard concrete parameters, such as: f_t — concrete tensile strength, f_c — concrete compressive strength and f_{cy} — concrete micro-cracking and fracture process zone creation.

The steel parameters are also quite standard, such as the yield stress σ_y and the ultimate stress σ_u . It was shown that the present multi-fiber model can provide quite reliable interpretation of the corresponding parameters for stress-resultant model. These two models can thus be used interchangeably in order to provide the most suitable and the most efficient computational procedure for the ultimate limit state of reinforced concrete frames, which could eventually lead to more reliable design procedures for this kind of structures.

Chapter 2

Stress resultant and multi-fiber beam model for combined axial force and moment

In this paper, we present the combined axial force and bending moment ultimate load computation, which continues the developments in the first part dealing with beam bending failure. We first review the pertinent formulations and assumptions in Euro Code 2 (EC2) used for predicting the relation between axial force and ultimate moment in the rectangular cross section of reinforced concrete column. As a more reliable alternative, the more realistic properties in material constituents of concrete and reinforcement were considered and applied in this along with the multi-fiber section mode. The modified stress-resultant beam macro model based on Timoshenko beam theory in the first part could also express the appearance and behavior of plastic hinges or mechanic failure in reinforced concrete frame, in the presence of axial force. In order to obtain a better and more flexible stress-resultant macro model, which can compute the column element with both the changes of moment and axial force. Beside rotational discontinuity embedded for describing the mechanical failure in frames, some functions expressing moment-axial force relation are needed for the model. The modified multi-fiber model introduced in the first part was used to compute and identify the new model parameters, by which we could create the moment and axial force relation. Several numerical examples are presented in order to illustrate the main differences between the new model compared to the previous model for beam bending failure and also the new model capabilities for dealing with the beam-column failure problem successfully.

Contents

1	Introduction	31
2	Prediction for the relations of ultimate and yield moments with axial force	32
2.1	Material properties and basic assumptions	33
2.2	Formulas for doubly reinforced-concrete rectangular section	34
2.3	Prediction for ultimate moment and axial force relation	36
3	Parameter identifications and macro model for stress-resultant failure criteria in frame	38
3.1	Stress-resultant macro model for reinforced concrete frames and chosen material behavior of concrete and reinforcement	38
3.2	Parameter identification for doubly reinforced concrete rectangular section	41
3.3	Function identification for moment-axial force relation	48
3.4	Function identification for curvature-axial force relations	51
3.5	Moment and curvature yield functions for stress-resultant macro model at the time t	55
4	Numerical applications	56
4.1	Single-element console computation	57
4.2	Two-storey reinforced concrete frame computation	59
5	Conclusion	66

1 Introduction

The effects of plastic hinges in reinforced concrete frame structure and the results of computation including the embedded rotational discontinuity (discussed in the first part) have also been studied by many researches (see [4], [5], [10], [11]). With the beam model with plastic hinges in design computation, we can obtain more reliable models both in design of a structure and in the verification of integrity of an existing structure. Furthermore, the computational work after the ultimate loading value is more concerned recently, that will give us the clear knowledge about the frame structure, from that we can give out a decision and method for maintaining the building.

In the first part, we already presented a macro model of stress-resultant for Timoshenko beam-column element. That model can be used to compute the beam-column with rotational discontinuity embedded in the middle of beam element. The axial load on element does not change while the threshold functions computed to find bending moment are kept constant in each iterations. That was the first step to develop the stress-resultant beam macro element, which was suitable for computing a single column component. However, in the complex frame structure with many beam and column elements this approach is not much suitable for reliable computations. Otherwise, in frame structure with the affection of the transverse load, the axial force in the column elements will be changed that will re-affect against the change of limit values of moments in threshold functions. Therefore, we shall consider a new modified stress-resultant macro model accounting for combined section of bending moment and axial force. This new model has the capability to compute the beam-column elements with the embedded rotational discontinuity and to provide a reliable representation of the frame under and after the ultimate load. This especially the case, when both bending moment and axial load are changed following the change of external load.

Many recent research works are concerned by the problem of computation with plastic hinges appearance in the reinforced-concrete frame structures. We refer to some recent papers [4], [5], [11], [16]. Some of those papers consider the problem with the combination of fracture-mechanic, damage-mechanic and the concepts of plastic-hinge. Others consider the plastic softening behavior under bending and axial forces using a relation of moment and axial forces with the simple yield functions obtained for the symmetric-homogenous material.

In this work, the modified multi-fiber model for reinforced concrete is used. With this model, we can compute and identify all the limit values of bending moment, such as crack-moment, yield-moment and ultimate moment (M_c , M_y , M_u), under different values of axial force from zero to the ultimate axial load without bending moment ($N_{max} = N_u$, $M = 0$). In those multi-fiber computations, concrete and steel material are used as Elastic-Plastic-Softening model, that is also presented in the first part.

It is very important to recognize that many factors affect the behavior of moment-curvature in the reinforced concrete columns. We can mention some of them as: shape and dimension of cross-section, steel reinforcement ratio, material properties of both concrete and steel, kind of loading, position of reinforcement as well as the reinforcement arrangement. For this work, we use some limitations in concrete and steel materials following EC2 (see [18] and [19]). The cross-section of column is rectangular, in which two longitudinal steel reinforcement layers are embedded at the symmetric positions of two sides of cross section. All external loads used to compute stress-resultant properties and carrying out numerical applications are quasi-static loads.

In Section 2, we introduce some limitations in material properties of concrete and steel, with the basic assumptions used for the beam-column computation. Some equilibrium formulations of moment and axial force for cross section design are also presented. All of them are taken from EC2, these formulations need to predict the formulas, also the charts for moment and axial force relations. In Section 3, we present the problem of identifying parameters, which needs to be solved in particular for stress-resultant macro model such as moments for threshold functions, (M_c, M_y, M_u) and tangent moduli for the phases of hardening and softening (K_1, K_2, K_3) . We also present the functions expressing the relation of both couples moment-axial force and curvature-axial force. The behaviors of concrete and steel are also introduced in the beginning of the section. In the last section, we introduce the new stress-resultant macro model for frame computation with new threshold functions, in which moment functions and modulus functions are considered to express the coupled moment and axial force action.

In Section 4, we present several illustrative examples for numerical applications. The first example is the one with a built-in beam, which has just one element. This example is employed for testing the behavior at local level, where both rotation and axial load are imposed and changed at the free end for purpose to obtain the corresponding changes of both moment and axial force. In the second example, we represent the two-storey reinforced concrete frame, which aims to obtain a comparison between computational results of both stress-resultant macro model in the first and this parts. Those results are also compared with the results in multi-fiber computation or in the practical experiment. In the last section, some concluding remarks and perspectives are given.

2 Prediction for the relations of ultimate and yield moments with axial force

In this section we first review the basic assumptions for design computation in reinforced-concrete frame components, some limitations of concrete and steel materials proposed EC2 as introduced in [18] and [19]. With these formulations in hand, we can easily predict the figure of yield and ultimate moments with respect to the axial force in rectangular cross section submitted to the axial force and bending moment.

2.1 Material properties and basic assumptions

We can have many kinds of simplified material constitutive models for both steel reinforcement and concrete as suggested by EC2, and the other using codes. Hence, in this work, it is first necessary to give some guidelines and conditions for material used herein. Generally, we use some basic assumptions in the design computation for beam or column: one is that plane sections remain plane once loaded, and the strain in reinforcement is the same as the strain in the concrete at the same level (no bond slip). These assumptions are universally accepted for the design of members containing bonded ordinary reinforcement. With perfect bond, the change in strain in the steel is assumed to be the same as the change in strain in the concrete.

In computation of the resistance for a reinforced-concrete column, many factors in material properties of both steel and concrete affect to the load carrying capacity of elements. However, in a simplified version for the consideration to follow, we just concentrate on main factors, such as the yield and ultimate strengths, strain limits and moduli. At first we introduce steel material model proposed in EC2. Absolute limit is not given for the maximum tensile strain in the reinforcement, but there is clearly a limiting strain that defines the failure of any particular type of reinforcement. In Figure.2.1 we introduce the stress-strain diagram in steel material used for design, where the curve *B* is expressed for design while the curve *A* is considered as the idealized curve. Strain limit ϵ_u for normal ductility steel is equal to 0.025 and for high ductility steel it is equal to 0.05. More discussions and informations about steel material can be found in [18].

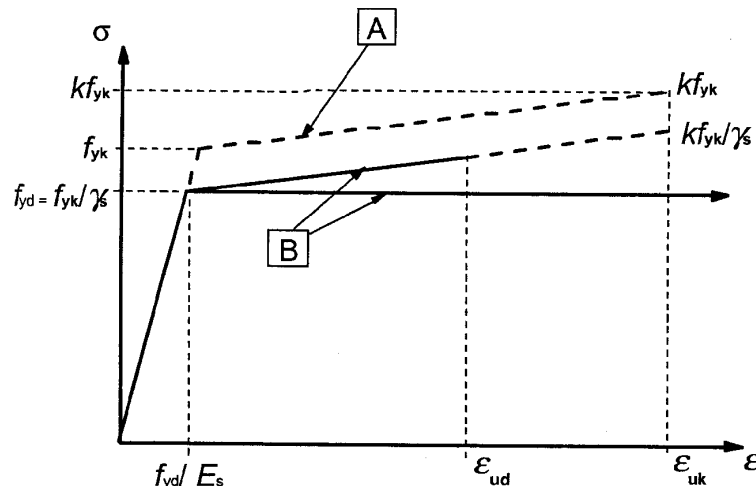


Figure 2.1: Stress-strain curve of steel for design

About concrete material in design for reinforced-concrete, we usually use two main kinds of concrete for construction, the normal and high resistance concrete. In this work

we concentrate on the kind of normal resistance described with the curve in Fig.2.2. The maximum stress in compression is denoted as f_{cm} , as the stress corresponding to one value of strain ϵ_c , while another ultimate strain ϵ_{cu1} is considered as the nominal value.

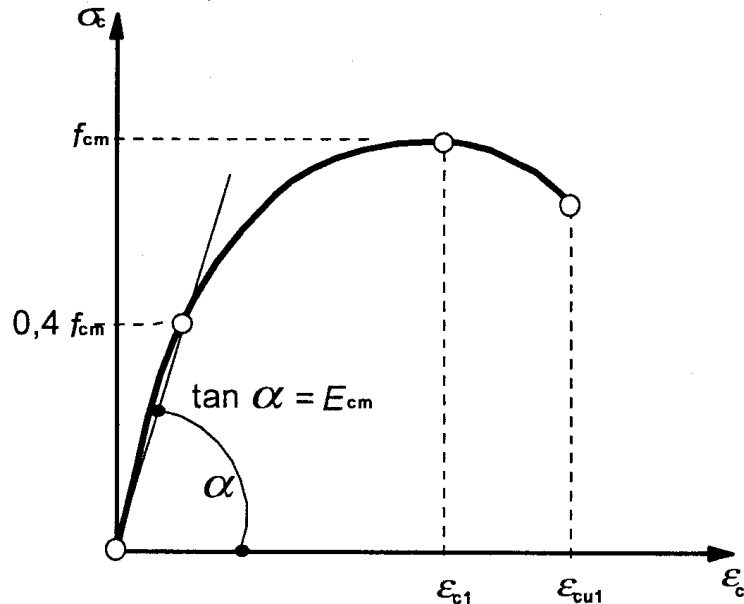


Figure 2.2: Stress-strain curve of concrete in compression of experiment

The ultimate strain in concrete is different in different codes. Following EC2 (see [18]), we use ultimate strain ϵ_u equal to 0.0035, for the case of coupled bending moment and axial force and under the condition that the neutral axis remains within the cross-section. For an alternative case, with the complete cross-section under compressive stress, the ultimate strain ϵ_u is changed from 0.002 to 0.0035 (see Fig.2.3).

There are several hypotheses for stress-strain diagram of concrete in compression zone, which are used in design computation, such as the hypotheses parabolic-rectangular, bilinear or rectangular curves. We consider the first of these diagram with the parabolic-rectangular shape (see Fig.2.4), in which the stress curve in compression zone of cross section in pure-bending or under combined action of the bending moment and axial force.

2.2 Formulas for doubly reinforced-concrete rectangular section

The formulas considering the ultimate bending moment and axial force of the rectangular cross section in the reinforced concrete column, used for the situations where the neutral axis remains within sections, are given as follows.

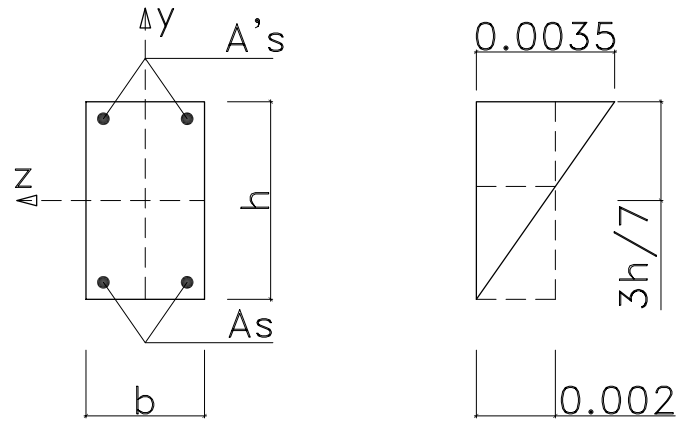


Figure 2.3: Ultimate strains in members under compression

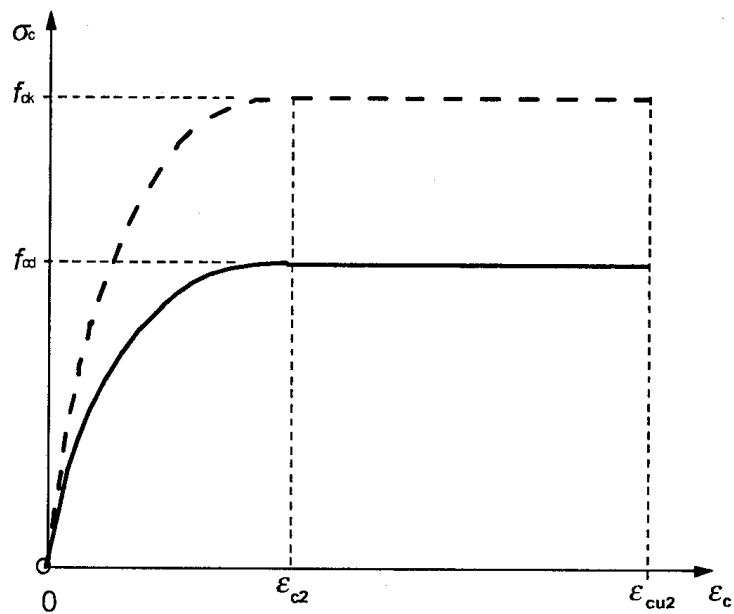


Figure 2.4: Parabolic-rectangular curve in compressive zone of bending beam

$$N_{Rd} = f_{av}bx + \sum f_s A_s \quad (2.1)$$

$$M_{Rd} = f_{av}bx\left(\frac{h}{2} - \beta x\right) + \sum f_s A_s \left(\frac{h}{2} - d_i\right) \quad (2.2)$$

where N_{Rd} and M_{Rd} denote, respectively, axial force and ultimate bending moment capacities of the rectangular cross section. The dimensions $b \times h$ denote the width and the height of the cross section, whereas x is the depth of compression zone and β is considered as the ratio of distance from the position of the sum of force in compressive zone of concrete to the most compressive edge of rectangular section with respect to the depth of compressive zone x . Normally, in design computation, the value β is chosen as 0.416. The tensile strength of concrete in these formulas is ignored, while compressive strength f_{av} is used as the average stress in the compressive zone. Comparing to the value of maximum compressive strength f_{ck} , f_{av} is equal to 0.459 of f_{ck} . Yield strength value used in design of steel, denoted as f_{yd} , is equal to $f_{yk}/1.15$, where f_{yk} is the yield tensile strength for steel. Distances from each layers of reinforcement to the centre of the cross-section is denoted as d_i .

With these design formulas on hand, we can obtain the result for reinforcement area A_s , which will be placed at the design positions in the cross-section in order to carry moment and axial force. In cross section design, for each couple of (M, N) we can find the corresponding reinforcement area A_s .

2.3 Prediction for ultimate moment and axial force relation

From two formulas in (2.1) and (2.2), we can readily obtain the corresponding relationship between the ultimate moment and axial force (see Fig.2.5). There are two cases related to load compression for a particular rectangular cross-section. The first case is called the large-eccentricity load, where in the couple of (M, N) , the value of M is very big compared to the value of N , so that we obtain a large value $e = M/N$. In this case, in comparison to the limit-eccentricity e_{limit} of the section, we shall have $e \geq e_{limit}$. This limit-eccentricity is considered as the frontier between large-eccentricity and small-eccentricity (see [18]). In case of the large-eccentricity, cross-section is divided clearly into two parts with compression and traction zone, with the neutral axis that always remains within the section. The failure process in the cross-section will derive from the yielding process of steel in the traction zone. We use an increasing relation of ultimate moment and axial force in the case of large-eccentricity, which means when axial force increases we shall also obtain a increasing ultimate moment.

In the second case, we consider the small-eccentricity, where the eccentric value $e = M/N$ is smaller than the limit-eccentricity e_{limit} . The failure process will derive mostly from the failure process of concrete in compressive zone. We shall obtain a descending

relation of ultimate moment and axial force. This further implies that in case of small-eccentricity, the axial force increase will also be accompanied by a descending values of ultimate moment.

We propose these relations as shown in Fig.2.5, as the functions of yield and ultimate moments with respect to the axial force. For either of those relations, we note three particular points: the first point is when axial force is equal to zero; the second point is when the value of ultimate moment of the section reaches maximum value M_{max} , corresponding to axial force N^* ; the third point is when axial force reaches the ultimate value, that corresponds to the moment be equal to zero $M = 0$. For each rectangular cross-sections of reinforced concrete column, and each value of axial force N , we can thus easily determine the correspondence of yield and ultimate moment (M_y and M_u).

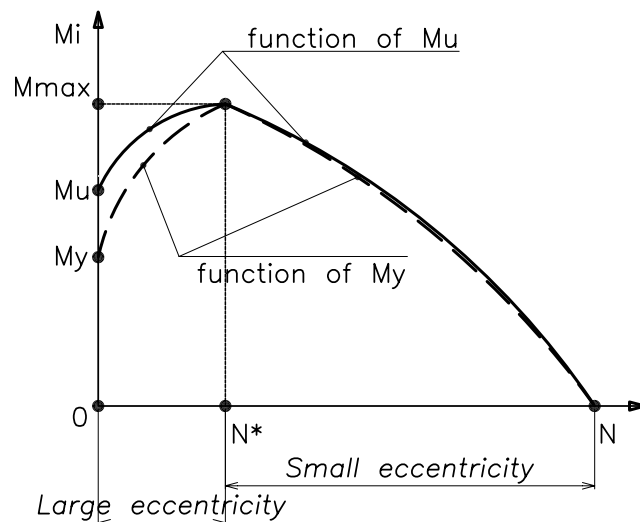


Figure 2.5: Prediction for ultimate moment-axial force relation

In order to define the proper relationship each couple (M_u, N) or (M_y, N) , we first compute three points $(N = 0., M \neq 0.)$, $(N = N^*, M = M_{max})$, and $(N = N_u, M = 0.)$. These are three points separating the curve into two separate functions: one for large-eccentricity and the other for small-eccentricity case. These points can easily be determined not only by numerical but also by analytic computations. In the next section we present the identification procedure for identifying these parameters and defining the complete functioned relationship.

3 Parameter identifications and macro model for stress-resultant failure criteria in frame

In this section, we elaborate upon the tasks of identifying the limit values of moment (M_c , M_y , M_u) and hardening/softening moduli (K_1 , K_2 , K_3) for stress-resultant macro model. We also deal with the tasks of creating the functions of moment-axial force and/or curvature-axial force relations. The relations identified in this manner are embedded into threshold functions for combined action of bending moments and axial force, which can be used for computing the complete failure of a reinforced concrete beam-column element with the rectangular cross-section. We present in Fig.2.6 the multi-fiber beam used for such an identification procedure. The computation is carried out under free-end rotation and axial load, which is also indicated in Fig.2.6.

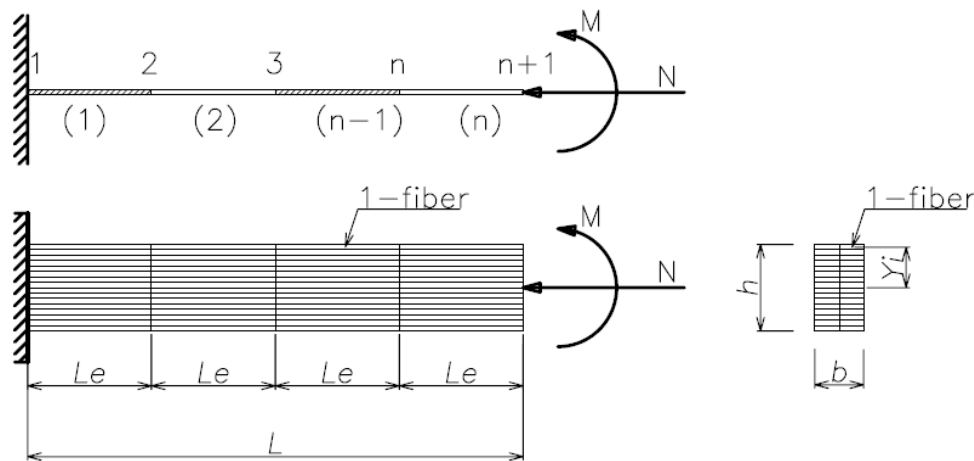


Figure 2.6: Imposed axial load and rotation in multi-fiber and stress-resultant beam-column element

3.1 Stress-resultant macro model for reinforced concrete frames and chosen material behavior of concrete and reinforcement

We present the macro model of stress-resultant for reinforced-concrete beam computed in accordance with the chosen constitutive behavior of the main ingredients, concrete and steel. In this model three prominent values of moments included the first cracking, the yield and the ultimate moment (M_c , M_y , M_u).

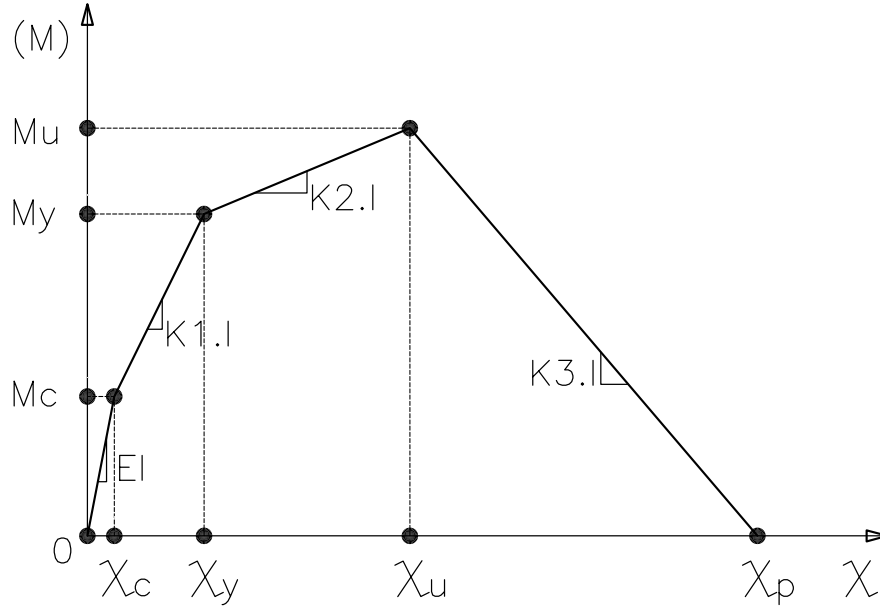


Figure 2.7: Stress-resultant macro model for frames

Three threshold functions are defined for this model featuring these prominent values of moments, which can be written as:

$$\Phi^M(M, \zeta_i^M) := |M| - (M_i + K_i I \cdot \zeta_i^M) \leq 0$$

if $i = 1$:hardening phase 1 $\Rightarrow M_i = M_c$; $K_i = K_1$ and $\zeta_i^M = \zeta_1^M$

if $i = 2$:hardening phase 2 $\Rightarrow M_i = M_y$; $K_i = K_2$ and $\zeta_i^M = \zeta_2^M$

if $i = 3$:softening phase $\Rightarrow M_i = M_u$; $K_i = K_3$ and $\zeta_i^M = \zeta_3^M$

if $i = 4$:complete rupture $\Rightarrow M_i = 0$; $K_i = 0$ and $\zeta_i^M = \zeta_4^M$

where K_1 , K_2 and K_3 are the corresponding values of hardening/softening moduli.

These threshold function are used to describe two different regimes for stress-resultant models: a stress-resultant elasto-plastic model with two linear hardening phases, dealing with different mechanisms of inelastic bulk behavior; and a rigid-plastic model with linear softening to deal with the formation and development of a plastic hinge.

We must introduce the Elasto-Plastic hardening-Softening models for concrete and steel, which is defined in detail subsequently, that will be used for identifying the needed parameters for macro model and will provide the basis of the micro-scale model based upon multi-fiber concept.

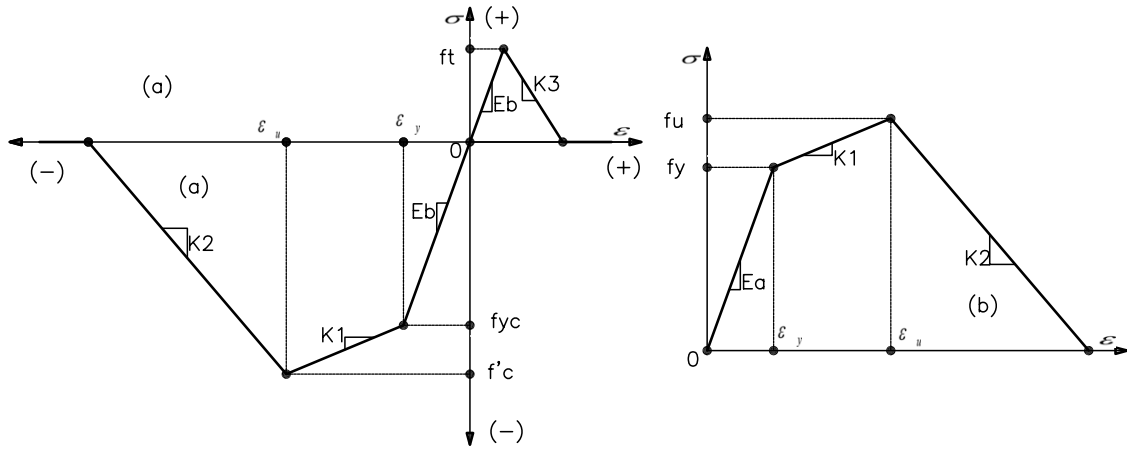


Figure 2.8: Material behaviors of concrete and reinforcement

The concrete material is characterized by constitutive model with two different phases, one for compressive case and another for tension case. The response for each phase is defined with different variables, as well as with the independent yield functions (see Fig.2.8). The parameters needed for this model are tensile fracture stress f_t , compressive stress f_{yc} starting development of fracture process zone and the compressive fracture stress f'_c , as well as the elastic Young's modulus E_b and hardening/softening moduli K_1 , K_2 and K_3 . In the compression phase we account for elastic response followed by the distributed cracking (fracture process zone) softening phase, whereas in tension phase elastic response is immediately followed by softening.

The steel reinforcement is also expressed as combined elasto-plastic hardening and softening. Both compression and tension phase for steel are expressed by the same two yield functions, one for hardening and another for softening regime. The parameters needed for this kind of model concern the yield stress f_y , the ultimate stress f_u , the Young modulus for steel E_b as well as the hardening and softening moduli, K_1 and K_2 .

Yield functions for concrete constitutive model in the compression case can be introduced for both hardening and softening cases:

$$\begin{aligned} \Phi^c(\sigma, \bar{\zeta}_i) &:= |\sigma| - (\sigma_i^c + \bar{K}_i^c \bar{\zeta}_i) \leq 0 \\ \text{if } i = 1 : \text{hardening} &\Rightarrow \sigma_i^c = \sigma_y^c; \bar{K}_i^c = \bar{K}_1^c \text{ and } \bar{\zeta}_i = \bar{\zeta}_1 \\ \text{if } i = 2 : \text{softening} &\Rightarrow \sigma_i^c = \sigma_u^c; \bar{K}_i^c = \bar{K}_2^c \text{ and } \bar{\zeta}_i = \bar{\zeta}_2 \\ \text{if } i = 3 : \text{rupture} &\Rightarrow \sigma_i^c = 0; \bar{K}_i^c = 0 \text{ and } \bar{\zeta}_i = \bar{\zeta}_3 \end{aligned} \quad (2.3)$$

The yield function for the tension case can be defined as:

$$\begin{aligned} \Phi^t(\sigma, \bar{\zeta}_i) &:= |\sigma| - (\sigma_i^t + \bar{K}_i^t \bar{\zeta}_i) \leq 0 \\ \text{if } i = 1 : \text{softening} &\Rightarrow \sigma_i^t = \sigma_y^t; \bar{K}_i^t = \bar{K}_1^t \text{ and } \bar{\zeta}_i = \bar{\zeta}_1 \\ \text{if } i = 2 : \text{rupture} &\Rightarrow \sigma_i^t = 0; \bar{K}_i^t = 0 \text{ and } \bar{\zeta}_i = \bar{\zeta}_2 \end{aligned} \quad (2.4)$$

The yield function for steel constitutive model can be also defined in the same way for both hardening and softening, and we can write as:

$$\begin{aligned} \Phi(\sigma, \bar{\zeta}_i) &:= |\sigma| - (\sigma_i + K_i \bar{\zeta}_i) \leq 0 \\ \text{with } i = 1 : \text{hardening phase} &\Rightarrow \sigma_i = \sigma_y \text{ and } K_i = K_1 \\ \text{with } i = 2 : \text{softening phase} &\Rightarrow \sigma_i = \sigma_u \text{ and } K_i = K_2 \\ \text{with } i = 3 : \text{rupture phase} &\Rightarrow \sigma_i = 0 \text{ and } K_i = 0 \end{aligned} \quad (2.5)$$

Yield functions for both concrete and steel are written unified notation. However, it is clear that, the value of σ_i is equal to the value of ultimate stress f_c' or the plastic stress f_{yc} in the compression regime for concrete, whereas it is equal to ultimate tensile stress f_t in the tension regime for concrete. Similarly, σ_i is equal to the yield stress σ_y or ultimate stress σ_u in both compressive and tension regimes for steel. The values of hardening and softening moduli K_i should also be defined for both concrete and steel materials, and both in compression and tension regime.

3.2 Parameter identification for doubly reinforced concrete rectangular section

Here we will consider the case of rectangular cross-section for reinforced concrete beam-column element. The section dimensions are denoted as $(b \times h)$, with two layers of reinforcements with the areas (A_s', A_s) that are embedded symmetrically in both compressive and tension zone of section. The identification procedure is carried out on the built-in beam. The length of the beam L is equal to the length of single element L_e , that is used for this computation. At free end of the console, we impose an axial load and rotational displacement.

We present a representative for the built-in beam-column, which is used to describe for all needed steps in the process of parameter identification. The dimensions of rectangular cross-section of the beam are $b \times h$ equal to $30 \times 40(\text{cm})$. The length of the beam is as the same as the length of element, for this built-in beam-column we choose $L = L_e$ equal to 0.25m . Inside the cross-section, $4\phi 20\text{mm}$ of the longitudinal bar are placed at each side, and the stirrups $\phi 10\text{mm}$ at the distance $a = 125\text{mm}$ are used along to the length of console. The concrete has compressive strength $f_c' = 30\text{MPa}$, tensile strength $f_{ct} = 1.8\text{MPa}$, modulus of elasticity $E_b = 28,600\text{MPa}$. By using the multi-fiber model for parameter

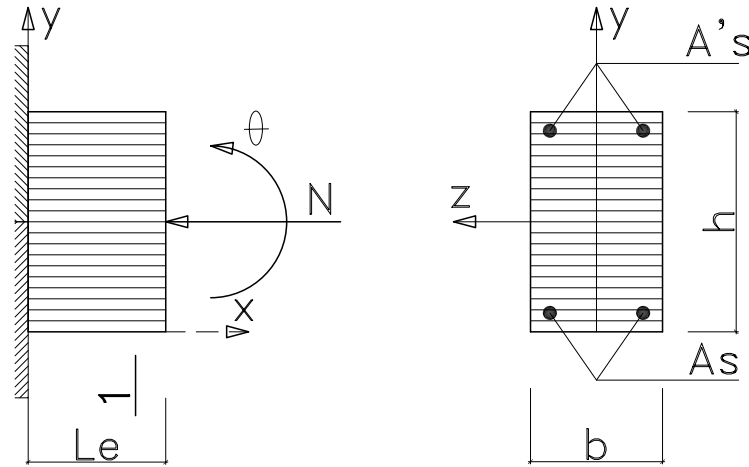


Figure 2.9: Multi-fiber beam-column diagram for parameter identification

identification, we use the divided rectangular cross-section of the beam with 20 concrete layers and 8 discrete fibers for describing the steel reinforcements. The geometry and detail of the beam-column can be seen in Fig.2.10.

In the first step, we compute the limit values of axial force for this beam without the effort of the imposed rotation displacement, which purposes to obtain the third point, N_u , in the relationship of ultimate moment and axial force. By imposing only the axial displacement we can obtain the yield and ultimate axial force (N_y , N_u) as presented in Fig.2.11. Two of these values are the important values, which will be used for the next steps of parameter identification.

By using this built-in beam computation for the case of fixed axial load, with the chosen value of axial load N specified by the ratio $n = N/N_y$, we can consider the steps $n := 0 : 0.1 : 1.05$, and thus obtain the corresponding diagram for moment-curvature for 12 different cases presented in Fig.2.12. We can separate these diagrams into two main groups: the first one for axial force N changes of n from zero to 0.4 of yield axial force N_y and the second for axial force with changes of n from 0.4 to 1.05. The first group corresponds to the large-eccentricity cases, where the failure in the reinforced-concrete beam is induced by the yielding of reinforcement in tension zone. With the increasing values of axial force we can obtain the corresponding increase in values of cracking, yielding and ultimate moment (M_c , M_y , M_u), where the values of M_y and M_u will differ clearly. We also have fairly long part with hardening response diffuse of plastic phase. The second group corresponds to the small-eccentricity case, where the failure process is governed by the compressive failure of concrete in compression zone. With the increase of axial force, we obtain a small difference between the values of yield and ultimate moments, and the value of ultimate moment can even become smaller than the yield moment ($M_u \leq M_y$).

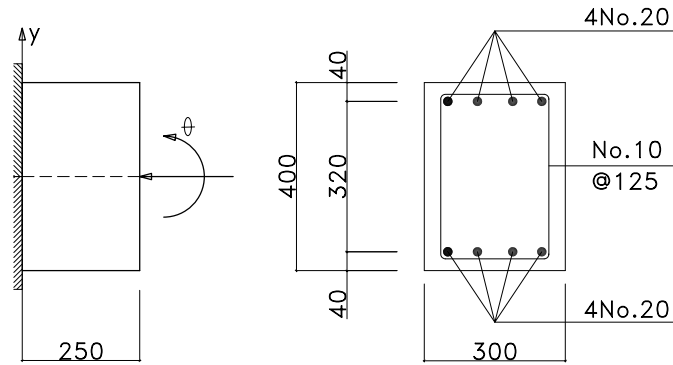


Figure 2.10: Geometry of reinforced concrete built-in beam-column for parameter identification

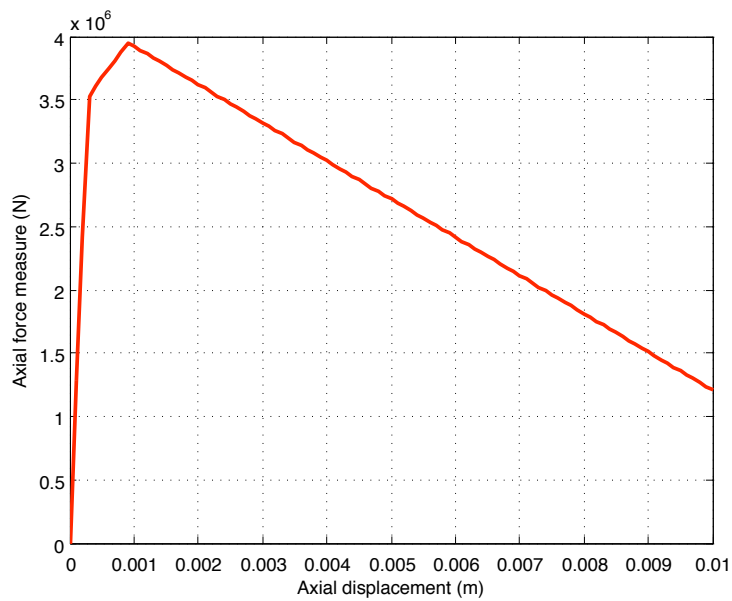


Figure 2.11: Axial force identification for rectangular cross-section

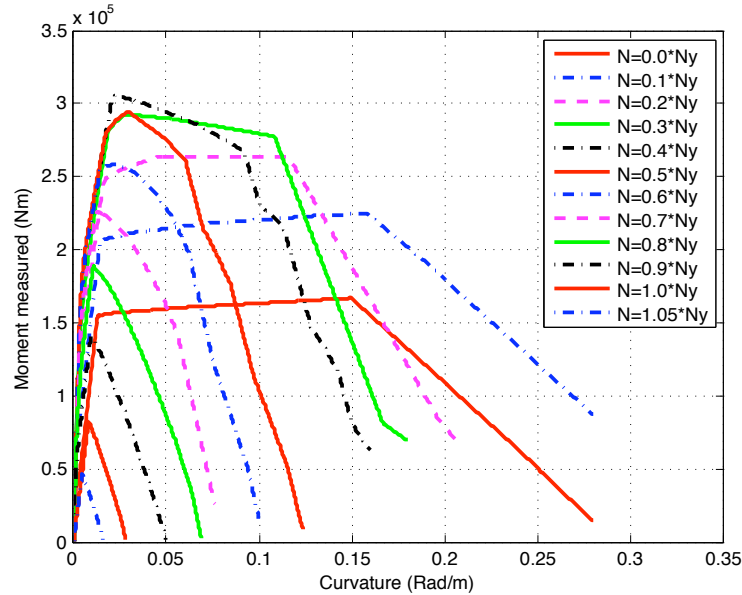


Figure 2.12: Moment-curvature relations obtained by multi-fiber beam-column model based computations

In order to determine the dependence of the prominent values of moments in the reinforced-concrete beam-column element namely, the cracking, yielding, and ultimate moments (M_c , M_y , M_u) and the corresponding curvature values, upon the chosen stress-strain diagrams we present the stress-time curves for several fibers in the cross-section. In this case, four particular fibers are chosen in the cross-section. Two of them are chosen for reinforcements, one in tension zone and the other in compression zone. Two remaining fibers are chosen for concrete, where one is tension fiber and the last one is compressive concrete fiber. Both of concrete fibers are chosen at the top and the bottom edges of cross-section, where the strain values are the largest. For those selected fibers, we can identify easily all limitations for moment following the limit stresses of concrete and steel fibers.

The crack-moment M_c in the beam-column element implies that the rupture will appear in the concrete fibers at the tensile edge of cross-section. Because the tension strength f_t in concrete is very small compared to compressive strength f'_c , the rupture in tensile concrete can appear even under a small external load. We also obtain a very small value of cracking moment compared with the yield-moment or ultimate-moment value.

In order to determine the value of the yield-moment M_y , we consider to the stress-time curve in tensile steel fiber. When stress in this steel fiber reaches the yield-strength f_y , we project it to the shape of moment-time curve for determining the value of yield-moment M_y . We note that, when the cross-section is designed following the limitations

in the code, we can always obtain the yield-moment when the steel tension reaches the yield-stress (see Fig.2.13).

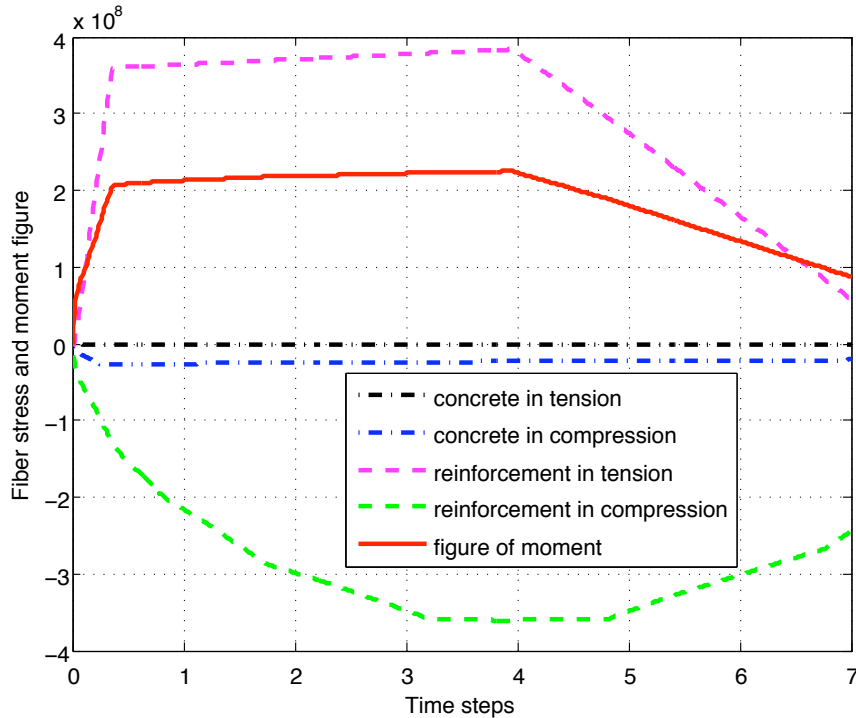


Figure 2.13: Stress-time fiber curve and moment-time curve

The last parameter we ought to obtain for defining constitutive behavior of stress-resultant beam-column element is the ultimate-moment M_u . We have to deal with two separate cases of compression in reinforced-concrete column: the large-eccentricity and the small-eccentricity. For the large-eccentricity in compression case, we always have the value of ultimate moment M_u equal to the maximum value of moment M_{max} for each types of cross-section. However, for the small-eccentricity compression case, we can choose this value of moment only by following the change of tangent modulus, namely, the point where the tangent modulus changes suddenly from the plastic phase to the softening phase can be considered as the one defining the corresponding value of the ultimate moment.

Beside the task of determination prominent values of moment-curvature couples, we need to determine the tangent modulus for the softening phase in order to fully define the moment-curvature curve for ultimate load computation. We assume that the point of time in the moment-time curve, where the compressive concrete fiber at the same position of the compressive steel fiber is damaged completely, is the point of time that the beam-

column element is not able to carry the load. From this point at the end of loading process after ultimate load in reinforced concrete beam or column can be determined, we may call this point in moment-curvature curve is the name as the terminal point (M_t, κ_t).

All of the necessary parameters (M_c, M_y, M_u, M_t) require separate computations of the resulting stress states for each prominent values of moment, we can also obtain the corresponding curvature values ($\kappa_c, \kappa_y, \kappa_u, \kappa_t$), as a part of the complete computation.

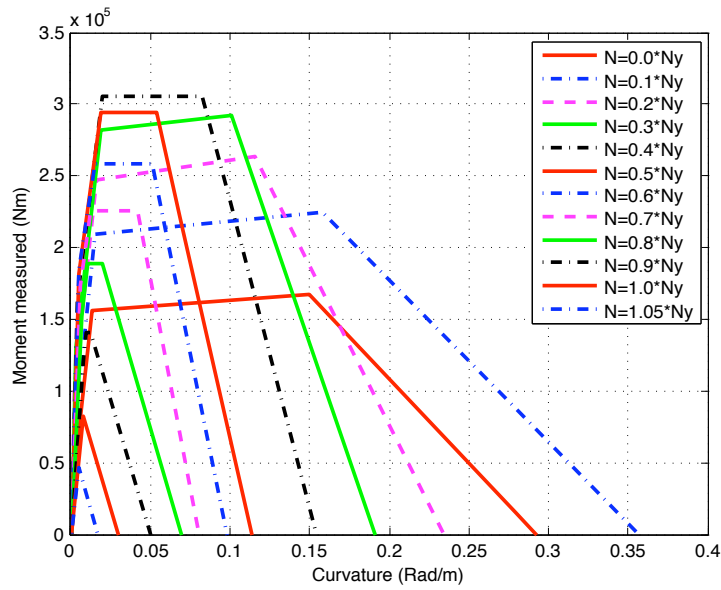


Figure 2.14: Moment-curvature diagrams in the refined curves

Having computed all necessary prominent values for the moment-curvature diagram, we can complete the description of moment-curvature for stress-resultant beam-column element for all computed cases. Following the main assumptions of the stress-resultant macro model for beam-column element, we choose to connect all the prominent points in moment-curvature diagram by the straight lines. This will further simply all of tangent moduli for that model (elastic, plastic hardening and softening) are represented as constant. In other words, knowing four sets of values of moment and curvature including (M_c, κ_c), (M_y, κ_y), (M_u, κ_u) and (M_t, κ_t), we can draw the new curves for each presented moment-curvature diagram to replace those obtained earlier multi-fiber model (see Fig.2.14). Since it is quite easy to determine the value of tangent modulus in the softening phase (the value of K_3 in the presented stress-resultant macro model), we draw the line of softening phase from the point of (M_t, κ_t) crossing the line with curvature and thus obtain the new point at the intersection with the couple ($M_p = 0$ and κ_p). It is therefore not difficult to determine this point and the value of κ_p , which further allows to replace the point of (M_t, κ_t) by the new point of (M_p, κ_p).

Collecting and arranging all prominent values of moments and of curvatures, for different ratio of external axial load value and yield axial force of the section ($n = N/N_y$), we can also define three corresponding relations between limit moment and the ratio n as presented in Fig.2.15.

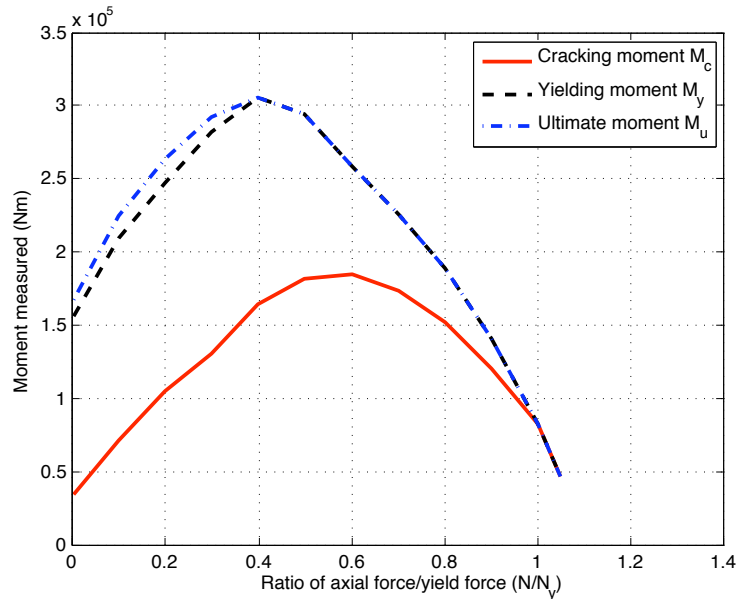


Figure 2.15: Cracking, yielding and ultimate moments with respect to N/N_y ratio

From this kind of relationship between the limit moment and loading ratio, we can recognize clearly the previously defined expression distinguishing two eccentricity compression cases. With the value of $n = N/N_y$ from zero to 0.4 or the external axial load increase we have the large-eccentricity compression case, where the values of yield and ultimate moments are increased following the non-linear behaviors. In the opposite, for further increase of n increase from 0.4 to 1.05, which is equivalent to increasing the external axial load, the values of yield and ultimate moments are descending following the non-linear behavior. Yield and ultimate moment have the same evolution with respect to n , and for that reason we chose the value of ultimate moment the same as the value of yield moment. Somewhat different behavior is defined by the curve of cracking moment versus the ratio of axial load and yield axial force n that reaches the maximum value of cracking moment M_c for value of n equal to 0.6.

We also compute the prominent values of curvature ($\kappa_c, \kappa_y, \kappa_u, \kappa_p$) with respect to the ratio of axial load and yield axial force ($n = N/N_y$), as presented in Fig.2.16. In trying to provide the best possible description of curvature variation, we have done some additional

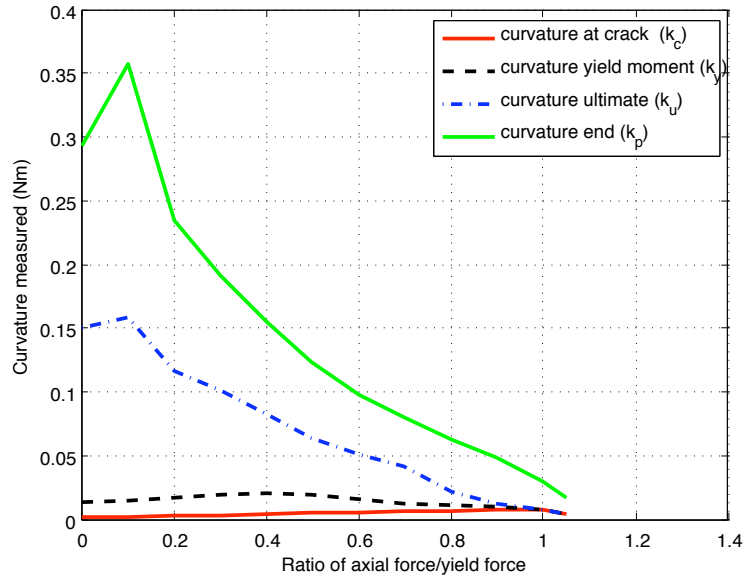


Figure 2.16: Prominent curvature values (κ_c , κ_y , κ_u , κ_p) with respect to $n = N/N_y$ ratio

computations with the effect of changing axial load with n between 0.0 and 0.1. In the figure presented above, we note that the curve shapes of curvature κ_u and κ_p are different from those of curvature κ_c and κ_y . For values of n between 0.0 and 0.1, the curves of κ_u and κ_p are increasing with linear behavior, but from 0.1 to 1.05 they are descending with non-linear behavior. The curve of κ_c increases with linear behavior following the increase of ratio, while the curve of κ_y increases with non-linear behavior and reaches the maximum value when the ratio of axial load is equal to 0.4.

In the next subsections, we shall present the curve fitting to compute the functions for limit-moments and limit-curvatures with respect to N_y , which are needed for developing the stress-resultant macro model.

3.3 Function identification for moment-axial force relation

In this section we discuss how to create a reliable representation of the limit value of moments and their dependence upon the applied axial force. This can be accomplished thank to the tool in *MATLAB* program that is called "cftool", which means Create-Function-Tool. With this tool, for a group of points in 2D coordinate system plane (x , y) we can provide the best fit for a function, either in terms of polynomial, exponential or power law depending upon the point positions within the group.

We first consider the point group of values for cracking moment, which is identified and presented in Fig. 2.15. Given different point positions, we could use two functions

for describing the best-fit relationship, namely, we could divide the curve at the point of $n = 0.6$, and thus then create two different functions for describing the non-linear behavior one for decreasing and another for increasing values of N/N_y . However, since the values of cracking moment are very small comparing to the values of yield or ultimate moments, we decided to use one function for this case. The comparison of function curve and point group of cracking moment is still quite acceptable, as shown in Fig.2.17.

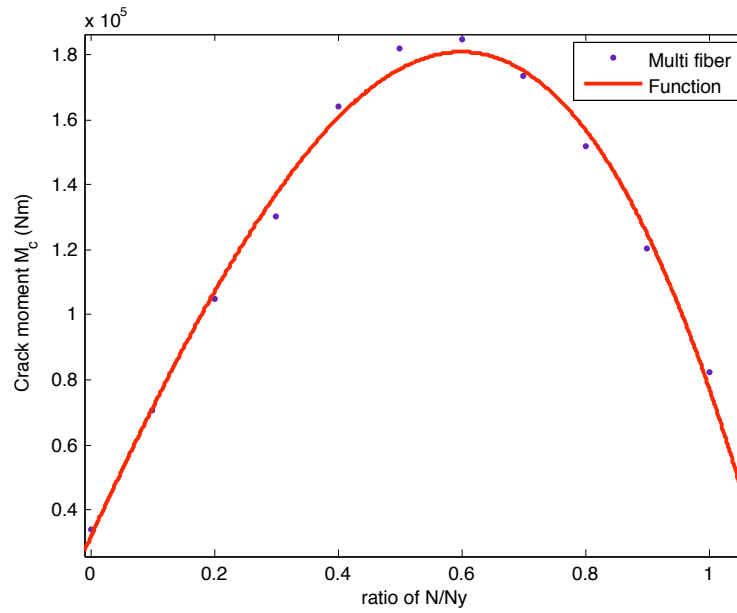


Figure 2.17: Best-fit function for cracking moment M_c variation with respect to $n = N/N_y$

This particular choice is a cubic polynomial function, that function can be expressed as $f(x) = p1 * x^3 + p2 * x^2 + p3 * x + p4$, where $f(x)$ denotes as the cracking moment limit value and x denotes as the corresponding argument of the function. Recall again that in this case, the argument x is equal, to n , the ratio of axial force and yield axial force ($n = N/N_y$), while the coefficients of function ($p1, p2, p3, p4$) are equal to $-2.245e + 05$, $-1.452e + 05$, $4.161e + 05$ and $3.168e + 04$ respectively. We can thus write the limit value of cracking moment as:

$$M_c = (-2.245 * n^3 - 1.452 * n^2 + 4.161 * n + 0.3168) * 10^5 \quad (2.6)$$

We can carry on with the best-fit function for point group of limit values for yielding moment. We note that the M_y at the point of $n = 0.4$ reaches the maximum value, thus we decide to divide the curve into two phases. The first phase covers the values of n from 0.0 to 0.4, with the curve that has the non-linear increasing behavior. The second phase that

covers the values of n from 0.4 to 1.05 is defined by a curve has the non-linear decreasing behavior. We can use different kinds of functions, such as a single cubic function as we have already done for describing the cracking moment or a couple of quadratic functions for describing the variation of yielding moment.

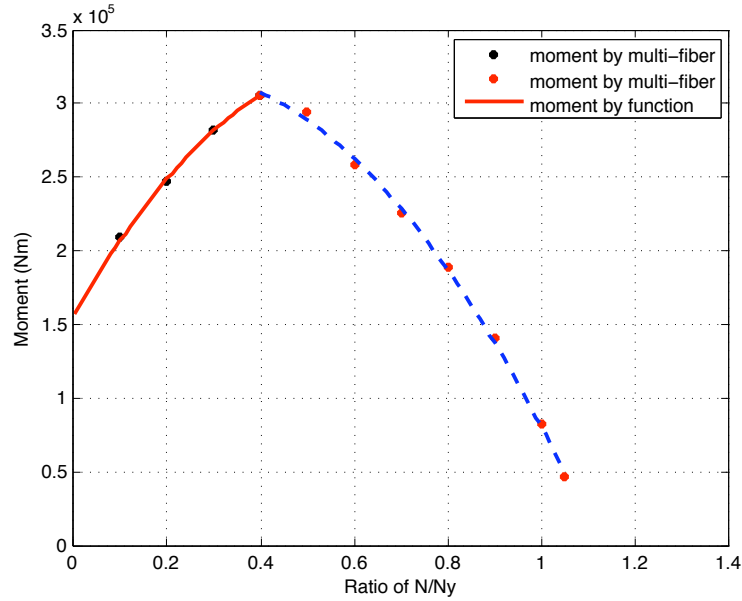


Figure 2.18: Best-fit function for yielding moment M_y variation with respect to $n = N/N_y$

After trying both options, we finally chose a couple of quadratic functions. The first function is used for describing the yielding moment variation for values of $n \in [0.0, 0.4]$ and the second one is used for remaining values of $n \in [0.4, 1.05]$. The chosen couple of function is presented in Fig.2.18, and each of two functions can be written as $f(x) = p1 * x^2 + p2 * x + p3$. For the first function, the coefficients $p1$, $p2$, $p3$ are respectively equal to $-4.449e + 05$, $5.506e + 05$, $1.566e + 05$, while for the second function, the coefficients are $p1 = -3.865e + 05$, $p2 = 1.639e + 05$, $p3 = 3.035e + 05$. Changing M_y for $f(x)$ and the ratio of axial load and yield axial force ($n = N/N_y$) for variable x in these functions, we can then re-write two quadratic functions expressing the corresponding limit value of yielding moment as:

$$\begin{aligned} M_y^{(1)} &= (-4.449 * n^2 + 5.506 * n + 1.566) * 10^5; \text{ for } n \in [0.0, 0.4] \\ M_y^{(2)} &= (-3.865 * n^2 + 1.639 * n + 3.035) * 10^5; \text{ for } n \in [0.4, 1.05] \end{aligned} \quad (2.7)$$

The last functions that ought to be created are those for the ultimate moment M_u . For the collected point group of ultimate moment limit values for different n , we can see that

the shape of the curve is very much the same as the one used for the yielding moment case, and hence we can also use two quadratic functions for describing the curves. The coefficients for the first function are respectively $p1 = -7.061e + 05$, $p2 = 6.282e + 05$, $p3 = 1.675e + 05$, whereas those for the second function are $p1 = -3.583e + 05$, $p2 = 1.28e + 05$, $p3 = 3.141e + 05$.

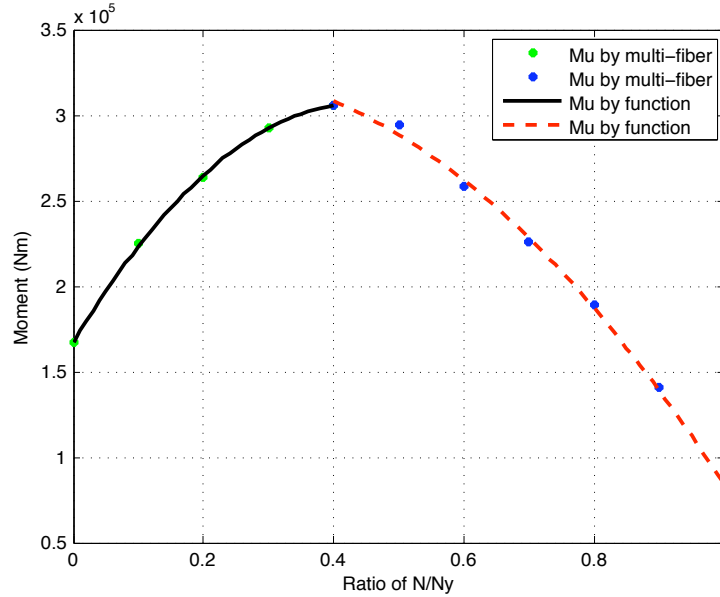


Figure 2.19: Best-fit function for ultimate-moment M_u variation with respect to $n = N/N_y$

After replacing $f(x)$ by M_u and x by n , we can write the functions describing the relationships between ultimate moment and ratio n as:

$$\begin{aligned}
 M_u^{(1)} &= (-7.061 * n^2 + 6.282 * n + 1.675) * 10^5; \text{ with } n \in [0.0, 0.4] \\
 M_u^{(2)} &= (-3.865 * n^2 + 1.280 * n + 3.141) * 10^5; \text{ with } n \in [0.4, 1.05]
 \end{aligned}
 \tag{2.8}$$

Comparing the expressions for functions chosen for $M_y^{(2)}$ and $M_u^{(2)}$, we recognize that values of M_y and M_u in the domain $n \in [0.4, 1.05]$ are very much the same. In other word, in the case of small-eccentricity of compression load in the reinforced-concrete column, the value of yield moment in cross section remains equal to the value of ultimate moment.

3.4 Function identification for curvature-axial force relations

The changes of limit values of moment under varying axial load should be accompanied by the corresponding values of limit curvature, which will also be changing. For

identification of the complete list of stress-resultant beam-column model parameters, it is also necessary to obtain the curvature dependence upon the change of axial load. We first consider the problem of how to define the function for limit value of curvature corresponding to the cracking moment. The arrangement of point group of values κ_c with respect to change of axial force, indicates the linear dependence on, so that we can use a linear polynomial for describing function as $f(x) = p1 * x + p2$. The computed values of coefficients are $p1 = 0.006882$ and $p2 = 0.001225$. Changing $f(x)$ by κ_c and x by n , we write a linear function for the relation between curvature at cracking moment and ratio of axial load and yield axial force as:

$$\kappa_c = (6.882 * n + 1.225) * 10^{-3} w \quad (2.9)$$

The excellent best-fit between the linear function and point group of κ_c is shown in Fig.2.20

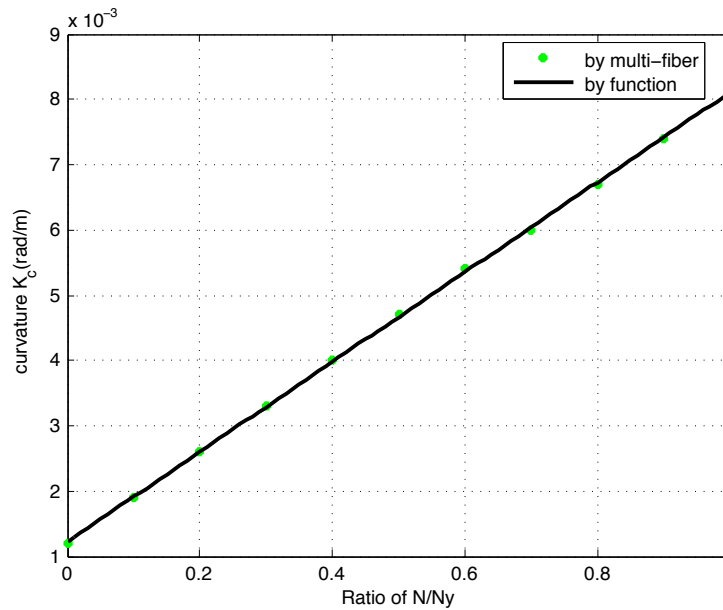


Figure 2.20: Function of curvature κ_c with $n = N/N_y$

The second best-fit function for curvature is obtained for the point group of limit values of curvature at yielding moment. The arrangement of points in this group indicates that the best-fit curve for κ_y should have non-linear behavior, with the maximum value $n = 0.4$. We have tested two kinds of function including a couple of cubic polynomial functions with the same value at $n = 0.4$ or a polynomial function with the degree higher than cubic polynomial. We finally decided to choose the polynomial function with 8th degree for describing the dependence of curvature at yielding moment upon the applied axial force. With such a choice we accepted less than perfect fit for the value of $n = N/N_y$

close to 1, since no reinforced concrete beam-column element submitted to both bending moment and axial force is likely to reach this kind of values for axial force; therefore, the use of 8th degree polynomial function for this case can be acceptable.

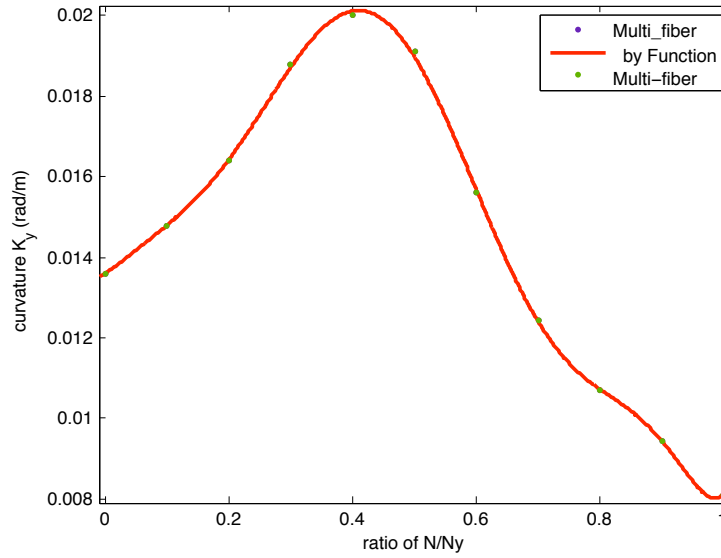


Figure 2.21: Best-fit function for curvature at yield moment variation with respect to N/Ny

The particular function can be expressed as $f(x) = p1 * x^8 + p2 * x^7 + p3 * x^6 + p4 * x^5 + \dots + p9$, where the values of coefficients of polynomial are defined as $p1 = 6.683$, $p2 = -24.14$, $p3 = 33.58$, $p4 = -22.22$, $p5 = 6.989$, $p6 = -0.9648$, $p7 = 0.06642$, $p8 = 0.009835$ and $p9 = 0.0136$. Replacing $f(x)$ by κ_y and x by n , we can thus write 8th degree polynomial function for describing the behavior of limit value of curvature for yielding moment with respect to ratio n as

$$\begin{aligned} \kappa_y = & 6.683 * n^8 - 24.14 * n^7 + 33.58 * n^6 - 22.22 * n^5 + 6.989 * n^4 \\ & - 0.9648 * n^3 + 0.06642 * n^2 + 0.009835 * n + 0.0136 \end{aligned} \quad (2.10)$$

The chosen function and point group are shown in Fig.2.21.

The next best-fit function that should be created concerns the point group of ultimate curvature κ_u corresponding to the ultimate moment M_u . There are two kinds of best-fit functions expressing the arrangement of point group: the first is linear for the values of $n \in [0.0, 0.1]$ and the second curve is non-linear for the remaining values of n . We use two best-fit functions for this case. The first function is a linear polynomial $f(x) = p1 * x + p2$ with coefficients $p1 = 0.084$ and $p2 = 0.15$. The second function is the exponential

function $f(x) = a * \exp(b * x) + c * \exp(d * x)$ with the coefficients $a = 0.191$, $b = -2.07$, $c = -0.0009861$ and $d = 2.943$.

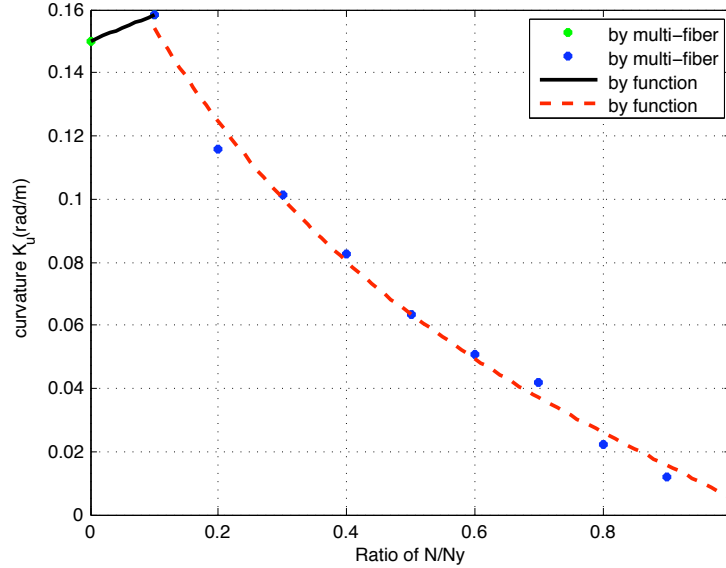


Figure 2.22: Best-fit function for curvature at ultimate moment variation with respect to N/N_y

Replacing $f(x)$ by κ_u and x by n , we can obtain two functions for describing the relationship between ultimate curvature and ratio of axial load and yield axial force $n = N/N_y$ as

$$\begin{aligned} \kappa_u^{(1)} &= 0.084 * n + 0.15; \text{ with } n \in [0.0, 0.1] \\ \kappa_u^{(2)} &= 0.191 * \exp(-2.07 * n) - 0.0009861 * \exp(2.943 * n); \text{ with } n \in [0.1, 1.05] \end{aligned} \quad (2.11)$$

The final choice of two functions and the point group are presented in Fig.2.22.

The last best-fit function that should be created concerns the point group of the curvature κ_p in reinforced concrete column, corresponding to a complete collapse with value of moment M_p equal to zero. Considering this point group, we note that it is very much the same as that of ultimate curvature case. Namely, there are two functions that ought to be created: the first one for linear behavior for the values of $n \in [0.0, 0.1]$ and the second one for non-linear behavior for the remaining values of $n \in [0.1, 1.05]$.

The best fit will thus provide: the first linear function $f(x) = p1 * x + p2$, with coefficients $p1 = 0.644$ and $p2 = 0.2926$, along with the second exponential function is $f(x) = a * \exp(b * x) + c * \exp(d * x)$ with coefficients $a = 6473$, $b = -115.9$, $c = 0.3715$

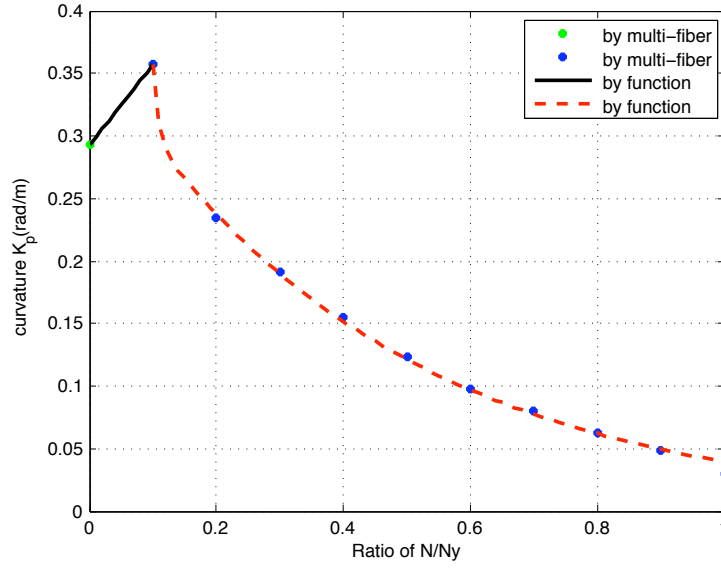


Figure 2.23: Best-fit function for curvature at rupture point κ_p variation with respect to $n=N/N_y$

and $d = -2.237$. By replacing κ_p for $f(x)$ and n for x , we can obtain two functions describing the behavior of κ_p with respect the ratio n as

$$\begin{aligned} \kappa_p^{(1)} &= 0.644 * n + 0.2926; \text{ with } n \in [0.0, 0.1] \\ \kappa_p^{(2)} &= 6473 * \exp(-115.9 * n) + 0.3715 * \exp(-2.237 * n); \text{ with } n \in [0.1, 1.05] \end{aligned} \quad (2.12)$$

The illustration of two functions and point group for κ_p is given in Fig.2.23.

With all the functions in hand, we can fully define the dependences of both limit moment (M_c, M_y, M_u) and limit values of curvature ($\kappa_c, \kappa_y, \kappa_u, \kappa_p$) upon ratio of axial load and yield axial force n . By exploiting those results, we can provide the method for computing the tangent moduli of the stress-resultant macro model for beam-column element of both plastic hardening and softening. This is presented next.

3.5 Moment and curvature yield functions for stress-resultant macro model at the time t

In each time step of numerical computation, we can obtain the current value of the axial force, further denoted as N^t for each element at the time t . Introducing this value of N^t into the yield functions $\Phi^M(M, N)$, as already defined in Subsection 3.1, we can find out the corresponding value of moment at the time t M^t in both plastic hardening and softening phases. Therefore, in the present stress-resultant macro model, the parameters of tangent

modulus and the value of limit moment for yield functions are as not remain fixed during the whole computation nor they are known in advance. In fact, for each value of axial force N^t at the time t we have the new value for both limit moment (M_i^t) and tangent modulus (K_i^t). Putting these two new values into a particular yield function at time step t , we shall find out the more exact value of moment for element in stress-resultant macro model. The limit values of moment and curvature at each time step can be obtained from the corresponding best-fit functions with the axial force as a variable, so that the value of tangent modulus can be formed as the combined function.

$$\begin{aligned} K_1^t &= (M_y^t - M_c^t) / (\kappa_y^t - \kappa_c^t) \\ K_2^t &= (M_u^t - M_y^t) / (\kappa_u^t - \kappa_y^t) \\ K_3^t &= (M_p^t - M_u^t) / (\kappa_p^t - \kappa_u^t) \end{aligned} \quad (2.13)$$

The group of yield function introducing in Subsection 3.1 can now be rewritten as the yield function dependent on a particular time step

$$\begin{aligned} \Phi^M(M^t, \zeta_i^M) &:= |M| - (M_i^t + K_i^t I \zeta_i^M) \leq 0 \\ \text{if } i = 1 &: \text{hardening phase 1} \Rightarrow M_i^t = M_c^t; K_i^t = K_1^t \text{ and } \zeta_i^M = \zeta_1^M \\ \text{if } i = 2 &: \text{hardening phase 2} \Rightarrow M_i^t = M_y^t; K_i^t = K_2^t \text{ and } \zeta_i^M = \zeta_2^M \\ \text{if } i = 3 &: \text{softening phase} \Rightarrow M_i^t = M_u^t; K_i^t = K_3^t \text{ and } \zeta_i^M = \zeta_3^M \\ \text{if } i = 4 &: \text{complete rupture} \Rightarrow M_i^t = 0; K_i^t = 0 \text{ and } \zeta_i^M = \zeta_4^M \end{aligned} \quad (2.14)$$

We also can rewrite yield function under the other type, in which we embed the moment functions and the modulus function as

$$\Phi^M(M, N, \zeta_i^M) := |M| - (M_i(N) + K_i(N) I \zeta_i^M) \leq 0 \quad (2.15)$$

It is important to note that the axial force is considered as a local variable in the yield function.

With this new value of the yield function for the stress-resultant macro model, we shall compare the results against those computed by the multi-fiber beam-column model. Several numerical examples are solved and presented in the next section.

4 Numerical applications

In this section we present several numerical examples in order to provide the illustration of a very satisfying performance of the progressed methodology. The first example has the purpose to present the local behavior of moment-curvature of the stress-resultant macro model for beam-column element. For that reason the analysis can be performed by a one

element mesh. The different loading programs are used: increasing, decreasing axial load and keeping load constant. In this manner we want to present the effect of axial loading change in beam-column element will have redefining the constitutive relationship for the new stress-resultant macro model for beam and column.

4.1 Single-element console computation

In this example, we use the built-in beam introduced in Section 3 see Fig. 2.10. This example is also used for computing and formulating the general behavior of moment-curvature. The computations are carried out for both multi-fiber and macro beam-column model. In each case, four types of loading program for axial load are applied to this element, while always keeping the same type of imposed rotation at the free end of the beam: the first case of loading is $N = 0$, the second is $N = 705\text{KN}$ that is also be kept constant, the third is N increasing from 705KN to 1029KN and the last one is N decreasing from 705KN to 211.5KN (see Fig.2.24).

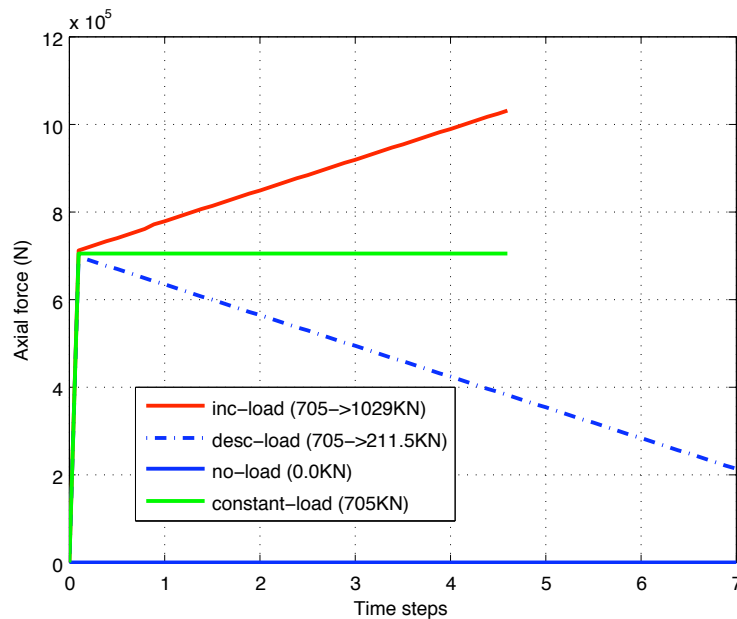


Figure 2.24: Axial loading program and its time evolution

In Fig.2.25 and Fig.2.26, we compare the local behavior of moment-curvature diagram in both cases with multi-fiber and stress-resultant macro model. We can see that the results for the corresponding diagrams to be used in the computation of macro model are in fact very close to those of the multi-fiber model. On the other hand, when comparing the time computation for both cases, the cost used for computation of macro model is much smaller than that for computation of multi-fiber model.

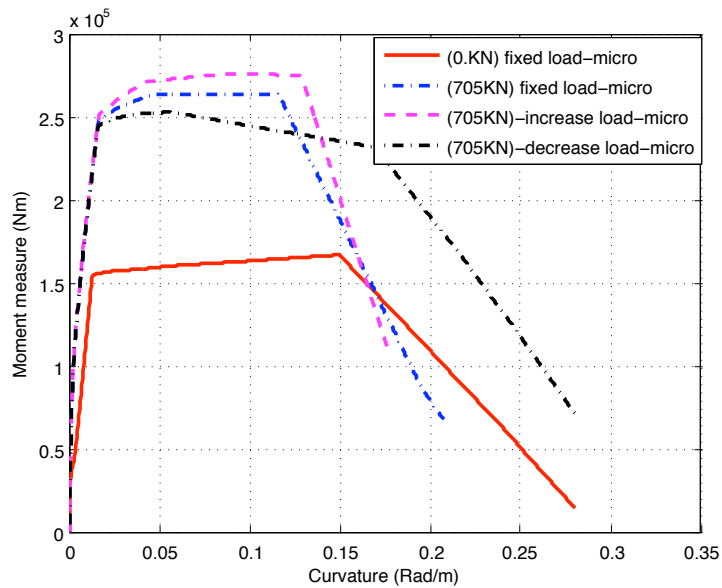


Figure 2.25: Multi-fiber computation for reinforced concrete single-element console

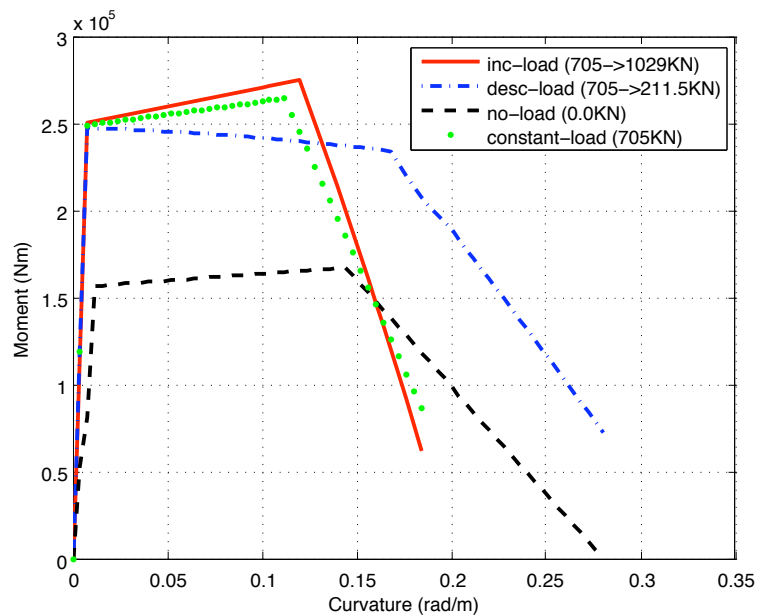


Figure 2.26: Stress-resultant beam macro computation for reinforced concrete single-element console

In next figures (2.27), (2.28) and (2.29), we present the operations of embedded moment functions in the new stress-resultant macro model. Although the change of axial load in this example is in a short distance comparing with $n = N/N_y$, but the presenting curves for M_c , M_y or M_u are correct to what is also presented in their functions. Following the time steps of changing the axial load, program can solve and give out many values of limit moments, but from what is presented in the curve of moment-curvature behavior of macro model, we recognize that by each couple of moment and axial load (counting with the fixed load function following the time $P(t)$), the limit-moment group be used in the yield-function (Φ^M) for each element is only one group.

We also present the curves of curvatures-loading time ($\kappa_c, \kappa_y, \kappa_u, \kappa_p$ with t) (see Fig.2.30, 2.31, 2.32 and 2.33), which is given out by the computation of macro model. Following the change of axial load and the computed results of tangent moduli (see 2.13), we can also figure out the relation between K_1, K_2, K_3 in the macro model with the loading time t (see Fig.2.34, 2.35 and 2.36).

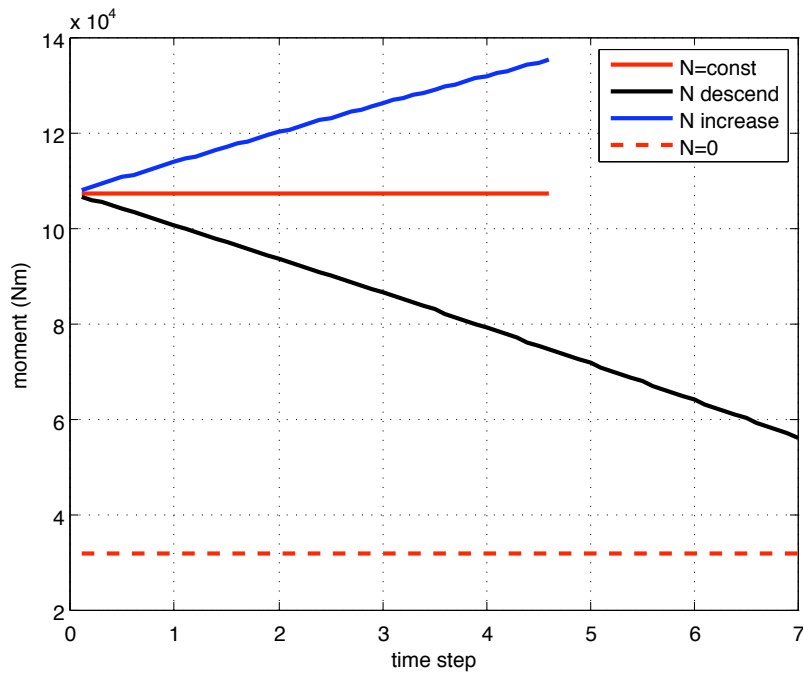


Figure 2.27: Change of cracking moment M_c

4.2 Two-storey reinforced concrete frame computation

We represent the example for computing a reinforced concrete frame with two-storey, which is also presented in the first part. In the first computation for this frame, we also obtained the results of both multi-fiber and stress-resultant macro models without change

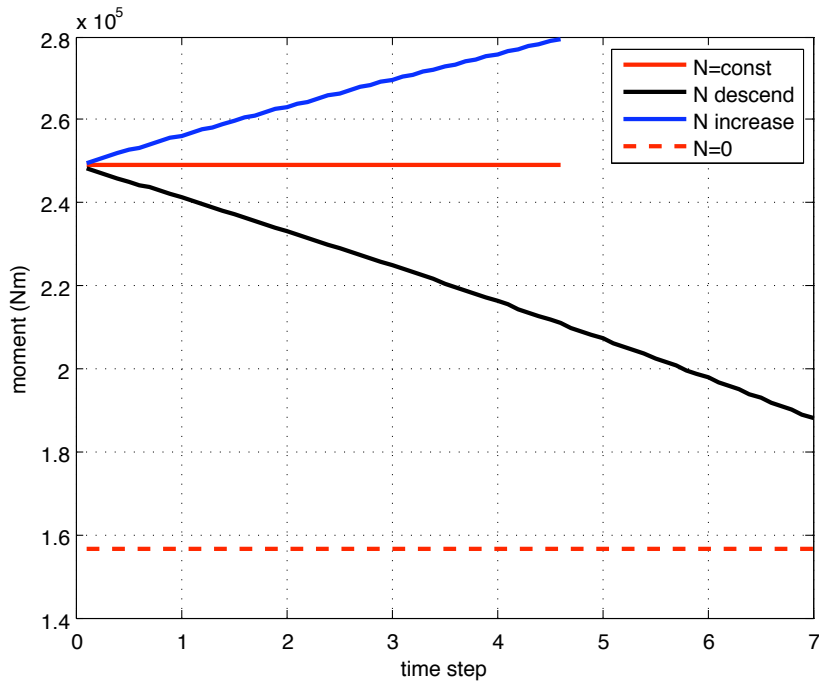


Figure 2.28: Change of yield moment M_y

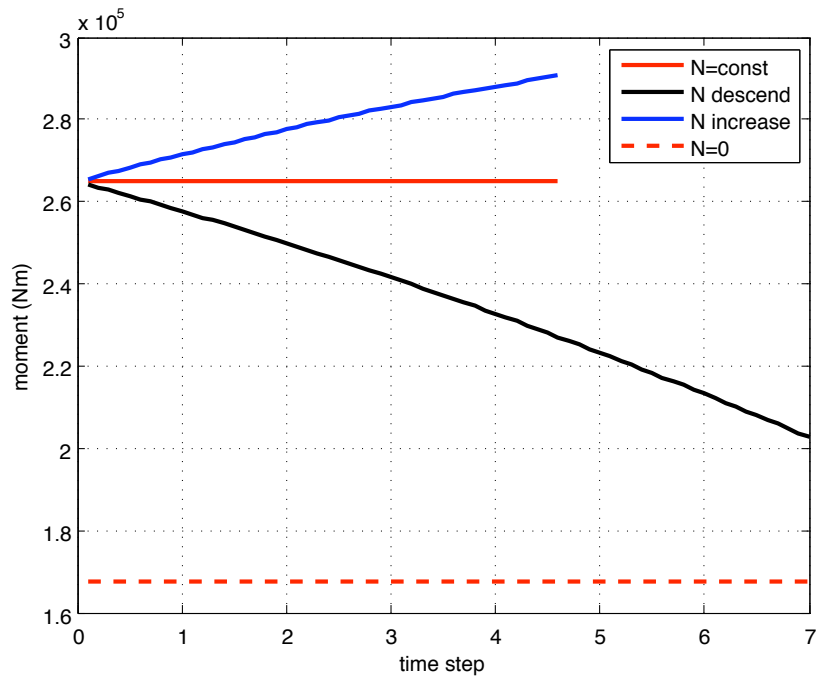


Figure 2.29: Change of ultimate moment M_u

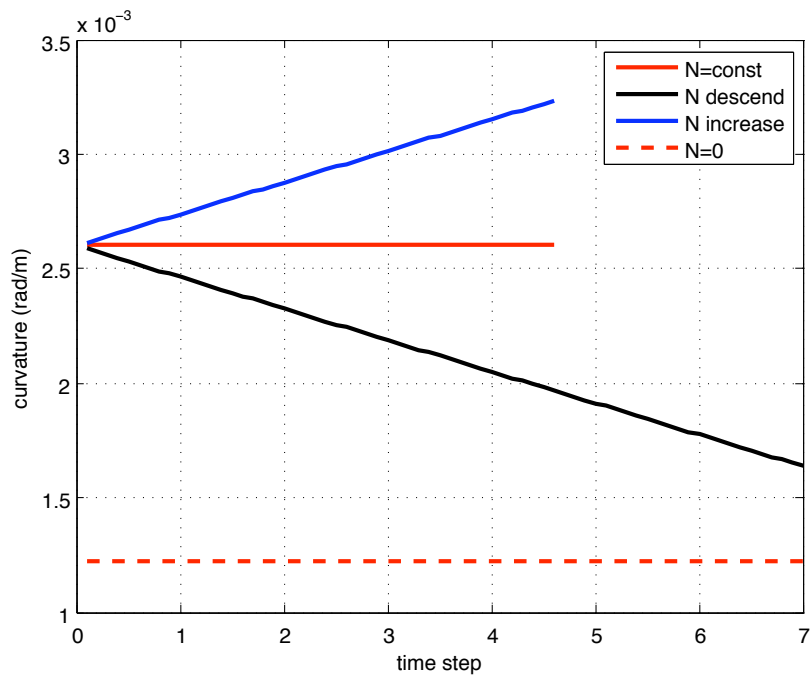


Figure 2.30: Change of crack-curvature κ_c

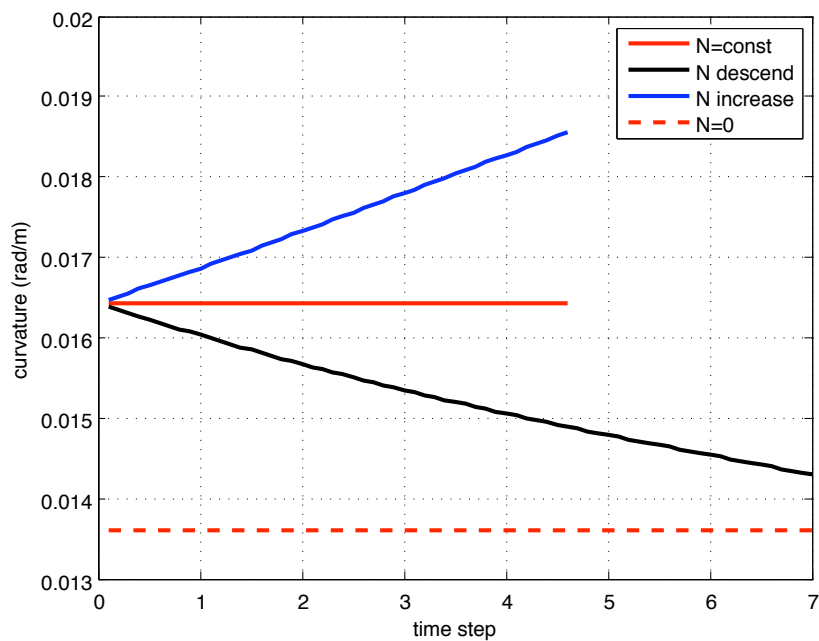


Figure 2.31: Change of yield-curvature κ_y

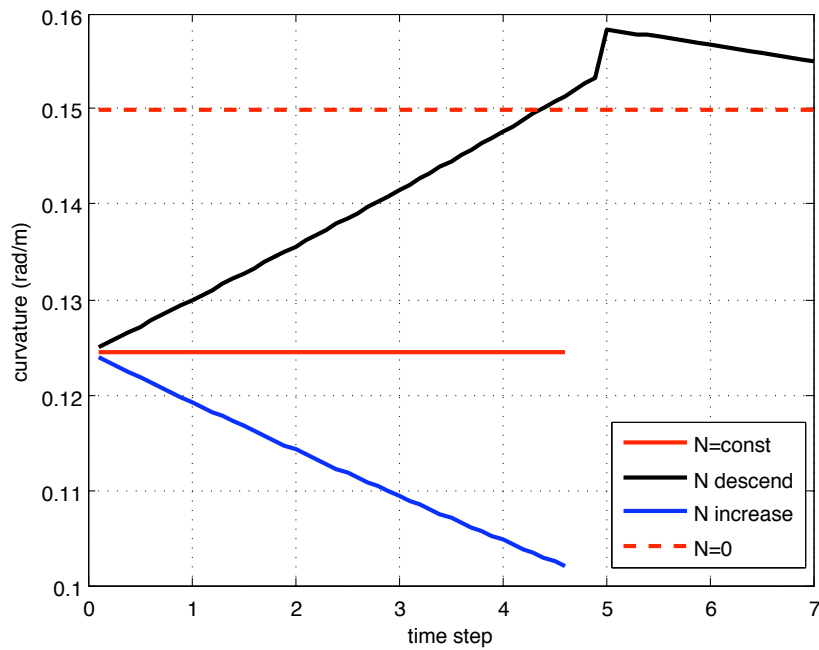


Figure 2.32: Change of ultimate-curvature κ_u

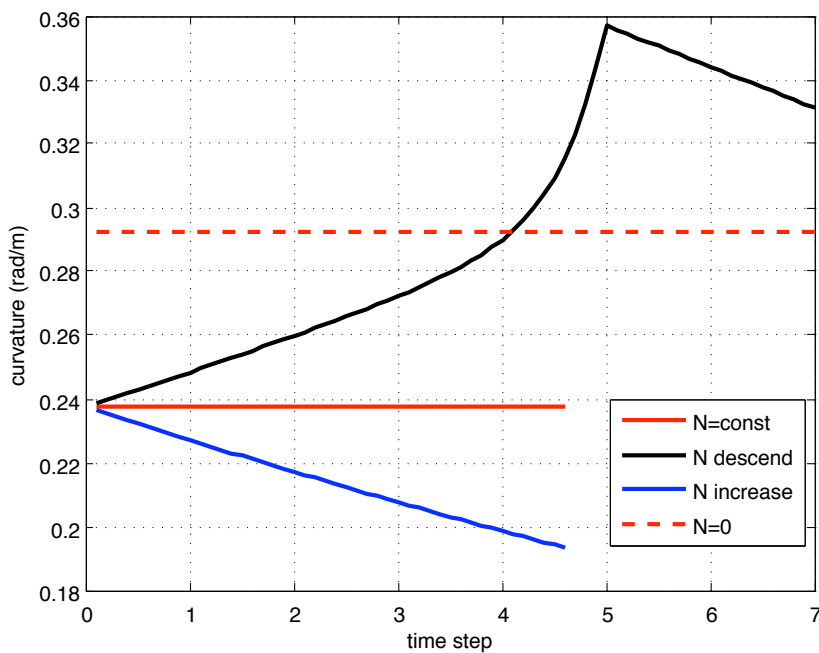


Figure 2.33: Change of curvature κ_p

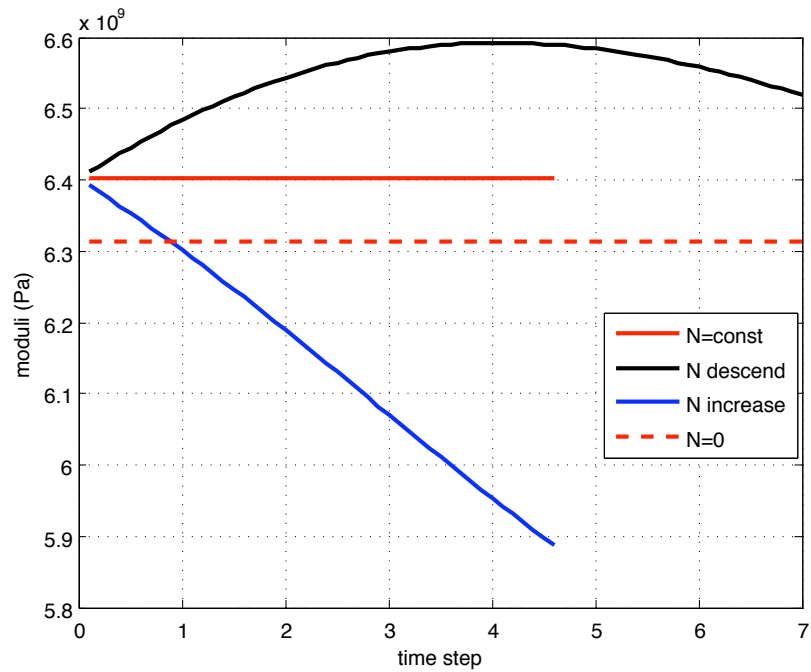


Figure 2.34: Change of hardening tangent K_1

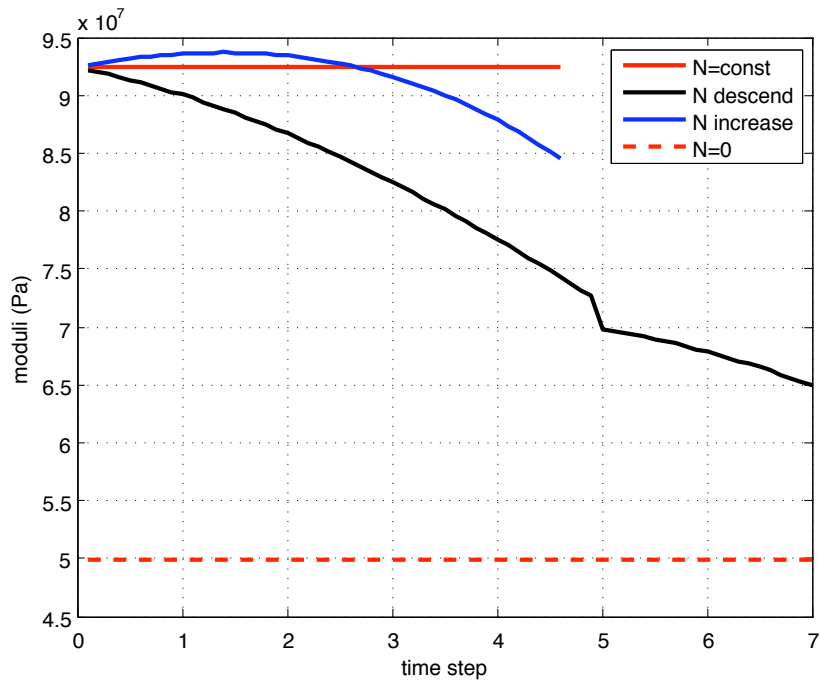


Figure 2.35: Change of hardening tangent K_2

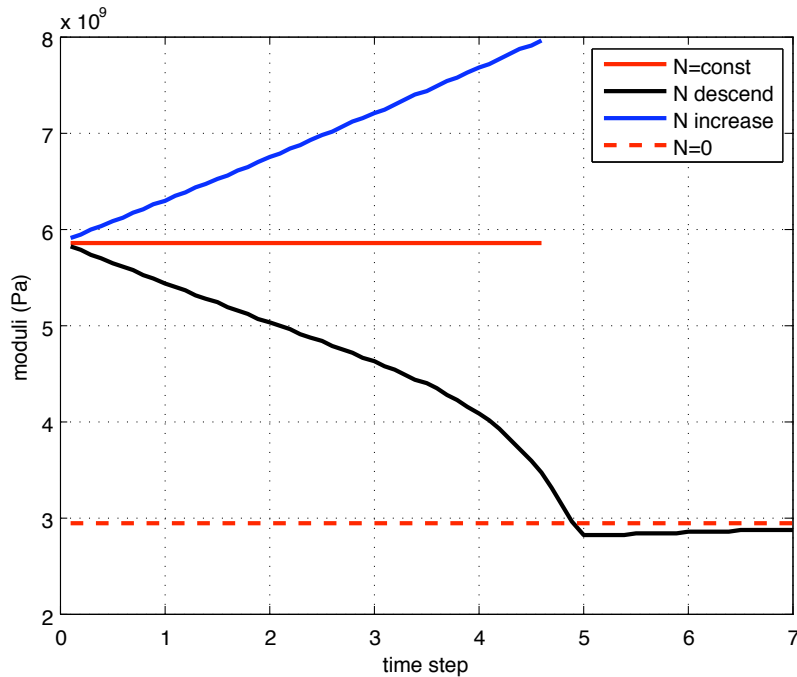


Figure 2.36: Change of softening tangent K_3

of limit moments in the yield function of macro model. With the moment functions embedded in the yield function of the stress-resultant macro model, we can obtain the better results comparing to the previous results.

Details of this reinforced concrete frame including the cross-section, the height of store and the span of frame can be seen in Fig.2.37. We also present the figure of the rotation displacement in frame computation in Fig.2.38. In this figure, the positions of plastic-hinge described as rotational discontinuity can be obtained. The orders of the appearances of plastic hinge are the same as those of presented in the first part.

In the relation of transverse load versus the deflection of the frame (see Fig.2.39), we present three curves: one for the experimental result, two remains for the stress-resultant macro model with and without the effects of embedded moment functions in yield functions. The continuous curve is expressed for the computation with the embedded moment function in the yield function, this curve is much more flexural comparing to the hidden curve of the case without embedded moment function in yield function of the previous stress-resultant macro model. When comparing the time for computation in both of multi-fiber and macro models, we always have the used time of the macro computation is always much smaller than that of multi-fiber model.

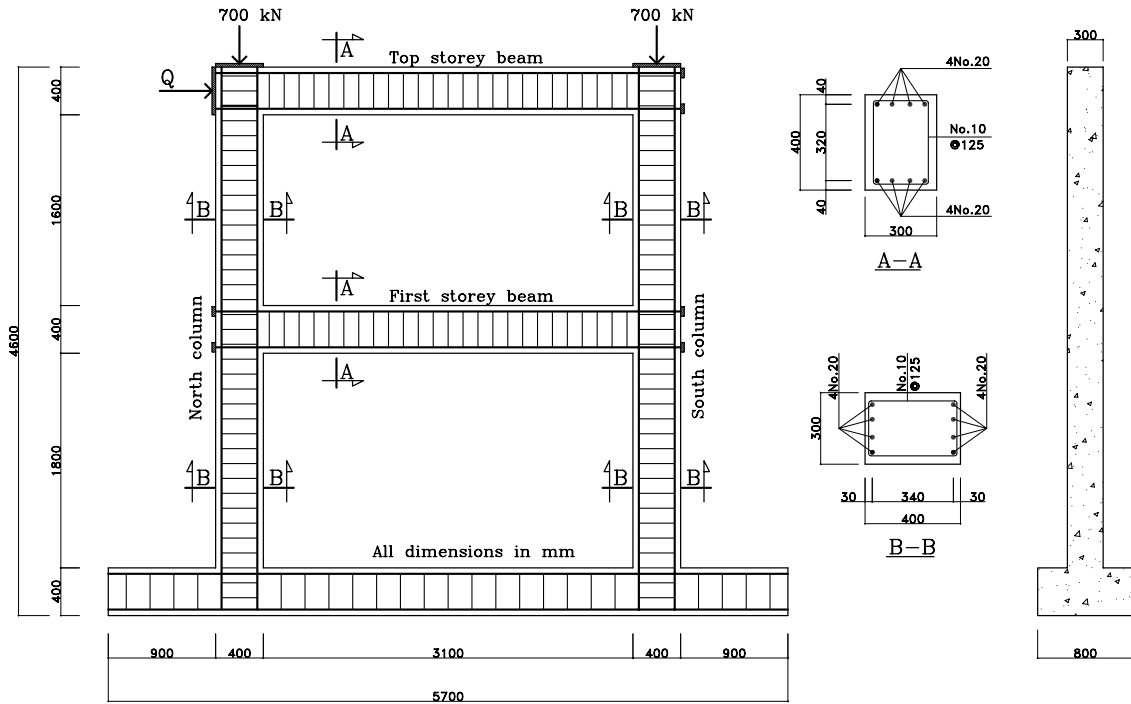


Figure 2.37: Detail of two-storey reinforced concrete frame

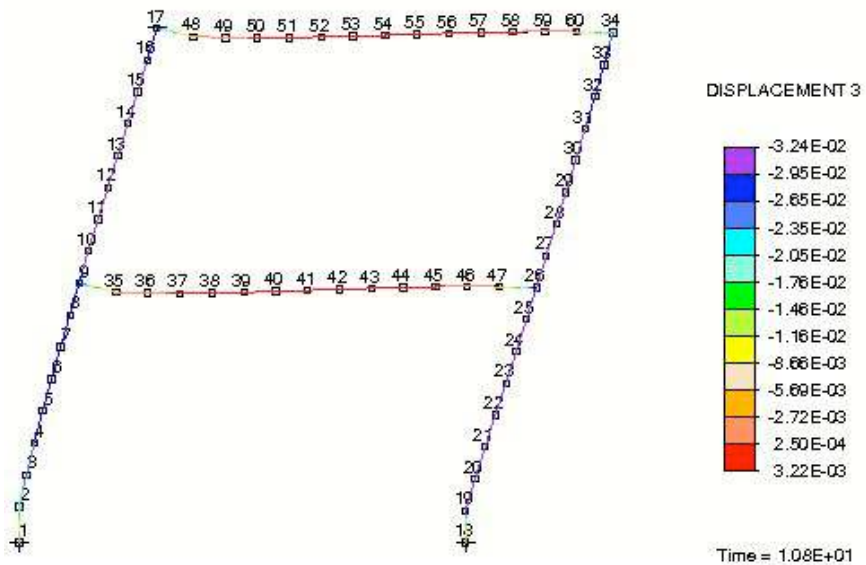


Figure 2.38: Rotation displacement of frame in computation

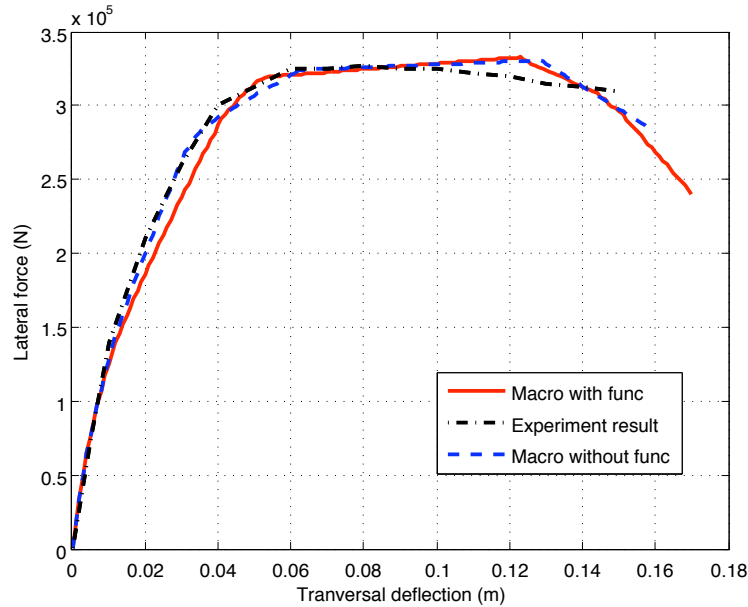


Figure 2.39: Transversal load and deflection in frame

5 Conclusion

In this work, we also present the main limitations in concrete and steel materials referred from Euro code 2, which is needed to give out the bases of the limit strains and stresses using for those computations in this paper. Some fundamental formulations and hypotheses for standard design and for computation are also given, those are basic for predicting the curves of limit moment in the yield function with the changes of the axial load.

In the multi-fiber model, where each fiber in the cross-section of element is considered as a bar with embedded strain discontinuity, it is used for computing a reinforced concrete built-in beam. This beam would be used as the fundamental element for identifying all necessary parameters used to create the best fit functions for limit values of moments and curvatures. Those best-fit functions are necessary for describing the change of limit moments in the yield functions of the stress-resultant macro model.

Several problems in the first part of the stress-resultant macro model is now solved. Those problems are when the axial force changed in the element of column, the corresponding limit moments in the yield function ought to be changed. With this new macro model, we still can compute the reinforced-concrete frame with the small time comparing to other models.

Two numerical examples are presented, one for purpose to describe the work of el-

ement at the local level, while the other for testing the new macro model at the global level. With the motivation to obtain the better stress-resultant macro model has capability to compute the frame with the appearances of plastic-hinges by effects of ultimate moment and/or ultimate shear force, we consider to continue developing this stress-resultant macro model. In addition, we shall a X-FEM model, which is fully detailed for all of main components, such as bond-slip of reinforcement, non-linear behavior of concrete, embedded strain discontinuities in 2D plate element with the aim to obtain useful model.

Chapter 3

Stress resultant and multi-fiber beam model with shear failure and crack spacing

In this work, a new version of the stress-resultant macro model for reinforced-concrete beam-column is developed with the new appearance of transverse displacement discontinuity beside the rotational discontinuity and combined bending moment and axial force, which are presented in previous macro model. Its ability to compute in the macro level is the more improved and the more relied, without changing the efficiency of computational cost. The idea for choosing the length of beam element is also considered by observing the contours of stress or displacement diagram of one X-FEM model for the reinforced concrete structure, in which full details of the behavior of each component such as the concrete with non-linear behavior, the steel and bond-slip problem are assigned to the 2D plate element, where the strain discontinuity is embedded. Several numerical computations using the new stress-resultant macro model and multi-fiber model are executed and compared with the result of X-FEM model for the purpose to recognize some main differences in the global behavior of three models.

Contents

1	Introduction	71
2	Reinforced concrete model and its finite element implementation	72
2.1	Concrete, bond-slip and steel models	72
2.2	Numerical formulation of the reinforced concrete element	76
2.3	Numerical examples	78
3	Stress-resultant macro model: embedded displacement discontinuities .	81
3.1	Theoretical formulation and finite element representation	83
3.2	Stress-resultant constitutive laws	88
4	Numerical examples	91
5	Conclusions	93

1 Introduction

The computation of the behavior of reinforced concrete structures requires in limited situations a fine description of the fracture mechanisms involved in the collapse of the structure namely, the concrete fracture, bond-slip fracture and finally eventually steel fracture. Nevertheless, in a great majority of the cases and for design applications, a coarser description of the behavior provided is takes into account all the localized phenomena such as plastic hinges could be sufficient to understand and predict the fracture mechanisms.

In that context, we present here a so-called Timoshenko beam macro-model capable of taking into account the phenomena involved during the rupture of reinforced concrete structures. In order to build the beam macro-model we use a detailed micro-model incorporating a 2D description of the fracture of reinforced concrete structures.

In the first part, the problem about bending failure in Timoshenko beam for reinforced-concrete material can be also solved by the stress-resultant macro model, where the rotational discontinuity is consider and embedded inside the beam element for describing the failure mechanism in the frame structure as the appearance of plastic-hinges. In the next step of the second step, the problem about combined bending moment and axial force is considered for developing the stress-resultant macro model become the new version. This model now can solve the frame structure with the change of both moment and axial load affecting in the cross-section of each reinforced-concrete element. The computational result of particular beam-column element at local level or of the whole frame structure at the global level now is more effective. However, this macro model still contents several limitations, for example when the shear load or transverse load is very big, while the shear-load capacity of the cross-section is not enough under external transverse load action, the frame structure may be collapsed by the shear load before reaching at the limitation of ultimate moment.

The other important problem when using finite element computational method is the dimension of element. Many papers, recently, consider this problem, especially when involving in reinforced-concrete material and the appearance of the strain discontinuity. We use a X-FEM model for observing and recognizing the appearance, positions as well as distances between macro cracks in the tension zone of the flexion beam. This model is modeled by the full consideration of the main factors including the non-linear behavior problem of the concrete and the steel reinforcement materials as well as the embedded strain discontinuity in the 2D-plate element, also including the appeared bond-slip inside model (see [53]). With knowing the distances of macro crack, a suitable choice for the beam element length is considered to apply into the stress-resultant macro model for optimizing the mesh in the frame structure.

For those necessary problems discussed above, we consider to embed transverse displacement discontinuity inside beam element at the middle point, where the rotational discontinuity is also embedded and presented in two previous parts, beside considering the suitable beam element length for stress-resultant macro model for beam-column. This new macro model capacities to compute frame structure with ultimate load, that concerns two couples of main failure cases: one for combined bending moment and axial force and

the other for combined shear force and axial force.

In this work, we present the main ingredients of both micro and macro model used for the description of the behavior until total failure of reinforced concrete beams. In order to present, the material models of concrete and steel as well as the bond-slip problem are introduced in Section 2. In Section 3, namely Stress-resultant macro model: embedded displacement discontinuities, we present some theoretical formulations and finite-element representation as well as the stress-resultant constitutive laws. Several numerical examples using both multi-fiber and macro models are presented in Section 4 and compare the global response with X-FEM model. Several main conclusions and perspectives are presented in the last section.

2 Reinforced concrete model and its finite element implementation

In this section, we present the main ingredients of the model used for the detailed description of reinforced concrete behavior. The proposed model takes into account the failure of concrete, the bond-slip behavior as well as the plastic yielding of the steel rebars. The main goal of this model is to provide standard global quantities used for optimal design (ultimate load, dissipated energy, ...) but also more specific quantities such as crack spacing, crack opening or bond-slip.

2.1 Concrete, bond-slip and steel models

2.1.1 Concrete model

The model used herein for the concrete behavior takes into account three phases: a first elastic phase followed by the development of randomly distributed micro-cracks leading to so-called fracture process zone and characterized by a bulk dissipation and finally the coalescence of micro-cracks and creation of a macro-crack responsible for the complete failure of the structure. The fracture process zone is represented, in the proposed model, by an isotropic continuum damage model whereas the macro-crack effect is taken into account considering a displacement discontinuity and related interface damage model producing localized dissipation.

All the details of the formulation of the concrete model used in this work are presented in [29], we give here only the key points of such a model. We give some words on the kinematic enrichment, the bulk and discontinuity behaviors and finally on the finite element implementation of such a model.

Kinematics

The model presented here lies in the framework of the strong discontinuity approach. The main originality of the present work is to combine bulk and localized dissipation in order to take into account both the effects of fracture process zone and localization

zones. For that purpose, the total strain field is enriched with a singular contribution corresponding to the displacement discontinuity contribution of the macro-crack so that we have for the concrete :

$$\boldsymbol{\varepsilon}^c(x, t) = \underbrace{\bar{\boldsymbol{\varepsilon}}^c(x, t)}_{\nabla^s \mathbf{u}} + \mathbf{G}_r \boldsymbol{\alpha}^c(t) + \delta_\Gamma(x) (\bar{\mathbf{u}}(t) \otimes \mathbf{n})^s \quad (3.1)$$

where \mathbf{n} denotes the unit normal vector to the discontinuity surface Γ , \mathbf{u} denotes the regular part of the displacement and $\bar{\mathbf{u}}$ refers to the displacement jump on the surface of discontinuity Γ . Finally, \mathbf{G}_r is the function allowing to manage the influence of the macro-crack on the fracture process zone.

Material behaviors

Two models have to be implemented in order to describe the whole behavior of concrete from its sound state to its complete failure : one manages the bulk dissipation (referred to as the continuum model) and the other one is related to the localized dissipation produced by the development of a macro-crack (referred to as the discrete model). Those two models are written in the framework of the thermodynamics of continuum media and interfaces in two very similar ways considering damage phenomena both for the bulk and for the interface. Table 3.1 gives the main ingredients for the construction of the two constitutive laws.

	Continuum model	Discrete model
Helmholtz free energy	$\bar{\Psi}(\bar{\boldsymbol{\varepsilon}}, \bar{\mathbf{D}}, \bar{\xi}) = \frac{1}{2} \bar{\boldsymbol{\varepsilon}} : \bar{\mathbf{D}}^{-1} : \bar{\boldsymbol{\varepsilon}} + \bar{\Xi}(\bar{\xi})$	$\bar{\Psi}(\bar{\mathbf{u}}, \bar{\mathbf{Q}}, \bar{\xi}) = \frac{1}{2} \bar{\mathbf{u}} \cdot \bar{\mathbf{Q}}^{-1} \cdot \bar{\mathbf{u}} + \bar{\Xi}(\bar{\xi})$
Yield function(s)	$\bar{\phi}(\boldsymbol{\sigma}, \bar{q}) = \underbrace{\sqrt{\boldsymbol{\sigma} : \mathbf{D}^e : \boldsymbol{\sigma}}}_{\ \boldsymbol{\sigma}\ _{\mathbf{D}^e}} - \frac{1}{\sqrt{E}} (\sigma_f - \bar{q})$	$\bar{\phi}_1(\mathbf{t}_{\Gamma_s}, \bar{q}) = \mathbf{t}_{\Gamma_s} \cdot \mathbf{n} - (\bar{\sigma}_f - \bar{q})$ $\bar{\phi}_2(\mathbf{t}_{\Gamma_s}, \bar{q}) = \mathbf{t}_{\Gamma_s} \cdot \mathbf{m} - (\bar{\sigma}_s - \frac{\bar{\sigma}_s}{\bar{\sigma}_f} \bar{q})$
State equations	$\boldsymbol{\sigma} = \bar{\mathbf{D}}^{-1} : \bar{\boldsymbol{\varepsilon}} \quad \text{and} \quad \bar{q} = -\frac{d}{d\bar{\xi}} \bar{\Xi}(\bar{\xi})$	$\mathbf{t}_{\Gamma_s} = \bar{\mathbf{Q}}^{-1} \cdot \bar{\mathbf{u}} \quad \text{and} \quad \bar{q} = -\frac{\partial \bar{\Xi}}{\partial \bar{\xi}}$
Evolution equations	$\dot{\bar{\mathbf{D}}} = \dot{\gamma} \frac{\partial \bar{\phi}}{\partial \boldsymbol{\sigma}} \otimes \frac{\partial \bar{\phi}}{\partial \boldsymbol{\sigma}} \frac{1}{\ \boldsymbol{\sigma}\ _{\mathbf{D}^e}}$ $\dot{\bar{\xi}} = \dot{\gamma} \frac{\partial \bar{\phi}}{\partial \bar{q}}$	$\dot{\bar{\mathbf{Q}}} = \dot{\gamma}_1 \frac{1}{\mathbf{t}_{\Gamma_s} \cdot \mathbf{n}} + \dot{\gamma}_2 \frac{1}{ \mathbf{t}_{\Gamma_s} \cdot \mathbf{m} }$ $\dot{\bar{\xi}} = \dot{\gamma}_1 + \frac{\bar{\sigma}_s}{\bar{\sigma}_f} \dot{\gamma}_2$
Dissipation	$0 \leq \bar{\mathcal{D}} = \frac{1}{2} \dot{\bar{\xi}} (\bar{\sigma}_f - \bar{K} \bar{\xi})$	$0 \leq \bar{\mathcal{D}} = \frac{1}{2} \dot{\bar{\xi}} (\bar{\sigma}_f - \bar{K} \bar{\xi})$

Table 3.1: Main ingredients of the construction of the two damage models

In table 3.1, the variables $\dot{\gamma}$, $\dot{\gamma}_1$ and $\dot{\gamma}_2$ denote Lagrange multipliers induced by the use of the maximum dissipation principle. $\bar{\mathbf{D}}$ and $\bar{\mathbf{Q}}$ correspond to the damaged compliance of the continuum and discrete model, respectively. In the following, the isotropic hardening law associated to the discrete models chosen as :

$$\bar{q} = \bar{\sigma}_f \left[1 - \exp \left(-\frac{\bar{\beta}}{\bar{\sigma}_f} \bar{\xi} \right) \right] \quad (3.2)$$

In a finite element context, those two models are integrated using a Return Mapping algorithm.

Finite element implementation

The main deal for the finite element implementation is to choose the influence function \mathbf{G}_r and to take it into account in the weak form of the equilibrium equation. We've chosen here to work with a Constant Strain Triangle (CST), in [22], for which the influence function \mathbf{G}_r is chosen as:

$$\mathbf{G}_r = - \sum_{i \in \Omega^+} \nabla^s N_i \quad (3.3)$$

where N_i denotes the standard finite element shape function associated to node i .

The weak form of the equilibrium equation is then obtained by considering the Incompatible Modes Method (see in [6]) and introducing a virtual strain field $\gamma^c(x, t)$ constructed from a slightly modified version of the influence function in order to pass the patch test in [22]:

$$\gamma^c(x, t) = \bar{\gamma}^c(x, t) + \mathbf{G}_v \beta^c(t) + \delta_\Gamma(x) (\beta^c(t) \otimes \mathbf{n})^s \quad (3.4)$$

with

$$\mathbf{G}_v = \mathbf{G}_r - \frac{1}{\Omega^e} \int_{\Omega^e} \mathbf{G}_r d\Omega^e \quad (3.5)$$

By appealing to the incompatible Modes Method, the problem solution (nodal displacements and displacement jumps) is obtained by the resolution of a system of two equations the classical discrete global equilibrium equation modified by the effect of the discontinuity and a local equation which written on each localized element and which can be interpreted as the weak form of the traction continuity along the surface of discontinuity:

$$\begin{cases} \sum_{e=1}^{N_{elem}} \mathbf{A} [\mathbf{f}^{e,int}(t) - \mathbf{f}^{e,ext}(t)] = \mathbf{0} \\ \int_{\Omega^e} \mathbf{G}_v^T \boldsymbol{\sigma} d\Omega^e - \int_{\Gamma} \underbrace{\mathbf{t}_\Gamma}_{(\boldsymbol{\sigma} \cdot \mathbf{n})|_\Gamma} d\Gamma = \mathbf{0} \end{cases} \quad (3.6)$$

This set of equations is solved by an operator split method, the local equilibrium equation is solved locally on each localized element and then by static condensation at the

element level, the nodal displacements are obtained iteratively as solution of an equation of the form:

$$\sum_{e=1}^{Nelem} [\hat{\mathbf{K}}^e \Delta \mathbf{d}_{n+1}^{(i)} = \mathbf{f}_{n+1}^{e,ext} - \mathbf{f}_{n+1}^{e,int(i)}] \quad (3.7)$$

where $\hat{\mathbf{K}}^e$ is the tangent stiffness of element e modified to take into account the effect of the discontinuity.

2.1.2 Bond-slip model

The bond-slip model is introduced to describe the behavior of the concrete-steel interface. The bond-slip behavior is represented through the shear strain at the interface and its shear resistance should be dependent on the normal pressure. In order to implement such a model, a Drucker-Prager non associative plasticity model has been chosen leading to a yield function of the form:

$$\phi^{bs}(\boldsymbol{\sigma}) = \sqrt{\frac{3}{2}} \|\text{dev}[\boldsymbol{\sigma}]\| - \kappa(p) \leq 0; \quad \kappa(p) = \sigma_c - pf; \quad p = \frac{1}{3} \text{tr}[\boldsymbol{\sigma}] \quad (3.8)$$

where $\text{dev}[\boldsymbol{\sigma}]$ and $\text{tr}[\boldsymbol{\sigma}]$ denote respectively the deviatoric and spherical part of the stress tensor, and σ_c is the sliding resistance at zero pressure, with no confinement.

In addition, the slip or plastic deformation evolution is governed by a von-Mises plastic potential so that we have:

$$\dot{\epsilon}^p = \dot{\gamma} \frac{\partial \phi^{vm}(\boldsymbol{\sigma})}{\partial \boldsymbol{\sigma}} \quad \text{with} \quad \phi^{vm}(\boldsymbol{\sigma}) = \sqrt{\frac{3}{2}} \|\text{dev}[\boldsymbol{\sigma}]\| - \sigma_y \quad (3.9)$$

The integration of the constitutive equations is carried out using a return-mapping algorithm.

The finite element implementation of the bond-slip is performed through the use of a 4-node quadrilateral element of geometrically zero thickness (the nodes are coincident by pairs). The key point to deal with the zero thickness of the element is to introduce a penalty-like parameter s which allows to compute the derivatives of the shape functions as if the element was of thickness h_{pen} .

If we consider an element aligned with the global coordinates (x, y) of the problem, then we have for the derivatives of the shape functions the following results ($x_1 = x_4$, $x_2 = x_3$ and $y_4 = y_1 + h_{pen}$, $y_3 = y_2 + h_{pen}$):

$$\begin{aligned} x_{,\xi} &= \frac{\ell^e}{2}, \quad x_{,\eta} = 0, \quad y_{,\xi} = 0, \quad y_{,\eta} = \frac{h_{pen}}{2} \\ N_{a,x} &= \frac{N_{a,\xi} y_{,\eta} - N_{a,\eta} y_{,\xi}}{j} = \frac{\xi_a(1 + \eta_a \eta)}{2\ell^e}, \quad N_{a,y} = -\frac{N_{a,\xi} x_{,\eta} - N_{a,\eta} x_{,\xi}}{j} = \frac{\eta_a(1 + \xi_a \xi)}{2h_{pen}} \end{aligned} \quad (3.10)$$

where j denotes the element jacobian equal to $j = x_{,\xi} y_{,\eta} - x_{,\eta} y_{,\xi} = \frac{\ell^e h_{pen}}{4}$.

2.1.3 Steel model

The final ingredient to be defined is the choice for the modelling of the behavior of the steel rebars. Steel rebars are, in this work, described by using 2-node bar elements and a standard elasto-plastic model with isotropic hardening.

The yield function for the rebars is then given by:

$$\phi^s(\sigma) = |\sigma| - (\sigma_y + K\zeta) \leq 0 \quad (3.11)$$

with the classical stress state equation in plasticity:

$$\sigma = E(\varepsilon - \varepsilon^p) \quad (3.12)$$

where the evolution for ε^p is given by:

$$\dot{\varepsilon}^p = \dot{\gamma} \frac{\partial \phi^s}{\partial \sigma} \quad (3.13)$$

The tangent stiffness matrix of the steel rebars related to the nodal steel displacement is then of the form (in the local coordinate frame associated to the steel rebars):

$$K_{n+1}^s = \frac{C_{n+1}^{ep} A}{\ell} \begin{bmatrix} 1 & -1 \\ -1 & 1 \end{bmatrix} \quad (3.14)$$

where C_{n+1}^{ep} is the consistent tangent operator (see [36]), A denotes the rebars cross-section and ℓ their length.

2.2 Numerical formulation of the reinforced concrete element

The originality of the proposed strategy is to embed in a single finite element all the components of reinforced concrete described previously that is concrete, bond-slip and steel. This is achieved by enriching the kinematics of the element in order to take into account the specific kinematic relations between the three components of reinforced concrete. More precisely, incompatible modes enhancements are used to handle the concrete failure (see [29]), whereas XFEM-type enrichments are used for representing bond-slip along steel rebars. A macro-element including all the components is thus designed.

Figure 3.1 presents the proposed macro-element and its degrees of freedom. The macro-element is divided into 3 parts : the concrete part, the steel rebar and the bond-slip represented by a degenerated four node quadrangular element. With such a representation, we can either consider the absolute displacements of steel and concrete, the bond-slip displacement is then deduced from the two previous or consider the displacement of concrete and displacement of bond-slip relative to concrete and deduce the displacement of steel.

In the following, we describe how to deal with such a macro-element considering the absolute displacement of concrete and steel. A detailed description of the computational

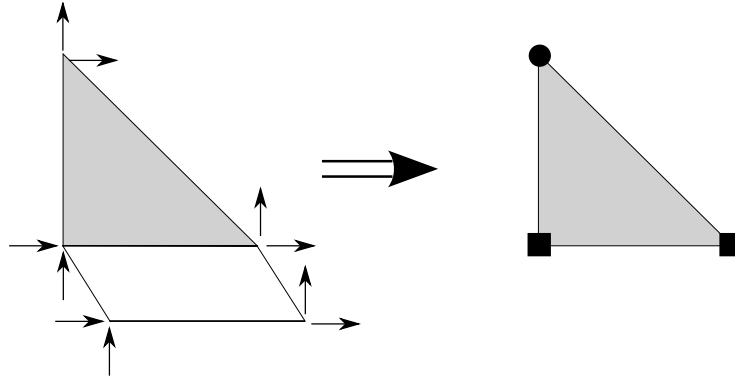


Figure 3.1: Kinematics of the macro element and enriched finite element

strategy for both cases is given in [53]. For simplicity, we assume that the steel rebar coincides with an element edge (see Figure 3.1).

The relative bond-slip displacement being defined as :

$$\boldsymbol{\alpha}(\mathbf{x}) = \sum_{j=1}^2 M_j(\mathbf{x}) \boldsymbol{\alpha}_j \quad (3.15)$$

the displacement field for the macro-element is given, considering XFEM-type interpolation to ensure continuity of the bond-slip, by:

$$\mathbf{d}(\mathbf{x}) = \sum_{i=1}^3 N_i(\mathbf{x}) \left(\mathbf{d}_i^c + \sum_{j=1}^2 M_j(\mathbf{x}) \boldsymbol{\alpha}_j \right) \quad (3.16)$$

where \mathbf{d}^c denotes the nodal displacement for concrete and $\boldsymbol{\alpha}$ the relative bond-slip.

From the interpolations given in equation (3.16), we can compute the stress state in each reinforced concrete components by using the algorithms and models presented in section 2.1.

For the concrete part, we have:

$$\begin{aligned} \mathbf{d}^c(\mathbf{x}) &= \sum_{i=1}^3 N_i(\mathbf{x}) \mathbf{d}_i^c \\ \boldsymbol{\varepsilon}^c(\mathbf{x}) &= \sum_{i=1}^3 \mathbf{B}_i^c(\mathbf{x}) \mathbf{d}_i^c + \mathbf{G}_r(\mathbf{x}) \bar{\mathbf{u}} \quad \text{with } \mathbf{B}_i^c = \begin{bmatrix} \frac{\partial N_i}{\partial x} & 0 \\ 0 & \frac{\partial N_i}{\partial y} \\ \frac{\partial N_i}{\partial y} & \frac{\partial N_i}{\partial x} \end{bmatrix} \end{aligned} \quad (3.17)$$

where N_i are the standard shape functions for Constant Strain Triangle.

For the steel part, we have:

$$\begin{aligned}\mathbf{d}^s(\mathbf{x}) &= \sum_{i=1'}^{2'} M_j(x)(\mathbf{d}_j^c + \boldsymbol{\alpha}_j) \\ \boldsymbol{\varepsilon}^s(\mathbf{x}) &= \sum_{i=1'}^{2'} B_j^s(x)(\mathbf{d}_j^c + \boldsymbol{\alpha}_j)\end{aligned}\quad (3.18)$$

where M_j are the standard shape functions for 2-node bar element. We can note that only the displacement of concrete for nodes 1 and 2 (see Figure ??) contribute to the computation of the steel displacement.

The stiffness matrix and internal loads for the macro-element are computed by assembly of the stiffness and internal loads obtained for each component.

The resolution of the weak form of the equilibrium equations is then performed by an operator-split method. At time t_{n+1} , the system of equations is partitioned into a set of global equations providing the new value of the displacement \mathbf{d}_{n+1}^c and a set of local equations related to the distribution of the bond-slip and providing the new value of the slip $\boldsymbol{\alpha}_{n+1}$: For given \mathbf{d}_n and $\boldsymbol{\alpha}_n$, find \mathbf{d}_{n+1} such that

$$\mathbf{r}^{cs}(\mathbf{d}_{n+1}^c, \boldsymbol{\alpha}_n) = \left[\sum_{e=1}^{Nel} \mathbf{A} \mathbf{f}^{c,int,e}(\mathbf{d}_{n+1}^c) + \sum_{e=1}^{Ns} \mathbf{f}^{s,int,e}(\mathbf{d}_{n+1}^c, \boldsymbol{\alpha}_n) - \mathbf{f}^{ext,e} \right] = \mathbf{0} \quad (3.19)$$

and

$$\mathbf{r}^{bss}(\boldsymbol{\alpha}_{n+1}) = \sum_{e=1}^{Ns} \left[\mathbf{f}^{s,int,e}(\mathbf{d}_{n+1}^c, \boldsymbol{\alpha}_{n+1}) + \mathbf{f}^{bs,int,e}(\boldsymbol{\alpha}_{n+1}) \right] = \mathbf{0} \quad (3.20)$$

where

$$\begin{aligned}\mathbf{f}^{c,int,e} &= \int_{\Omega^e} \mathbf{B}^{cT} \boldsymbol{\sigma}^c(\mathbf{d}^c, \boldsymbol{\alpha}) d\Omega \\ \mathbf{f}^{s,int,e} &= \int_{\Gamma^e} \mathbf{B}^{sT} \boldsymbol{\sigma}^s(\mathbf{d}^c, \boldsymbol{\alpha}) d\Gamma \\ \mathbf{f}^{bs,int,e} &= \int_{\Gamma^e} \mathbf{B}^{bsT} \boldsymbol{\sigma}^{bs}(\boldsymbol{\alpha}) d\Gamma\end{aligned}\quad (3.21)$$

2.3 Numerical examples

We present here the kinds of result of two examples, which could be obtained from the previous model presented in Section 2.1. In these examples, we study the capabilities of the proposed model to provide the predictive results for four-point bending test. The selected specimen for the first example is presented in Figure 3.2 with dimensions $L \times h \times b$ equal to $2250 \times 300 \times 300(mm)$. For this RC specimen, only one steel layer is modeled with $2 \times \phi 16$ located at the position $30mm$ from the bottom line. The material properties used in this example include for concrete: the Young's modulus E_b equal to $38000MPa$, the poisson coefficient ν_b equal to 0.2, the fracture energy G_f equal to $100N/m$ and $\bar{\sigma}_f$ equal to $2.3MPa$. For steel reinforcement, we use the property values: $E_s = 210000MPa$, $\nu_s = 0.3$, $K_b = 19600MPa$, $G_b = 15000MPa$ and $\tau_y = 10MPa$ (see [53]).

We can observe the different mechanism at different stages in the loading process. First macro-cracks appear in the between two sections, where the loading is applied as in Figure 3.3. The crack patterns keep growing along the rebar, while some macro-cracks developing into the neutral line of the beam. In Figure 3.4, we can see the crack pattern at an advanced post critical scenario. The displacement contour following the y-axis is represented in Figure 3.5. We clearly notice that the discontinuities correspond with the curving cracks.

Finally, the global response in Figure 3.6 shows clearly the loss of rigidity due to the damage of concrete in the structure. After the elastic part of loading, the subsequent loading/unloading sessions can be observed when cracks appear and keep growing. As the structure has the heavy reinforcement, we do not observe the large discontinuity in the response and the reinforcement plays the dominant role in the structural capacity.

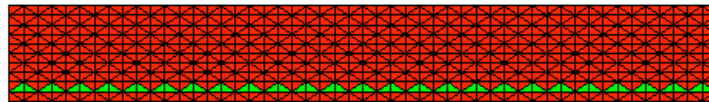


Figure 3.2: Four point bending test on RC specimen: geometry, loading and finite element mesh

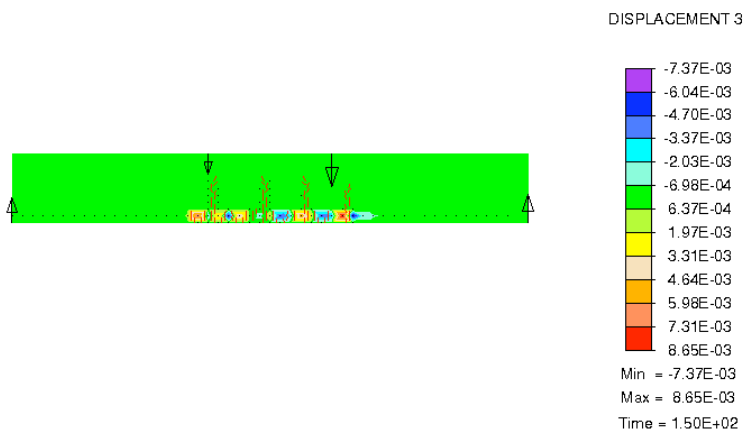


Figure 3.3: Bond-slip along the bar and crack pattern for the first macro-cracks

The second example was computed in order to observe differences in the crack pattern and the global response when the ratio of steel/concrete is changed. In this case, the steel reinforcement ratio is only equal to half the one of the ratio in the previous example, while all of other material properties are still not changed.

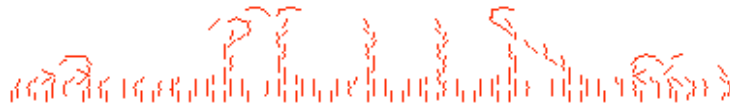


Figure 3.4: Cracks pattern at an advance loading stage

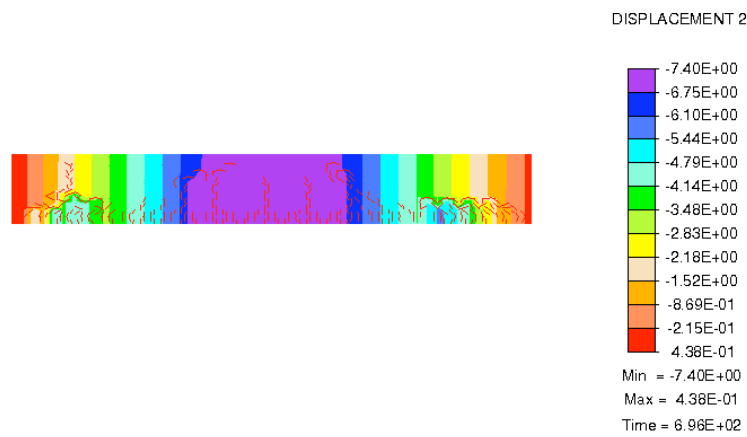


Figure 3.5: Displacement field along axis Y

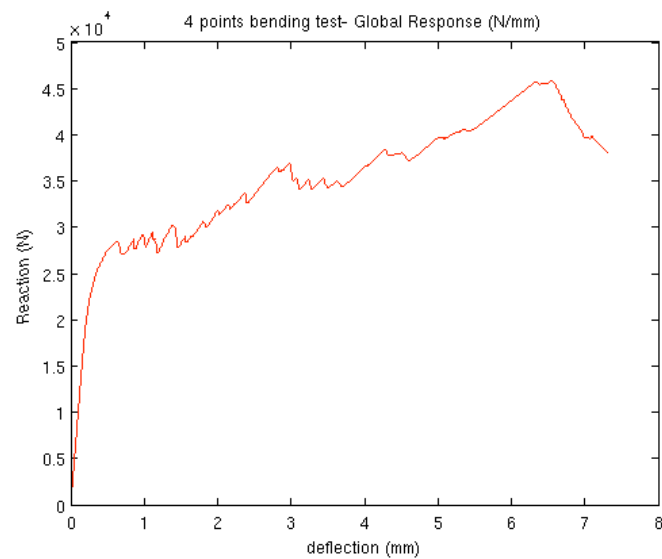


Figure 3.6: Global response for the heavy reinforcement

The crack pattern represented in Figure 3.7 shows us the cracks, which are developed

more regularly than those in the previous case of the higher reinforcement percentage. This phenomenon is due to the weaker role that steel governs in the structural process. We also observe in Figure 3.8 the role governed by the bond slip. On both parts of a crack, positive and negative bond-slip sliding is observed. On the left side, the concrete part moves sharply to the left due to the discontinuity, whereas the steel remains at the same place. As the consequence, positive relative bond-slip sliding is observed. The opposite signs and the same scenario apply to the right side.

In comparison of the global response for the heavy and weak reinforcement, in the weaker one we can observe (see Figure 3.9) the strong discontinuities in the loading and displacement curve due to the fact that concrete is predominant in the structural response. When concrete is totally damage, we will observe an elastic part corresponding to the steel behavior.

Beside the purpose to introduce the bond slip and crack pattern in two examples, we concentrate on the distance between two macro cracks that will be a basis for determining the length of element in stress-resultant macro model for reinforced concrete beam-column. We can discuss more about this problem on the numerical example section.

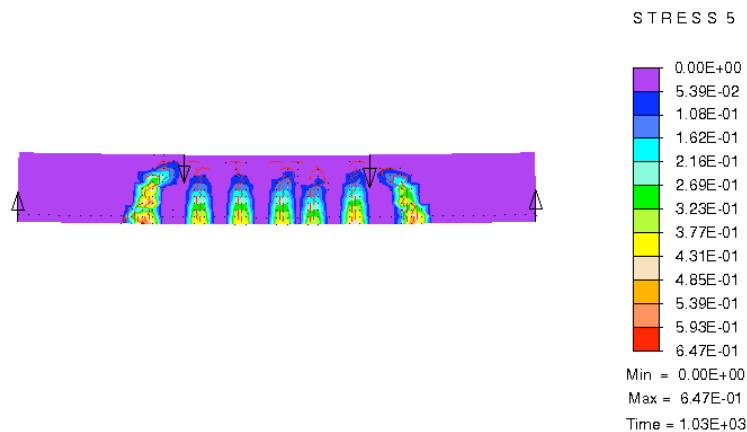


Figure 3.7: Cracks opening in the RC specimen

3 Stress-resultant macro model: embedded displacement discontinuities

We present in this section the main ingredients to design a macro-model for reinforced concrete beam integrating, through embedded discontinuities, all local fracture phenomena responsible for the failure of reinforced concrete namely concrete fracture, bond-slip fracture or eventually, steel rebars fracture. We present briefly the kinematic enrichment

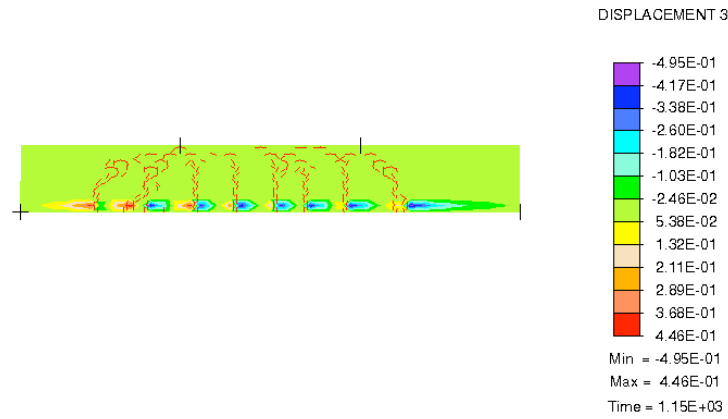


Figure 3.8: Cracks pattern and bond slip sliding

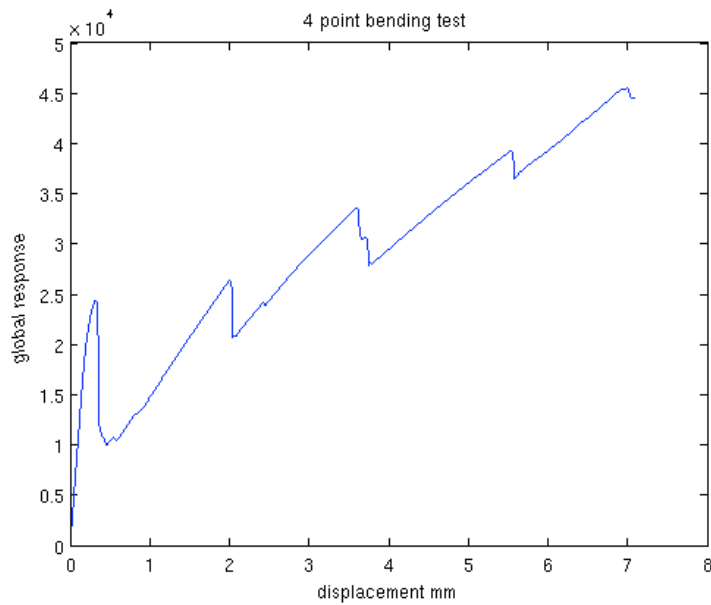


Figure 3.9: Global response for weak reinforcement

and the modification of the weak form of the equilibrium equation and we pay particular attention to give a detailed description of the stress-resultant macro model used to incorporate fracture processes of the different reinforced concrete components.

3.1 Theoretical formulation and finite element representation

We consider here a Timoshenko beam of length L and cross-section A submitted to $f(x)$, $q(x)$, $m(x)$ as well as F , Q , C being respectively the set of distributed loads and of concentrated loads (see Figure 3.10). We denote as (u, v) the components of the displacement of the beam mean-line and θ will denote the rotation of its cross-section.

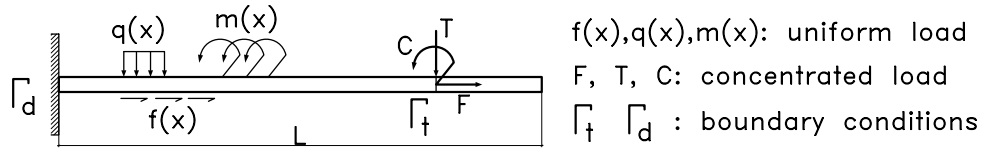


Figure 3.10: General beam diagram for stress-resultant model

The stress-resultant equilibrium equations can be written in a strong form as:

$$\frac{dM(x)}{dx} + T(x) + m(x) = 0; \quad \frac{dN(x)}{dx} + f(x) = 0 \quad \text{and} \quad \frac{dT(x)}{dx} + q(x) = 0 \quad (3.22)$$

Moreover, assuming Timoshenko standard kinematics we have:

$$\varepsilon(x) = \frac{du(x)}{dx}, \quad \gamma(x) = \frac{dv(x)}{dx} - \theta(x) \quad \text{and} \quad \kappa(x) = \frac{d\theta(x)}{dx} \quad (3.23)$$

In order to incorporate in the macro-model the effect of the development of fracture process in the different reinforced concrete components we introduce discontinuities both in the vertical displacement v and the rotation θ for a particular point on the beam mean-line.

In addition to standard degrees of freedom u, v, θ , we consider a discontinuity both in mean-line rotation and vertical displacement located at point x_c . The vertical displacement and rotation field are then written as:

$$v(x) = \bar{v}(x) + \alpha_v H_{x_c} \quad \text{and} \quad \theta(x) = \bar{\theta}(x) + \alpha_\theta H_{x_c} \quad (3.24)$$

where α_v and α_θ denote respectively the vertical displacement and rotation jumps. H_{x_c} is

the Heaviside function being 1 if $x > x_c$, 0 otherwise. By introducing a regular function $\varphi(x)$ being 0 for $x = 0$ and 1 for $x = L$, we can rewrite the previous expressions as:

$$\begin{cases} v(x) = \underbrace{(\bar{v}(x) + \alpha_v \varphi(x))}_{\tilde{v}(x)} + \alpha_v (H_{x_c} - \varphi(x)) \\ \theta(x) = \underbrace{(\bar{\theta}(x) + \alpha_\theta \varphi(x))}_{\tilde{\theta}(x)} + \alpha_\theta (H_{x_c} - \varphi(x)) \end{cases} \quad (3.25)$$

We can note that the regular variables $\tilde{v}(x)$ and $\tilde{\theta}(x)$ have, due to the form of the function $\varphi(x)$, exactly the same essential boundary values then the total transverse and rotational displacements $v(x)$ and $\theta(x)$. Such a choice allows to cancel the contribution of the discontinuities α_v and α_θ on the boundary of the domain leading to local contribution of the discontinuities.

With such interpolations, the beam shear strain and curvature can be decomposed into a regular and a singular part as:

$$\gamma(x) = \bar{\gamma}(x) + \alpha_v \delta_{x_c} \quad \text{and} \quad \kappa(x) = \bar{\kappa}(x) + \alpha_\theta \delta_{x_c} \quad (3.26)$$

where $\bar{\gamma}$ and $\bar{\kappa}$ denotes the regular part respectively of the shear strain and curvature. δ_{x_c} denotes the Dirac delta function on point x_c .

From the expression of the beam strain in equation (3.23), one can build the finite element for such quantities. We consider for that purpose a 2-node beam element of length ℓ^e (see Figure 3.11), where x_c denotes the mid-point of the element.

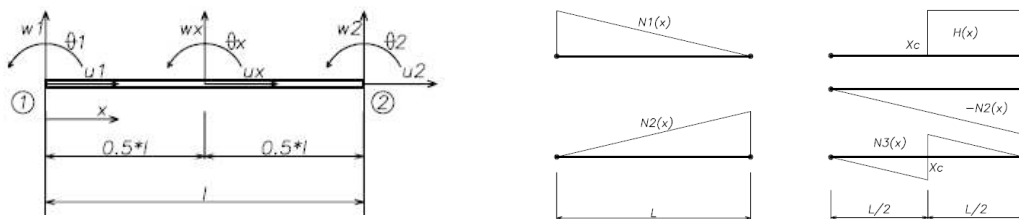


Figure 3.11: Beam element and shapes of interpolation function

A classical interpolation for such an element gives for the axial displacement, transverse displacement and rotation the following discretisation:

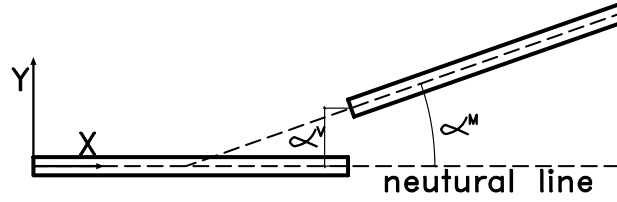


Figure 3.12: Description of transverse displacement and rotation discontinuities in beam element

$$\begin{cases} u(x) = N_1(x)u_1 + N_2(x)u_2 = \mathbf{N}\mathbf{u} \\ v(x) = N_1(x)v_1 + N_2(x)v_2 = \mathbf{N}\mathbf{v} \\ \theta(x) = N_1(x)\theta_1 + N_2(x)\theta_2 = \mathbf{N}\boldsymbol{\theta} \end{cases} \quad (3.27)$$

where $\mathbf{N} = \{N_1(x) = 1 - \frac{x}{\ell^e}, N_2(x) = \frac{x}{\ell^e}\}$ and \mathbf{u} , \mathbf{v} and $\boldsymbol{\theta}$ denote the nodal axial, transverse and rotational displacement vector ($\mathbf{u} = \{u_1, u_2\}^T$).

The rotation and transverse displacement discontinuities are taken into account in the strain interpolation, so that we deal with a kinematic incompatible formulation (see [6]). The strain interpolation are then given by :

$$\begin{cases} \varepsilon(x) = \mathbf{B}^e\mathbf{u} \\ \gamma(x) = \mathbf{B}^e\mathbf{v} - \mathbf{N}\boldsymbol{\theta} + G\alpha_v \\ \kappa(x) = \mathbf{B}^e\boldsymbol{\theta} + G\alpha_\theta \end{cases} \quad (3.28)$$

where $\mathbf{B}^e = \{-\frac{1}{\ell^e}, \frac{1}{\ell^e}\}$. In order to ensure the compatibility of the enhanced strain with the standard ones, the function $\varphi(x)$ introduced in equation (3.25) is chosen equal to $-N_2(x)$ so that, the function G is decomposed into a regular and a singular part as:

$$G = \bar{G} + \delta_{x_c} = -\frac{1}{\ell^e} + \delta_{x_c} \quad (3.29)$$

Denoting as $\boldsymbol{\varepsilon}$ the beam strain, we have :

$$\boldsymbol{\varepsilon} = \begin{bmatrix} \varepsilon \\ \gamma \\ \kappa \end{bmatrix} = \mathbf{B}\mathbf{d} + \mathbf{G}\boldsymbol{\alpha} \quad (3.30)$$

where we have:

$$\mathbf{d} = \begin{bmatrix} u_1 \\ v_1 \\ \theta_1 \\ u_2 \\ v_2 \\ \theta_2 \end{bmatrix}, \quad \boldsymbol{\alpha} = \begin{bmatrix} \alpha_v \\ \alpha_\theta \end{bmatrix}, \quad \mathbf{B} = [\mathbf{B}_1, \mathbf{B}_2] \text{ with } \mathbf{B}_i = \begin{bmatrix} \frac{dN_i}{dx} & 0 & 0 \\ 0 & \frac{dN_i}{dx} & -N_i \\ 0 & 0 & \frac{dN_i}{dx} \end{bmatrix}$$

$$\text{and } \mathbf{G} = \left(-\frac{1}{\ell^e} + \delta_{x_c}\right) \begin{bmatrix} 0 & 0 \\ 1 & 0 \\ 0 & 1 \end{bmatrix}.$$

From those interpolations, the weak form of the equilibrium equations are written considering the incompatible modes method (see [6]) based on the Hu-Washizu three field principle. For that purpose, we consider a kinematically admissible virtual displacement \mathbf{d}^* and the related virtual strain $\boldsymbol{\varepsilon}^* = \mathbf{B}\mathbf{d}^* + \mathbf{G}_v\boldsymbol{\beta}^*$ where \mathbf{G}_v is obtained from \mathbf{G} by imposing the patch-test.

$$\mathbf{G}_v = \mathbf{G} - \int_0^{\ell^e} \mathbf{G} dx = \bar{\mathbf{G}}_v + \begin{bmatrix} 0 \\ 1 \\ 1 \end{bmatrix} \delta_{x_c} \quad (3.31)$$

The weak form of the equilibrium equations results then in a system of two equations:

$$\forall \mathbf{d}^*, \forall \boldsymbol{\beta}^* \left\{ \begin{array}{l} \int_0^L \mathbf{d}^{*T} \mathbf{B} \boldsymbol{\sigma} dx - \int_0^L \mathbf{d}^{*T} \mathbf{N}^T \mathbf{f} dx - \int_{\Gamma_T} \mathbf{d}^{*T} \mathbf{N}^T \mathbf{F} d\Gamma = 0 \\ \int_0^{\ell^e} \boldsymbol{\beta}^{*T} \mathbf{G}_v^T \boldsymbol{\sigma} dx = 0 \quad \forall e \in [1, N_{elem}] \end{array} \right. \quad (3.32)$$

where: $\boldsymbol{\sigma} = \begin{bmatrix} N \\ T \\ M \end{bmatrix}$ is the stress-resultant vector, $\mathbf{f} = \begin{bmatrix} f \\ q \\ m \end{bmatrix}$ is the distributed load vector,

$\mathbf{F} = \begin{bmatrix} F \\ Q \\ C \end{bmatrix}$ is the concentrated load vector and Γ_T collects all the points where concentrated loads are prescribed.

We finally obtain a set of two equations:

$$\begin{cases} \mathbf{A}_{e=1}^{N_{elem}} [\mathbf{f}^{e,int} - \mathbf{f}^{e,ext}] = \mathbf{A}_{e=1}^{N_{elem}} \left[\int_0^{\ell^e} \mathbf{B}^T \boldsymbol{\sigma} dx - \int_0^{\ell^e} \mathbf{N}^T \mathbf{f} dx - \int_{\Gamma_T} \mathbf{N}^T \mathbf{F} d\Gamma \right] = \mathbf{0} \\ \int_0^{\ell^e} \bar{\mathbf{G}}_v^T \boldsymbol{\sigma} dx + \begin{bmatrix} T \\ M \end{bmatrix}_{x=x_c} = \mathbf{0} \quad \forall e \in [1, N_{elem}] \end{cases} \quad (3.33)$$

The second equation is a local equation written on each element enriched by discontinuity. This local equation can be interpreted as the weak form of the traction (being there the transverse load and bending moment) continuity condition across the discontinuity. If we assume that the material outside the discontinuity is non linear with an incremental law of the form:

$$\dot{\boldsymbol{\sigma}} = \mathbf{D}^{in} \dot{\boldsymbol{\varepsilon}} \quad (3.34)$$

and that the dissipation on the discontinuity is also managed by a non-linear law given in an incremental form as:

$$\begin{bmatrix} \dot{T} \\ \dot{M} \end{bmatrix} = \mathbf{D}_{x_c} \dot{\boldsymbol{\alpha}} \quad (3.35)$$

the system (3.33) can be written in an incremental form as:

$$\begin{cases} \mathbf{A}_{e=1}^{N_{elem}} [\mathbf{K}^e \Delta \mathbf{d} + \mathbf{F}_r \Delta \boldsymbol{\alpha} - \mathbf{f}^{e,ext}] = \mathbf{0} \\ \mathbf{F}_v^T \Delta \mathbf{d} + (\mathbf{H} + \mathbf{D}_{x_c}) \Delta \boldsymbol{\alpha} = \mathbf{0} \end{cases} \quad (3.36)$$

where

$$\mathbf{K}^e = \int_0^{\ell^e} \mathbf{B}^T \mathbf{D}^{in} \mathbf{B} dx, \quad \mathbf{F}_{r/v} = \int_0^{\ell^e} \mathbf{B}^T \mathbf{D}^{in} \bar{\mathbf{G}}_{r/v} dx \quad \text{and} \quad \mathbf{H} = \int_0^{\ell^e} \mathbf{G}_v^T \mathbf{D}^{in} \bar{\mathbf{G}}_r dx$$

This set of equations is solved taking advantage of the fact that the second equation is a local one. An operator split method is then used to compute first the value of the local parameter that is $\boldsymbol{\alpha}$ and then by static condensation at the element level, the displacement \mathbf{d} is obtained as the solution of:

$$\mathbf{A}_{e=1}^{N_{elem}} [\hat{\mathbf{K}}^e \Delta \mathbf{d} - \mathbf{f}^{e,ext}] = \mathbf{0} \quad (3.37)$$

with $\hat{\mathbf{K}}^e = \mathbf{K}^e - \mathbf{F}_r (\mathbf{H} + \mathbf{D}_{x_c})^{-1} \mathbf{F}_v^T$.

3.2 Stress-resultant constitutive laws

The numerical strategy used to enrich Timoshenko beam kinematics has been detailed previously. To complete the description of the macro-model, it remains to present the two constitutive models used to describe the behavior outside the discontinuity and on the discontinuity. Those two models are built in the framework of the thermodynamics of continuum media in a stress-resultant manner. We consider here a beam submitted to bending. The axial behavior of the beam is supposed to remain elastic, all the material non-linearities and dissipation are supposed to be related to the transverse and bending behavior. In the following, we detail how to build the shear and bending constitutive models both for the material outside the discontinuity and for the discontinuity.

We present here the type of models used in a generic form. In the following, σ should be either the transverse load T or the bending moment M . For the bulk behavior, we consider a classical elasto-plastic model with:

- the additive decomposition of strain:

$$\boldsymbol{\varepsilon} = \boldsymbol{\varepsilon}^e + \boldsymbol{\varepsilon}^p \quad (3.38)$$

where $\boldsymbol{\varepsilon}$ designates the curvature κ when dealing with bending and the shear strain γ when dealing with transverse load.

- an Helmholtz free energy:

$$\Psi(\boldsymbol{\varepsilon}^e, \xi) = \frac{1}{2} \boldsymbol{\varepsilon}^e C \boldsymbol{\varepsilon}^e + \Xi(\xi) \quad (3.39)$$

where C is the elastic modulus (EI when considering bending and GA when considering shear with E the Young modulus, G the shear modulus, I the cross-section inertia and A the cross-section area) of the material and Ξ is related to hardening.

- a yield function:

$$\phi(\sigma, q) = |\sigma| - (\sigma_y - q) \leq 0 \quad (3.40)$$

where q is the stress-like variable associated to hardening internal variable ξ and σ_y is the limit stress value.

Finally, the plastic dissipation for such a model is given by:

$$0 \leq \mathcal{D}^p = \sigma \dot{\boldsymbol{\varepsilon}} - \frac{d}{dt} \Psi(\boldsymbol{\varepsilon}^e, \xi) \quad (3.41)$$

The state equations are then given by:

$$\sigma = C(\varepsilon - \varepsilon^p) \quad \text{and} \quad q = -K(\xi)\xi \quad (3.42)$$

In the present work, we have chosen linear hardening law, so that the parameters K are constants. By appealing to the principle of maximum plastic dissipation, one can obtain the internal variables evolution equations:

$$\dot{\varepsilon}^p = \dot{\lambda} \frac{\partial \phi}{\partial \sigma} = \dot{\lambda} \text{sign}(\sigma) \quad \text{and} \quad \dot{\xi} = \dot{\lambda} \frac{\partial \phi}{\partial q} = \dot{\lambda} \quad (3.43)$$

and the constitutive equations:

$$\dot{\sigma} = \begin{cases} E\dot{\varepsilon} & \dot{\lambda} = 0 \\ \left[E - \frac{E \frac{\partial \phi}{\partial \sigma} E \frac{\partial \phi}{\partial \sigma}}{\frac{\partial \phi}{\partial \sigma} E \frac{\partial \phi}{\partial \sigma} + \frac{\partial \phi}{\partial q} K \frac{\partial \phi}{\partial q}} \right] \dot{\varepsilon} = \frac{EK}{E+K} \dot{\varepsilon} & \dot{\lambda} > 0 \end{cases} \quad (3.44)$$

with the loading/unloading conditions $\dot{\lambda}\phi = 0$, $\dot{\lambda} \geq 0$, $\phi \leq 0$, λ being the Lagrange multiplier. All of those equations give finally for the plastic dissipation the following expression:

$$0 \leq \mathcal{D}^p = \sigma \dot{\varepsilon}^p + q \dot{\xi} = \sigma_y \dot{\xi} \quad (3.45)$$

In order to consider the different stages of the behavior, if the beam is in the hardening phase, several yield functions are subsequently introduced. For instance, for bending hardening behavior, two different yield functions are considered and consequently two hardening phases characterized by two limit values:

- M_c corresponds to the cracking limit value that is the elastic limit for bending moment.
- M_y corresponds to the yield moment at which steel rebars start yielding.

Figure 3.13 gives the moment/curvature relation and defined the limit values used in this work for the bending behavior of the beam.

As regards the discontinuity behavior, we consider a rigid-plastic model with a yield function of the form:

$$\bar{\phi}(\sigma_\Gamma, \bar{q}) = |\sigma_\Gamma| - (\sigma_u - \bar{q}) \leq 0 \quad (3.46)$$

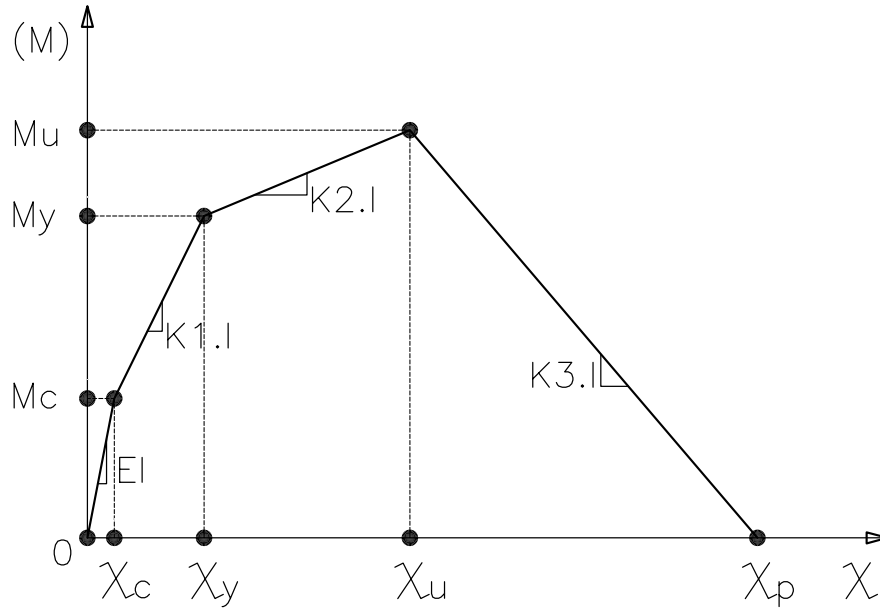


Figure 3.13: Moment-Curvature relation for stress resultant macro model

where σ_Γ denotes the value of either the bending moment or the transverse load at the surface of discontinuity Γ and σ_u is the ultimate generalized stress value. \bar{q} is the stress-like variable associated to softening. We have, when considering linear softening, $\dot{\bar{q}} = -\bar{K}\dot{\xi}$ with $\bar{K} < 0$. Similar construction of the model as the one presented previously can be pushed further (the only difference lies in the fact that we deal here with a rigid-plastic behavior). We obtain then for the constitutive law:

$$\dot{\sigma}_\Gamma = \bar{K}\dot{\alpha} \quad (3.47)$$

where the jump α is either α_v or α_θ depending on whether we consider shear or bending constitutive model.

For such a model, the dissipation related to the softening part of the behavior is given by:

$$\bar{D}^p = \sigma_\Gamma \dot{\alpha} + \bar{q} \dot{\xi} = \sigma_u \dot{\lambda} \quad (3.48)$$

where $\dot{\lambda}$ is the plastic multiplier associated to the discontinuity. We can note that the displacement jump α is no more than a localized plastic deformation accounting for the irreversible phenomena occurring when plastic hinges develop.

Finally, we can compute the total "fracture energy" G_f related to the considered rupture mode as:

$$G_f = \int_{t_0}^{t_f} \int_{A^e} \sigma_{\Gamma} \dot{\alpha} dS dt \quad (3.49)$$

where A^e is the area of the beam cross-section, t_0 is the time corresponding to initiation of the localized mode and t_f corresponds to complete failure of the beam. Considering constitutive laws and evolution equations for the discontinuity, we obtain for the fracture energy the following expression in terms of the limit stress and the softening parameter:

$$G_f = -A^e \frac{\sigma_u^2}{2\bar{K}} \quad (3.50)$$

such a fracture energy can be computed for both fracture modes : bending or shear.

4 Numerical examples

In this section, we present the numerical examples using both the new stress-resultant macro model for reinforced concrete beam-column presented clearly in previous section and multi-fiber model presented in previous parts. The four-point bending test of the beam, where the geometry, dimension of rectangular cross-section, as well as the number of steel reinforcement and the material properties are the same as those presented in the previous section, is considered as in Figure 3.14.

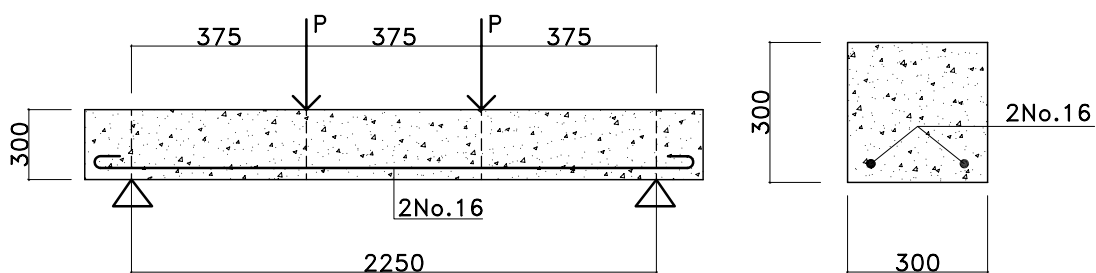


Figure 3.14: Geometry and details of beam in the four-point bending test

We apply both stress-resultant macro and multi-fiber models in this example, with the purpose to find out the differences among the computational results obtained from all of presented models. In the first step, we consider to choose the length of element L_e . This factor, in the local element level, affects not only the equivalence of internal strain energy

and dissipated energy, but also the time in computation. Observing the crack positions and distance between two macro cracks as well as the numbers of crack in the span between two external load positions in Figure 3.7 and Figure 3.8, in the beam divided into 3 spans with the length of each span L_s equal to $2.250/3 = 0.75(m)$, we choose 5 elements for each span. The length of each element L_e is equal to $0.75/5 = 0.15(m)$ as the choice for meshing the beam.

The general computational diagram for both multi-fiber and macro models as well as the post transverse displacement of the beam in this example can be seen in Figure 3.15. For control the transverse displacement of the beam, we impose two displacements at two external load positions in the computation for obtaining the behavior of beam expressed by the relation between support reaction and imposed displacement (see Figure 3.16).

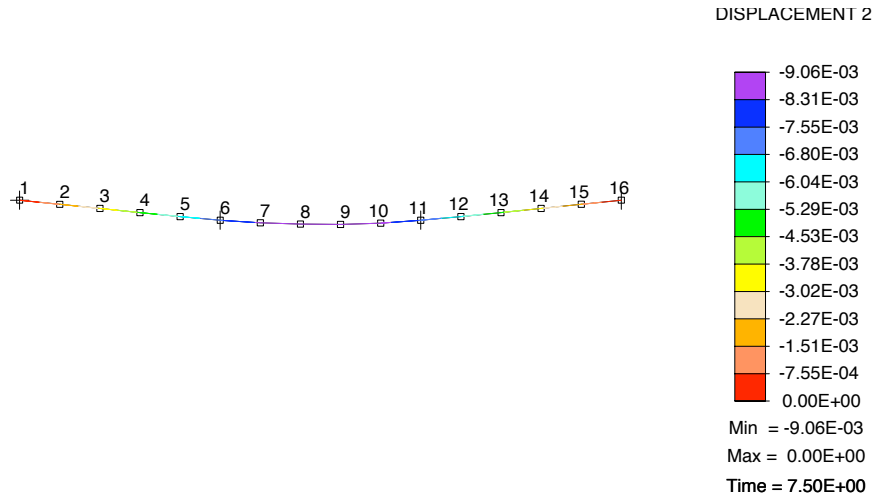


Figure 3.15: Computational diagram and post transverse displacement of tested beam

In the multi-fiber computation, we use the cross-section with the dimension $b \times h = 30 \times 30(cm)$. This cross-section is divided by 20 fibers of concrete and inserted 2 discrete fibers of steel reinforcement describing for $2\phi 16$ inside. The concrete and steel material models applied into each fiber for this case are kinds of strain discontinuity model, which can be seen more details from two previous parts. In this multi-fiber computation, we especially consider the softening modulus of the tension phase in concrete. Three values are used for three particular cases: the first value of $K_{sb} = 40.e9(Pa)$, the second value of $K_{sb} = 50.e9(Pa)$, and the third value of $K_{sb} = 53.3e9(Pa)$. When we change the softening modulus, the behavior of reaction/deflection are expressed by different curves, especially those differences are presented clearly in the plastic hardening phase of global behavior. The smaller value of softening modulus we use, the more smooth curve we obtain. On other words, this multi-fiber model can also express the appearance of macro cracks comparing with the presented global response of X-FEM model in the Figure 3.6 of Section 2.3 and if increasing the fracture energy G_f in concrete, we shall obtain the more smooth

curve of the global behavior.

In the computational example of stress-resultant macro model, we obtain the global response closed to that one computed by the multi-fiber model (see Figure 3.16). Comparing global response of both macro and multi-fiber model with that of X-FEM model, we recognize that the values of prominent moment M_y and M_u close to those of X-FEM model. However, the values of curvature corresponding prominent moments are not much different from those of X-FEM model, we can compare two points of couple (M_y, κ_y) and (M_u, κ_u) of each global response for recognizing what affect to those differences. In this example, the small difference of curvature is derived from the bond-slip effect and diagonal crack of coupled shear force and bending moment (T, M) in two spans at two ends of the beam.

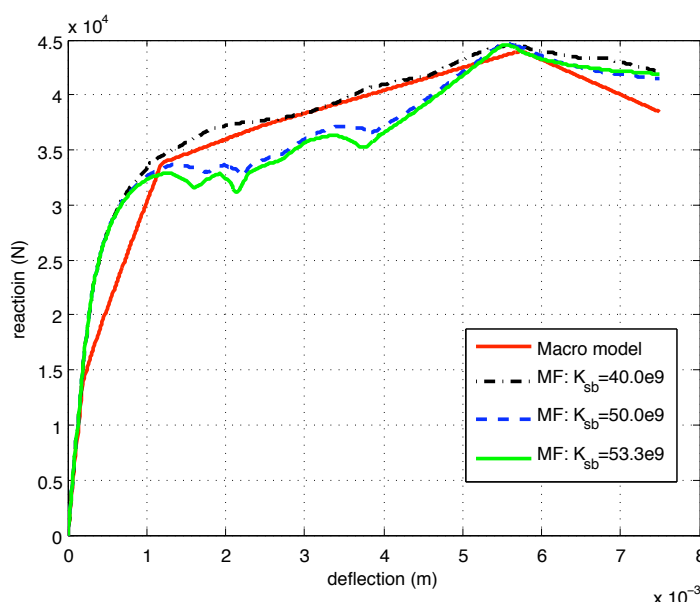


Figure 3.16: Global behavior of support reaction and deflection of tested beam

5 Conclusions

In this work, we also present briefly the problems for the concrete and steel material model as well as the bond-slip problem applied into the 2D plate finite element model, where the strain discontinuities in plate element are embedded.

The new version for stress-resultant macro model for reinforced concrete beam-column is built and presented, in which beside the appearance of combined moment and axial force in the previous version for computing the behavior of frame structure with the ultimate load and until the complete collapse, the problem of shear failure is also considered

with the adding new yield function of shear load. By this model, we can solve the general problem for frame structure at the macro level with saving time in computation.

With presenting a X-FEM model, it is not only the basis for determining the length of element, but also basic results for comparing the result obtained from both multi-fiber and macro model. In the next study, it is necessary to indicate the effects of the reinforcement bond-slip and the shear failure included the stirrup effect. As the same creating relationship between prominent moments and axial force in the second part, for knowing clearly the effect of the shear force and axial load couple, we shall consider to create that relationship with both shear and axial force changes based on the X-FEM model.

One more important problem that we need to consider the ratio of reinforcement in the cross-section. This ratio affects to both crack distance and the crack opening, so that this ratio will be considered as a factor for determining the length of element.

Conclusion

The main goal of this work was pertinent to the performance-based design of the reinforced concrete frame structures. Based upon such an approach, we can seek to optimize a number of factors that are involved in the computed nonlinear response, such as material properties of concrete and steel, the dimensions of the cross-section, the steel reinforcement ratio. This is made possible for any particular loading program by the approach presented herein, which relies on material level information (with the realistic properties of concrete and steel, including the localized failure) in order to build the stress resultant model for a particular reinforced concrete cross-section. In this manner we end up with what is most likely the most reliable basis for parameter identification which possesses the predictive capabilities. Moreover, the idea to build the stress-resultant constitutive model for a RC beam from the corresponding properties of the constituents is the main advantage with respect to classical and more recent works on ultimate limit load failure of frame structure, where the stress-resultant models are proposed in a fairly ad-hoc manner.

The stress-resultant constitutive model we initially developed for beam-bending failure mode, was easy enough to modify in order to account for a beam-column failure in the presence of axial force. The strategy used herein, where the prominent values of moment, such as cracking moment, yielding-moment, and ultimate moment are recomputed for the corresponding (non-zero) value of axial force, and further connected by curve fitting (by using the computer code MATLAB), proved to be sufficiently accurate for the prediction of the ultimate limit load of the reinforced concrete frame structure. Such a strategy, in addition, resulted with a very robust approach, which is quite likely the consequence of the bending-dominated failure despite the presence of the axial force.

The final development with this reinforced concrete stress-resultant model carried out herein concerns the examination of the model capabilities to represent the results obtained by a more refined 2D model (see [53]) of reinforced concrete that can take into account the bond-slip and any crack orientation (not necessarily orthogonal with respect to the steel reinforcement, such as for the case of cracks under the shear force). In fact, the comparison with this refined model allowed us to obtain the proper length of the beam element to be positioned against the crack, as well as the proper amount of fracture energy. We could thus imagine using this stress-resultant beam model as the replacement of the refined model (see [53]) once the cracks have stabilized, (with no further significant development in cracking), which should improve the computational efficiency for subse-

quent computations. The only information that the present stress-resultant beam model can not match coming from the refined model concerns the cracks under the shear force, which do not fit within the framework of beam theory.

A very important part of the developments of the beam model presented herein concerns the proper strain field representation for different phases of the beam failure. In particular, we have used an embedded discontinuity of the rotation (placed in the middle of the Timoshenko beam, at the single Gauss point used for computations of all matrices). This results in the appropriate representation of the localized failure mechanism, where a plastic hinge is created (with the total resistance characterized by the corresponding amount of fracture energy). The rotation discontinuity is handled within the framework of incompatible mode method (see [1]), which results with the Timoshenko beam element that can be introduced within any computer code.

In fact, there are still many other problems affecting to the local and global responses of reinforced concrete frames that we ought to study in future. For example, in the future work we would try embedding not only the relationship of moment, but also axial force as well as shear force into the macro model for beam-column and compute the optimization for reinforced concrete frame by using combination of macro and X-FEM models. We would ideally seek as the final development the adaptive structural model of this kind where the most adequate representation (between the present stress-resultant beam, multi-fiber beam or refined 2D beam model) would be used for the current computational phase in the process of computing the ultimate limit load of a reinforced-concrete frame under a given loading program.

Bibliography

- [1] Adnan IBRAHIMBEGOVIC. *Mécanique non linéaire des solides déformables - Formulation théorique et résolution numérique par éléments finis-2006*
- [2] A. IBRAHIMBEGOVIC, D. BRANCHERIE. *Combined hardening and softening constitutive model of plasticity: precursor to shear slip line failure -Computational Mechanics 31 (2003), p88-100*
- [3] FRANK J. VECCHIO, MOHAMED BASIL EMARA. *Shear Deformations in Reinforced Concrete Frames - ACI Structural Journal, Vol. 89, NO. 1, 1992*
- [4] S. MOULIN, L. DAVENNE, F. GATUINGT. *Réponse statique d'une poutre en béton armé (section rectangulaire) à comportement non linéaire - Code Aster*
- [5] F. ARMERO, D. EHRLICH. *Numerical modeling of softening hinges in thin Euler-Bernoulli Beams-Computers and Structures 84, p.641-656, 2006*
- [6] IBRAHIMBEGOVIC A., WILSON E. *A modified method of incompatible modes-Communications in Numerical Methods in Engineering, Vol. 7, p.187 - 194, 1991*
- [7] A. IBRAHIMBEGOVIC, F. FREY and J.L. SARF *Limit load analysis of plates with particular reference to steel and reinforced concrete plates-The Proceedings of the First European Conference on Numerical Methods in Engineering, Brussels, 1992*
- [8] A. IBRAHIMBEGOVIC, F. FREY *Stress resultants finite element analysis of reinforced concrete plates-Engineer Computation, p.15 - 30, 1993*
- [9] A. IBRAHIMBEGOVIC, F. FREY *An Efficient Implementation of Stress Resultant Plasticity in Analysis of Reissner-Mindlin Plates - Internation Journal For Numerical Methods in Engineering, Vol. 36, 303-320, 1993*
- [10] A. CIPOLLINA, A. LOPEZ-INOJOSA, J. FLOREZ-LOPEZ *A Simplified Damage Mechanics Approach to Nonlinear Analysis of Frames - Computers and Structures, Vol. 54, 1113-1126, 1995*
- [11] MARIA E. MARANTE, LORENA SUAREZ, ADRIANA QUERO, et AL. *Portal of Damage: A Web-Based Finite Element Program for the Analysis of Framed Structure Subjected to Overloads - Advances in Engineering Software, Vol. 36, 346-358, 2005*

- [12] P. NANAKORN *A Two-Dimensional Beam-Column Finite Element with Embedded Rotational Discontinuities - Computers and Structures, Vol. 82, 753-762, 2004*
- [13] MARIA E. MARANTE, RICARDO PICON, JULIO FLOREZ-LOPEZ *Analysis of Localization in Frame Members with Plastic Hinges - International Journal of Solids and Structures, Vol. 41, 3961-3975, 2004*
- [14] JULIO FLOREZ-LOPEZ *Frame Analysis and Continuum Damage Mechanics - European Journal of Mechanics, A/Solids, Vol. 17, N-02, 1998*
- [15] D. EHRLICH, F. ARMERO *Finite Element Methods for the Analysis of Softening Plastic Hinges in Beam and Frames - Computers and Mechanics, Vol. 35, 237-264, 2005*
- [16] MARIA E. MARANTE, JULIO FLOREZ-LOPEZ *Three-Dimensional Analysis of Reinforced Concrete Frames Based on Lumped Damage Mechanics - International Journal of Solids and Structures, Vol. 40, 5109-5123, 2003*
- [17] MARIA E. MARANTE, JULIO FLOREZ-LOPEZ *Model of Damage for RC Elements Subjected to Biaxial Bending - Engineering and Structures, Vol. 24, 1141-1152, 2002*
- [18] EURO CODE 2 *Design of Concrete Structures - Part 1-1 : General Rules and Rules for Buildings*
- [19] A.W. BEEBLY, R.S. NARAYAMAN *Designers' Handbook to Euro code 2, Part 1-1, Design of Concrete Structures*
- [20] JAKA DUJC, BOSTJAN BRANK, A. IBRAHIMBEGOVIC *Multi-scale computational model for failure analysis of metal frame that includes softening and buckling*
- [21] A. IBRAHIMBEGOVIC, P. JEHEL and L. DAVENNE *Coupled damage-plasticity constitutive model and direct stress interpolation - Computers and Mechanics, Vol. 42, 01-11, 2008*
- [22] O. C. ZIENKIEWICZ and R. L. TAYLOR *Review of The Finite Element Method for Solid and Structural Mechanics - 6th Edition- J. Engrg. Mech, Vol 132, pp. 1400-1400 (2006)*
- [23] NGUYEN Q.S., ZARKA J., *Quelques méthodes de résolution numérique en elastoplasticité classique et en elasto-viscoplasticité, Sciences et Technique de l'Armement, Vol. 47, 407-436, 1973*
- [24] NGUYEN Q.S., *On elastic plastic initial - boundary value problem and its numerical implementation, International Journal for Numerical Methods in Engineering, Vol. 11, p. 817-832, 1977*

- [25] NGUYEN Q.S., *Stabilité en mécanique non linéaire - Lavoisier, Paris, 2000*
- [26] E.I. Shifrin, B. Brank and G. Surace *Analytical-Numerical Solution of Elliptical Interface Crack Problem - International Journal of Fracture, Volume 94, Number 3 / December, 1998*
- [27] P. LEGER, R. TREMBLAY, *Earthquake ground motions for seismic damage assessment and re-evolution of existing buildings and critical facilities, Damage assessment and reconstruction after natural disaster and previous military activities, 116-144, 2008*
- [28] P. JEHEL, A. IBRAHIMBEGOVIC, P. LEGER, L. DAVENNE *Three scale nonlinear analysis until collapse for a priori damage assessment of RC frame elements in seismic loading, Damage assessment and reconstruction after natural disaster and previous military activities, 345-352, 2008*
- [29] Brancherie D., A. Ibrahimbegovic, *Novel anisotropic continuum-discrete damage model capable of representing localized failure of massive structures. Part I: theoretical formulation and numerical implementation, Journal of Engineering Computations, 26, 100-127, 2009*
- [30] Chen W.F., *Plasticity in Reinforced concrete , McGraw-Hill, New York, 1982*
- [31] Colliat J.B., A. Ibrahimbegovic, L. Davenne, *Saint-Venant plasticity model in strain space and in stress resultants, Journal of Engineering Computations, 22, 536-557, 2005*
- [32] Cox J.V., L.R. Herrmann, *Development of a plasticity bond model for steel reinforcement, Mech. Cohesive Frict. Mater., 3, 155-180, 1998*
- [33] Daoud A., *Experimental study of concrete-steel interface, PhD thesis INSA Toulouse (in French), 1995*
- [34] Dominguez N., Brancherie D., Davenne L., Ibrahimbegovic A. *Prediction of crack pattern distribution in reinforced concrete by coupling a strong discontinuity model of concrete cracking and a bond-slip of reinforcement model, Engineering Computations, 22, 558-581, 2005*
- [35] Guo J., Cox, J.V., *Implementation of a plasticity bond model for reinforced concrete, Computers and Structures, 77 (1), p.65-82, 2000*
- [36] Hughes T.J.R. *The Finite Element Method. Prentice-Hall, 1987.*
- [37] Hofstetter G., H.A. Mang, *Computational mechanics of reinforced concrete structures, Vieweg, Braunschweig, 1995*
- [38] A. Ibrahimbegovic, E.L.Wilson, *A unified computational model for static and dynamic frictional contact analysis, Int. J. Numer. Methods Eng., 34, 233-247, 1991*

- [39] A. Ibrahimbegovic, S. Melnyk, *Embedded discontinuity finite element method for modeling localized failure in heterogeneous materials with structural mesh: an alternative to extended finite element method*, *Computational Mechanics*, 41, pp 144-151, 2007
- [40] M. Jirasek, T. Zimmerman, *Embedded crack model: II. Combination with smeared cracks*, *International Journal for Numerical Methods in Engineering*, 50, 1291-1305, 2001
- [41] M. Jirasek, T. Belytschko, *Computational resolution of strong discontinuities*, *Proceedings WCCM-V, Vienna, Austria*, 1-7, 2002
- [42] Kucerova A., Brancherie D., A. Ibrahimbegovic, J. Zeman, Z. Bittnar, *Novel anisotropic continuum-discrete damage model capable of representing localized failure of massive structures. Part II: identification from tests under heterogeneous stress field*, *Engineering Computations*, 26, 128-144, 2009
- [43] Maker B.N., T. Laursen, *A finite element formulation for rod/continuum interaction: The one-dimensional slide-line*, *Int. J. Numer. Method Eng.*, 37, 1-18, 1994
- [44] Mazars J., *A Description of Micro and Macro- Scale Damage of Concrete Structures*, *Engineering Fracture Mechanics*, 25 (5/6): 729-737, 1995
- [45] J.M. Melenk, I. Babuska, *The partition of unity finite element method: Basic theory and applications*, *Int. Jour. Numer. Methods Eng.*, 727-758, 1997
- [46] J. Oliver. *On the discrete constitutive models induced by strong discontinuity kinematics and continuum constitutive equations*. *International Journal of Solids and Structures*, 37:7207-7229.
- [47] Oliver J. et al, *A comparative study on finite elements for capturing strong discontinuities: E-FEM vs X-FEM* *Computer Methods in Applied Mechanics and Engineering*, 2006
- [48] Prathap G. and Naganarayana B.P. *Consistent thermal stress evaluation in finite elements*, *Comput. Struct.*, 54:415-216, 1995.
- [49] Ragueneau F., Dominguez N., A. Ibrahimbegovic *Thermodynamic-based interface model for cohesive brittle materials: Application to bond slip in RC structures*, *Computer Methods in Applied Mechanics and Engineering*, 195 (52), 7249-7263, 2006
- [50] Sluys L.J., R. de Borst, *Failure in plain and reinforced concrete - an analysis of crack width and crack spacing*, *Int. J. Solids Struct.*, 33, 3257-3276, 1996
- [51] E. Stein, D. Tihomirov, *Anisotropic damage-plasticity modeling of reinforced concrete*, *Proceedings ECCMÖ99, Munchen, Germany*, 1-19, 1999

- [52] Yanenko N.N. *The method of fractional steps*. Springer-Verlag, 1971.
- [53] A. BOULKERTOUS *Interaction Feu/Ouvrages en beton arme dans le cas d'un incendie confine: prediction de la fissuration. Application a la problematique des installations nucleaires. These de l'Ecole Normale Superieure de Cachan- 2009*
- [54] D. BRANCHERIE *Modeles continus et "discrets" pour les problemes de localisation et de rupture fragile et/ou ductile. These de l'Ecole Normale Superieure de Cachan- 2003*
- [55] Bazant Z.P. *Mechanics of distributed cracking*, *Appl. Mech. Reviews*, ASME, 39, 675-705, 1986
- [56] Bazant Z.P., S. Sener, *Size effect in pull-out tests*, *ACI Mater. J.*, 85, 347-351, 1988
- [57] Bazant Z.P., T. Belytschko, and T.P. Chang. *Continuum theory for strain softening - ASCE Journal of Engineering Mechanics*, 110,12, 1666-1691,1984
- [58] Belytschko T., N. Moes, S. Usui, and C. Parimi, *Arbitrary discontinuities in finite elements - International Journal for Numerical Methods in Engineering*, 50 (4), 993-1013, 2001
- [59] Belytschko T., C. Parimi, N. Moes, N. Sukumar, S. Usui, *Structured extended finite element methods for solids defined by implicit surfaces*, *International Journal for Numerical Methods in Engineering*, 56 (4), 609-635, 2002
- [60] Black T, Belytschko T., *Elastic crack growth in finite elements with minimal remeshing*, *International Journal for Numerical Methods in Engineering*, 45: 601-620, 1999